CARL VON OSSIETZKY
UNIVERSITY OF OLDENBURG

MASTER'S PROGRAMME: MARINE ENVIRONMENTAL SCIENCES

MASTER'S THESIS

Scale Dependence of Subsurface Density Gradients

Author:
Buu Lik DUONG[1,2]
(6450147)

Supervisor/1st referee:
Dr. Wilken-Jon VON APPEN[1]
2nd referee:
Dr. Thomas BADEWIEN[2]

[1]Alfred Wegener Institute, Helmholtz Centre for Polar and Marine Research, Department of Physical Oceanography, Bremerhaven, Germany, [2]Institute for Chemistry and Biology of the Marine Environment, Department of Marine Sensor Systems, University of Oldenburg, Oldenburg, Germany

Location, Date of submission:
Oldenburg, August 30, 2024

Summer Semester 2024

Abstract

Horizontal sampling of the ocean has been sparse for decades because of technical limitations. This can contribute to an incomplete depiction and misleading understanding of the hydrography. This is a particular concern for complex submesoscale and smaller scale flow structures that influence stratification and vertical transport of properties.

We used high resolution observations from a Triaxus towed undulating vehicle and developed a statistical subsampling routine in order to present the first multi-scale investigation of subsurface horizontal density variability in a global context. Hydrographic transects were performed between 2018 and 2022 in the oceanographically distinct regimes of the Arctic marginal ice zone, of a coastal upwelling area, of the equatorial Atlantic, and of the Antarctic Circumpolar Current. The main objectives of this thesis are to determine the scaling properties of density fronts and to identify oceanic regimes that are susceptible to an underestimation of their thermohaline variability.

We find that the amplitude of horizontal density gradients increases nonlinearly as the horizontal resolution is increased. This relation is applicable throughout all study regions allowing for a potential prediction of the gradient distribution for scales not resolved by measurements. Submesoscale density gradients are of higher amplitude along the base of shallow mixed layers, and in the presence of frontal systems, eddies, and subsurface currents. Furthermore, the gradient fields are primarily driven by salinity variability at high northern latitudes and by temperature variability in regions closer to the equator; in the Southern Ocean temperature and salinity largely compensate. The decay rate of the estimated gradients with increasing horizontal distance is related to fractal properties and a scale-dependent compensation of the density field.

This highlights that there is a certain arbitrariness regarding the strengths of density gradients in the present literature. We recommend that the employed horizontal resolution always be quoted alongside values of the horizontal density gradient. The developed statistical method provides a novel approach for handling high-resolution data; its full potential has yet to be explored.

Zusammenfassung

Die horizontale Beprobung des Ozeans erfolgt seit Jahrzehnten aufgrund technischer Limitierungen in geringer Auslösung. Dies kann dabei eine unvollständigen Darstellung und Fehlinterpretation der Hydrographie herbeiführen. Dies gilt insbesondere für komplexe submesoskalige und kleinräumigere Strömungsstrukturen, die die Schichtung und den vertikalen Transport von Eigenschaften beeinflussen.

Wir haben hochauflösende Messungen eines profilierenden Schleppkörpers, dem Triaxus, verwendet und eine statistische Abtast-Routine entwickelt, um die erste multi-skalige Untersuchung der horizontalen Dichtevariabilität unter der Wasseroberfläche in einem globalen Kontext zu präsentieren. Hydrographische Transekte wurden zwischen 2018 und 2022 in den ozeanographisch verschiedenen Regimen der arktischen Eisrandzone, eines küstennahen Auftriebsgebiets, des äquatorialen Atlantiks und des antarktischen Zirkumpolarstroms aufgenommen. Die Hauptziele dieser Thesis bestehen darin, die Skalierungseigenschaften von Dichtefronten zu ermitteln und ozeanische Regime zu identifizieren, die anfällig für eine Unterschätzung ihrer thermohalinen Variabilität sind.

Wir stellen fest, dass die Stärke der horizontalen Dichtegradienten nichtlinear zunimmt, wenn die horizontale Auflösung erhöht wird. Diese Relation gilt für alle Untersuchungsgebiete und ermöglicht eine potenzielle Vorhersage der Gradientenverteilung für Skalen, die nicht durch Messungen aufgelöst werden. Submesoskalige Dichtegradienten haben eine höhere Amplitude entlang der Basis von flachen Deckschichten und in Gegenwart von Frontensystemen, Wirbeln und Strömungen unter der Oberfläche. Darüber hinaus werden die Gradientenfelder in erster Linie durch Salzgehalt Variabilitäten in hohen nördlichen Breiten und durch Temperaturschwankungen in äquatornahen Regionen bestimmt; im Südlichen Ozean gleichen sich Temperatur und Salzgehalt weitgehend aus. Die Abklingrate der Gradienten mit zunehmender lateraler Distanz hängt mit fraktalen Eigenschaften und einer skalenabhängigen Kompensation des Dichtefeldes zusammen.

Diese Abschlussarbeit macht deutlich, dass in der vorliegenden Literatur eine gewisse Willkür hinsichtlich der Stärke der Dichtegradienten besteht. Wir empfehlen, dass die verwendete horizontale Auflösung immer zusammen mit den Werten des horizontalen Dichtegradienten angegeben wird. Die entwickelte statistische Methode stellt einen neuartigen Ansatz für den Umgang mit hochaufgelösten Daten dar, dessen Potenzial noch nicht voll ausgeschöpft ist.

Nomenclature

Acronyms

AAIW	Antarctic Intermediate Water
AASW	Antarctic Surface Water
AAW	Arctic Atlantic Water
ACC	Antarctic Circumpolar Current
ACME	Anticyclonic mode water eddy
AWI	Alfred-Wegener-Institute, Helmholtz Centre for Polar and Marine Research
AW	Atlantic Water
CTD	Conductivity-Temperature-Depth probe
CVFZ	Cape Verde Frontal Zone
EGC	East Greenland Current
EGPF	East Greenland Polar Front
EUC	Equatorial Under Current
IGW	Internal gravity wave
KE	Kinetic Energy
MIZ	Marginal Ice Zone
MLD	Mixed layer depth
ML	Mixed Layer
MSM93	Expedition of the research vessel MARIA S. MERIAN within Fram Strait in 2020
NACW	North Atlantic Central Water
NADW	North Atlantic Deep Water

PF	Polar Front
PS113	Expedition of the research vessel POLARSTERN within the tropical Atlantic in 2018
PS131	Expedition of the research vessel POLARSTERN in northern Fram Strait in 2022
PS133.1	Expedition of the research vessel POLARSTERN within the Sothern Ocean in 2022
PW	Polar Water
SACCF	Southern ACC Front
SACW	South Atlantic Central Water
SB	Southern Boundary
SLA	Sea level anomaly
SST	Sea surface temperature
topAWI	Towed ocean profiler of the AWI
WSC	West Spitsbergen Current

Contents

List of Figures

Chapter 1

Introduction

1.1 Horizontal density variability

Lateral gradients in the density field of the ocean, are a principal part of generating and maintaining its complex and dynamic nature by driving currents and circulation, impacting stratification, and generating vertical fluxes. They can occur on a range of scales spanning from thousands of kilometers to millimeters linked by a downward cascade through horizontal stirring (K. S. Smith & Ferrari, 2009).

1.1.1 The mesoscale

The vertical integration of horizontal density gradients translates into horizontal pressure gradients through hydrostatic balance. On large scales, these pressure gradients can drive ocean currents and mesoscale motions. The mesoscale concerns ocean signals with spatial scales between ten and several hundred kilometers and a typical time scale over which motions evolve of between weeks and months, and represent the major oceanic reservoir of kinetic energy (Chelton et al., 2011; Ferrari & Wunsch, 2009). Mesoscale currents, such as eddies and vortices, are approximately in geostrophic balance and their deep-reaching dynamics and contribution to the lateral transport of salt, heat, and tracers have been a focus of research as early as the 1960s when it became possible to acquire continuous data of currents in the ocean interior (Swallow, 1971). Mesoscale eddies commonly emerge from barotropic instabilities in horizontally sheared motion trapping and advecting distinct water masses to different locations. Thus, eddy edges are characterized by strong horizontal gradients in a variety of properties that can penetrate the interior. Moreover, the circular flow can induce vertical motion as a result of convergence/divergence within the core of cyclonic/anticyclonic cells, a mechanism termed "eddy-pumping". This process results in the downward/upward doming of layers with the same density facilitating the vertical exchange of nutrients and other properties (Boyd & D'Asaro, 1994).

1.1.2 The submeso- and finescale

The submesoscale, characterized by $\mathcal{O}(1)$ Rossby number dynamics (0.1 km-10 km), that is a balance between the Coriolis and the inertial force, has been putting oceanographers on enquiry over the past decades. It corresponds to the energetic bridge between the quasi-geostrophic mesoscale and smaller dissipative scales of which the latter is necessary for achieving a steady state (Eden et al., 2014; McWilliams, 2016). Sharp horizontal gradients in density or other water properties are exhibited by oceanic fronts, typical structural events of the submeso- and smaller spatial scales representing water-mass boundaries mostly within the upper ocean. Such frontal structures can promote instabilities - in the presence of inclinded isopycnals (lateral density gradients) they create a baroclinic pressure field that is not in geostrophic balance providing the source of potential energy for baroclinic instabilities. Density fronts can become unstable to these baroclinic instabilities and slump as a way to dynamically adjust (Ferrari & Young, 1997). This gravitational overturning contributes to rapid restratification of the surface layer and and forms eddies, filaments and meanders converting the available potential energy to kinetic energy (Boccaletti et al., 2007). These submesoscale flows are inherently out of geostrophic balance and undergo a geostrophic adjustment to satisfy the thermal wind balance involving the development of an ageostrophic secondary circulation (ASC; Hoskins and Bretherton, (1972)).

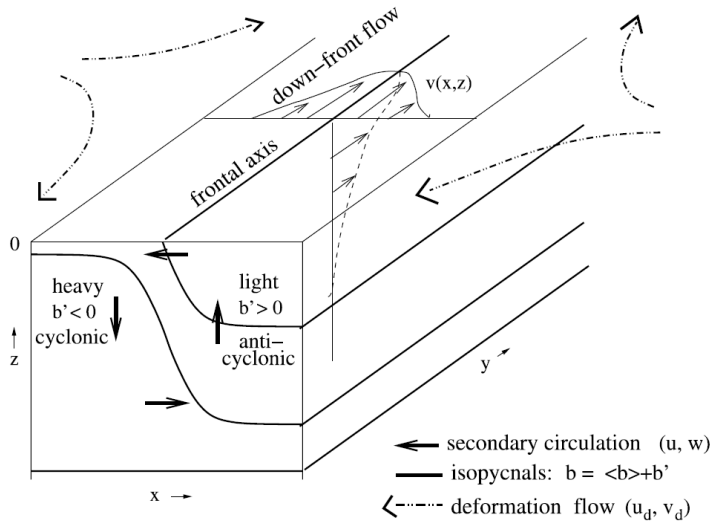

Figure 1. Sketch of surface frontogenesis. Figure from McWilliams et al. (2009).

In the event of a front with uniform lateral density gradients, these ASCs manifest as a circulation cell (see Fig. 1) around the frontal axis consisting of a down- and upwellig limb on the dense and light side, respectively, and across-front motion from the light side at the surface and from the dense side through subduction (McWilliams et al., 2009). The vertical flows exhibit velocities with $\mathcal{O}(10 -$

$100\,\mathrm{m\,day^{-1}}$) as revealed by recent observations (Hosegood et al., 2017; L. Johnson et al., 2020; von Appen et al., 2018) and numerical models (e.g. Manucharyan & Thompson, 2017). Owing to the large vertical velocities, submesoscale frontal structures in the density field have been increasingly considered to contribute to the vertical flux of heat and salt (Thomas et al., 2008), and gases and nutrients (Mahadevan, 2016) between the ocean surface and interior.

Imbalanced motions also manifest in internal gravity waves (IGW), oscillating disturbances spanning the entire stratified water column, yet most commonly found along density boundary layers. They are mostly generated by wind stirring the surface or by barotropic flow over a rough seafloor topography. As IGW propagate away from the location of generation they can interact with other flow structures aliasing vertical density gradients to horizontal structures for scales smaller than 10 km below the surface (Timmermans et al., 2012). Especially topographically generated IGWs are susceptible to nonlinear effects (Sarkar & Scotti, 2017) promoting the downward cascading toward smaller-scale secondary instabilities and turbulence via increased fluid velocities, small-scale waves, and detached flows. When internal gravity waves encounter steep gradients or other disturbances (shear or convective instability), they can break. This breaking process converts wave energy into turbulent kinetic energy, facilitating diapycnal mixing. The resulting turbulence creates microstructures that promote the vertical transport of properties such as heat, salt, and nutrients (e.g. MacKinnon et al., 2017). The turbulent flow itself is characterized by chaotic motion and exhibits statistically self-similar geometric features (fractal geometry; Mandelbrot & Mandelbrot, 1982), that can be found in the small-scale variability of the density field (Wijesekera, 1996).

Despite the growing consideration of submeso- and finescale structures as a major driver in setting surface-layer properties, due to their rapid development within timescales of a few days to hours (Brenner et al., 2020; McWilliams, 2016) the documentation surrounding them is sparse. Traditional oceanographic methodologies for data acquisition, such as CTD sections, lack the horizontal resolution to adequately cover structures and dynamics within these scales (e.g. Duong, 2021). These shortcomings have contributed to today's knowledge resting upon numerical models and theoretical estimates. Yet, global observational efforts have been evolving to assess the rapidly evolving dynamics of submeso- and finescale processes involving the development and operation of novel sampling methodologies.

In recent years, these technological advancements have yielded valuable datasets, revealing that lateral density gradients can be sharpened down to scales of a few meters and that smaller-scale features exist within mesoscale features. In the Bay of Bengal, characterized by large river discharges and monsoonal rainfall,

Jinadasa et al. (2016) observed a narrow front with a steep salinity gradient occurring over just a few meters. This sharp salinity transition was embedded within a broader frontal system where the lateral density gradient was considerably less pronounced. Spiro Jaeger and Mahadevan (2018) observed fronts spanning a wide range of length scales in the Bay of Bengal and that the submesoscale gradients get alleviated due to surface cooling. In a more recent study, Hofmann et al. (2024) observed a submesoscale system near the ice edge in Fram Strait consisting of a near-surface front and a subsurface front at 30-85 m depth introducing the concept of a "step-wise subduction". Subduction of a water mass originates at the surface, which then progresses through fronts at various depths. At each of these fronts properties of the lighter water are passed to the heavier subducting one resulting in weaker lateral density gradients with increasing depth. They suggested that this frontal system was part of a mesoscale eddy-like pattern in temperature and sea ice distribution. Further work involving a surface sailbuoy survey in the Antarctic marginal ice zone during ice retreat time evaluated the spread and frequency of lateral density gradients over a wide range of sampling length scales (Swart et al., 2020). They revealed a sharp rise in gradients as the spatial scales fall below the internal Rossby radius R_i, the scale at which submesoscale structures develop in the upper layer (Boccaletti et al., 2007), reaching up to 0.06 kg m^{-3} km^{-1} for the smallest observed scale of 0.5 km (see Fig. 2). In shallow mixed layer environments, for example in the presence of freshwater layers, data need to be acquired with a high sampling frequency to capture the variability of the surface density field on an adequate level.

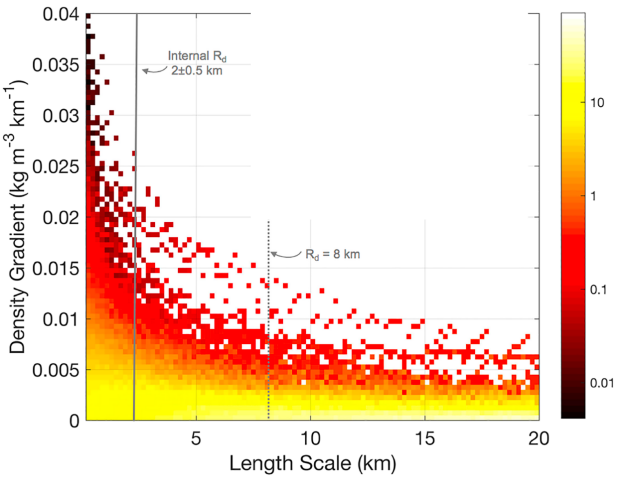

Figure 2. Distribution of lateral density gradients [kg m^{-3} km^{-1}] at various horizontal length scales [km] from a Sailbuoy dataset. The relative occurrence [%] of gradients at each scale bin is displayed by the logarithmic color scale. The gray solid and dashed lines indicate the full-depth and internal Rossby radius of deformation around 60°S/0°E. **(b)** Wavenumber spectra of lateral surface density variance. Figure from Swart et al. (2020) and modified.

Following a similar multi-scale analysis Coadou-Chaventon et al. (pers. comm. 2024) investigated regional contrasts in meso- and submesoscale (15-0.1 km) thermohaline surface variability in the northwest tropical Atlantic in wintertime, influenced by the advection of an Amazon-driven freshwater tongue. Different magnitudes of salinity-driven gradients, many times larger than found in the Antarctic, and a gradient drop-off at smaller length scales differentiated the region in vicinity of the freshwater plume from the open sea and surrounding regions. They proposed that freshwater fluxes are a primary factor driving frontogenesis. The negative correlation between density gradients and lateral spatial scale were also indicated in a global model simulation, in which a sharpening of density gradients occurred for configurations of increasing horizontal resolution (Kjellsson & Zanna, 2017).

1.2 Temperature and salinity contribution

1.2.1 Density compensation

Spatial gradients in density are determined by thermohaline variations. For the vast majority of the world's ocean, the density field is directed by temperature (G. C. Johnson et al., 2012). In regions with a strong salinity variability due to intense river discharge, sea ice melt, or rain fall temperature can, however, play a rather secondary role in governing the density distribution. Temperature and salinity gradients can also cancel out in their effect on density variations such that the density contrast across thermohaline gradients becomes small. A thermohaline front with cold and fresh water on one side and warm and saline water on the other exhibits a weak across-front density signature - a phenomenon termed "compensation". Such compensated fronts are usually stable, hence long-lived features, and globally prominent at scales of 10 km (Drushka et al., 2019). The surface mixed layer (SML) is particularly prone to hosting compensated density fronts. In the subtropical gyre of the North Pacific Rudnick and Ferrari (1999) proposed, based upon highly resolved data sampled with a SeaSoar, that density gradients in the SML were restricted to a spatial scale of 10 km corresponding to the internal Rossby radius. They found thermohaline fronts down to 20 m, albeit with no dynamical signatures. For scales $\leq R_i$, horizontal density gradients are thought to gravitationally collapse, while for larger scales they persist in geostrophic balance. In direct contrast, collecting data in the same region with a towed undulating CTD system, Hosegood et al. (2006) found significant lateral variability in the ML density field extending even down to scales of 2 km. They remarked that this threshold is not universal and potentially varies strongly with location. Based upon a survey of data acquired in the Atlantic, Pacific, and Indian Ocean over a period of 15

years, Rudnick and Martin (2002) revealed that compensation is not typical in shallow MLs and that the tendency for it increases with the mixed layer depth (MLD) and when vertical mixing is strong. When fronts are, however, present in the SML, wind forcing can compensate or even enhance them, depending on their orientation (Du Plessis et al., 2019). They distinguished down-front and up-front winds that drive cross-frontal Ekman transport from the denser to the light side of the front and vice versa. In case of the former, the cross-frontal advection can promote convective instabilities, and thereby enhance mixing by turbulence. In contrast, when lighter water is transported to the denser side, the vertical stratification increases.

1.2.2 Alpha and beta oceans

Carmack (2007) introduced a distinction between alpha and beta oceans defined as regions with temperature and salinity controlled vertical stratification, respectively, responding in different ways to external forcing and mixing processes. In a simplified categorization, alpha oceans predominately occupy low latitudes while high-latitude oceans are considered as beta oceans. The distributions of alpha and beta oceans, however, have more complicated horizontal and vertical structures (Stewart & Haine, 2016). They showed that the upper 50 m of the world's ocean are largely occupied (>95%) by so-called transition zones, in which heat and salt contributions to the vertical stratification are density compensating. At a depth of 100 m the proportion of alpha oceans is comparable to that of transition zone oceans and the simplified latitudinal distribution becomes indeed more evident. At this depth, the major oceanic gyres and the Antarctic Circumpolar Current (ACC) remain transition zone oceans. At 400 m depth, temperature become the governing property for 80% of the global ocean, beta oceans no longer exist in the Atlantic, and the Arctic Ocean is occupied by transition zone oceans for a large part. For even greater depths, they found a beta ocean equatorward intrusion in the Atlantic at 1000 m and in the Indian and Pacific at 1500 m.

1.3 Study sites

1.3.1 The Maginal Ice Zone

The Arctic Ocean is generally considered a beta ocean as its upper layer is permanently stratified by salinity due the presence of sea ice and the freshwater input that is associated with it. Sea-ice is, however, not ubiquitous in the Arctic and more southern parts are actually ice free. The transition between pack ice and the open sea is commonly referred to as the marginal ice zone (MIZ) characterized by a low to intermediate sea ice concentration interspersed with areas of open water.

In summer, a highly stratified surface layer can frequently be present due to sea ice melt (e.g. Hofmann et al., 2024; von Appen et al., 2021). Flow structures, in diverse spatial scales, such as fronts, filaments, and eddies are ubiquitous in the vicinity of the MIZ making it a well-suited laboratory to assess salinity-driven density variabilities over a variety of lateral scales. This transitioning zone is a prominent feature in Fram Strait, the deepest and broadest oceanic gateway that connects the Arctic Ocean with the lower-latitude oceans, separating Greenland and Svalvard (see Fig. 3). The circulation in Fram Strait is mainly driven by two boundary currents: On the eastern side, warm and saline Atlantic Water (AW), originated in the North Alantic, get advected via the West Spitsbergen Current (WSC) along the eastern continental slope of Svalvard. The WSC is mostly barotropic (Teigen et al., 2010), and hence guided by the complex bathymetry characteristic for Fram Strait leading to a bifurcation. The WSC splits into multiple branches, inter alia, eddy-driven recirculation branches (Hattermann et al., 2016; Hofmann et al., 2021) and an outer branch (Yermak branch) following the northern continental slope of Svalvard (Pérez-Hernández et al., 2016).

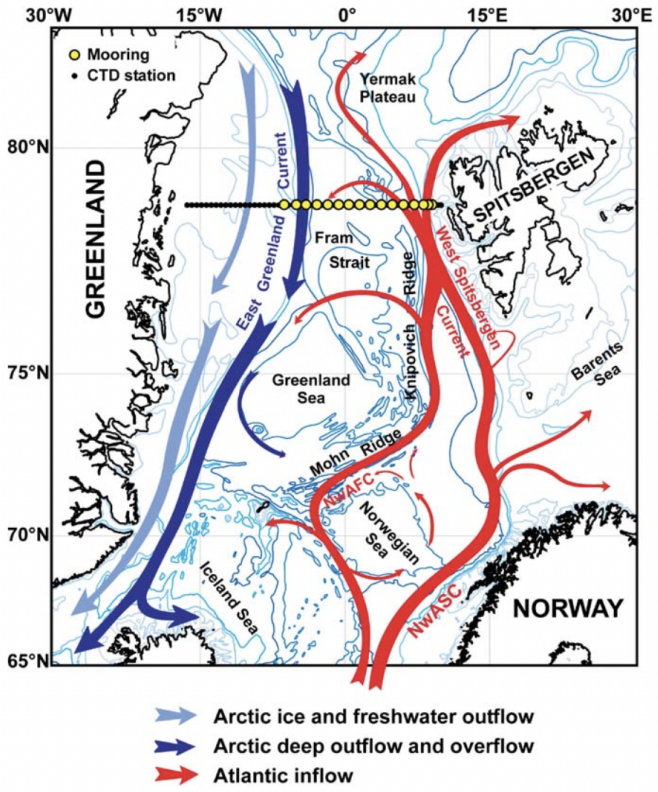

Figure 3. Schematic circulation for Fram Strait. Figure from Beszczynska-Möller et al. (2012).

On the western side, cold and fresh Polar Water (PW), sea ice, and modified AW exit the Arctic Ocean along the East Greenland Current (EGC). The EGC is characterized by a vertical three-layer structure (Håvik et al., 2017) consisting of

PW at the surface, a layer of modified and recirculated AW at right below with a thickness between 500-700 m, and an intermediate layer holding temperature below 0°C. Moreover, the boundary current system consists of distinct branches such as the outer EGC coinciding with the transition between the AW and the colder ambient water and the PSW jet above the shelf. Both branches are associated with a density front. The core of the EGC is characterized by an enhanced equatorward flow along the continental shelfbreak, previously referred to as the shelfbreak EGC (Våge et al., 2013) associated with an intermediate maximum in temperature. Another feature in the Greenland Sea is the omnipresent East Greenland Polar Front (EGPF) which exhibit large thermohaline gradients effectively separating Atlantic from Arctic originated water. Its position depends highly on the sea-ice edge (Liu et al., 2022), especially in northern summer when the sea ice retreats from the southeast outer shelf to the northwest shelf of Greenland: Beyond the shelf break, the front concentrates around the moving ice edge and when the sea-ice retreats behind it, the EGPF gets restricted to the shelf break followed by a decrease of its intensity.

1.3.2 Coastal upwelling systems

Sharp fronts are also common in upwelling systems, with the largest ones being located at the eastern side of the world's oceans (Chavez & Messié, 2009). The coastal upwelled water is cold and nutrient rich compared to the offshore water, and hence, separated by a front. This boundary can get unstable to instabilities promoting the formation of flowing structures such as eddies and filaments. By the example of the Mauritanian upwelling system offshore of the northwest African coast Hosegood et al. (2017) report a strong bloom produced by the the coastal upwelled water via sea surface temperature (SST) data and the westward advection along a filament by hundreds of kilometers. The filament was characterized by strong deep-reaching thermohaline gradients. In a recent investigation of the Cape Verde Frontal Zone (CVFZ), far west of the Mauritanian shelf, von Appen et al. (2021) also documented an $\mathcal{O}(20\,\mathrm{km})$ wide mesoscale upwelling filament and mesoscale anticyclonic mode water eddy.

1.3.3 The Equatorial Under Current

The largest longitudinally averaged thermal expansion coefficients are found in the area around the equator (Drushka et al., 2019) which is generally considered a representative of an alpha ocean. One prominent feature in the equator is the eastward directed Equatorial Under Current (EUC) that is driven by an interplay of a westward pressure gradient force driven by the meriodonally asymmetric wind system (Dietrich et al., 1975) and the absence of the Coriolis force at the equator.

The narrow EUC exists separately in the Pacific, Indian, and Atlantic Ocean and is of $\mathcal{O}(1\,\mathrm{m/s})$ fast-flowing nature. In the Atlantic, its core, associated with a local maximum in salinity (Blanke et al., 2002; Mathieu, 2019), shoals from around 100 m in the western basin to around 30 m depth in the eastern boundary (Talley et al., 2011). The top of the EUC is subject to high vertical shear, associated with large turbulence, due to trade wind driven westward flow of the surface water.

1.3.4 The Antarctic Circumpolar Current

A region that is subject to an intense wind field is the Southern Ocean, generally defined as the global ocean south of 35°S. Its flow is zonally not restricted by continental margins and is characterized by a continuous band of eastward movement of water, also known as the Antarctic Circumpolar Current (ACC), linking all major oceans. The ACC is structured by a series of fronts and following the 'traditional' view after Orsi et al. (1995) they are denoted as (from north to south) the Subantarctic Front (SAF), the Polar Front (PF) and the Southern ACC Front (SACCF). Each of them are circumpolar in extent, associated with deep-reaching jets, and highly steered by the bathymetry. Due to the latter the width of the ACC is not uniform and characterized by "choke points" with the strongest concentration in the Udintsev Fracture Zone (Park et al., 2019).

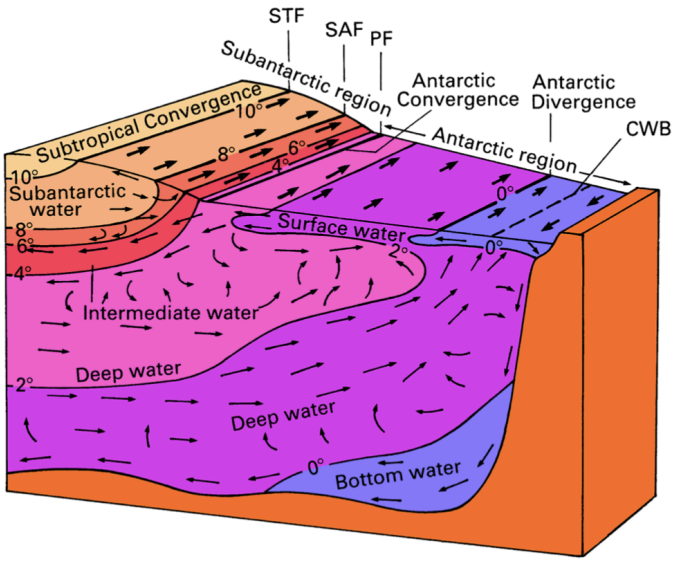

Figure 4. Schematic circulation across the ACC. (STF = Subtropical Front, SAF = Subantarctic Front, PF = Polar Front, CWB = Coastal Water Boundary). Figure from Tomczak and Godfrey (2003).

The main ACC fronts are occasionally expanded by the Southern Boundary, defined as the poleward edge of the Antarctic divergence (see Fig. 4). The surface divergence is a result of the strong westerly and easterly winds over and south of the ACC, respectively, contributing to the upwelling of North Atlantic Deep Water (NADW). As the deep water moves northward across the main fronts it gets

modified until it subducts as Antartic Intermediate Water (AAIW) north of the PF (Tomczak & Godfrey, 2003). The study of the fronts dates back to the 1920s and ever since diverse definitions are used leading to conflicting and confusing conclusions. The idea that the fronts' properties are variable in space and time is much more common now and in a recent review Chapman et al. (2020) provide a guide for the front detection in the Southern Ocean.

1.4 Research questions

In this thesis, the primary objective is the investigation of the multi-scale behavior of lateral density gradients based upon high-resolution subsurface CTD data obtained by a towed undulating system, which was operated from the surface down to 50 - 350 m in regions as different as Fram Strait, the equatorial/tropical Atlantic, and the Southern Ocean. In regard to the available data, we aim to answer the following key questions:

- To what extent does the lateral spatial scale impact the perception of a density gradient field?
- How do varying dynamical and oceanographic specifities manifest in the horizontal variability of the thermohaline structure?

This Master's thesis starts with the description of the collected data and methods we use (Chapter 2) involving a newly developed statistical pipeline. We then give an overview of the vertical sections and of their main hydrographic features (Chapter 3.1) before elaborating the scale-selective properties of their gradient field in density: The functionality of the pipeline is demonstrated by the example of multiple EGC crossings (Chapter 3.2) followed by an assessment of lateral density gradients up-scaled to worldwide regions with an additional focus on compensation and fractal properties (Chapter 3.3). The results are then subsequently discussed (Chapter 4). Finally, the end of this study contains a brief summary of our findings and concludes with an outlook and further recommendations (Chapter 5).

Chapter 2

Data and Methods

Hydrographic data used in this study were collected from the expedition MSM93 on RV *Maria S. Merian* and the three expeditions PS113, PS131, PS133.1 on RV *Polarstern* over the course of 3.5 years (2018 - 2022) in areas as varied as Fram Strait, the tropical Atlantic, and the Southern Ocean (Fig. 5). Despite their distinct objectives and research programs, they all relied on high-resolution underway data from the same towed system forming the foundation of this thesis. This section will provide detailed information on the different cruises and how data was acquired and processed. The analysis in regard to the gradient distribution over different scales relied on many steps of data-resampling, which will be addressed in this section as well as other derived variables for a complementing analysis. The software MATLAB was utilized for all steps in treatment and processing of data.

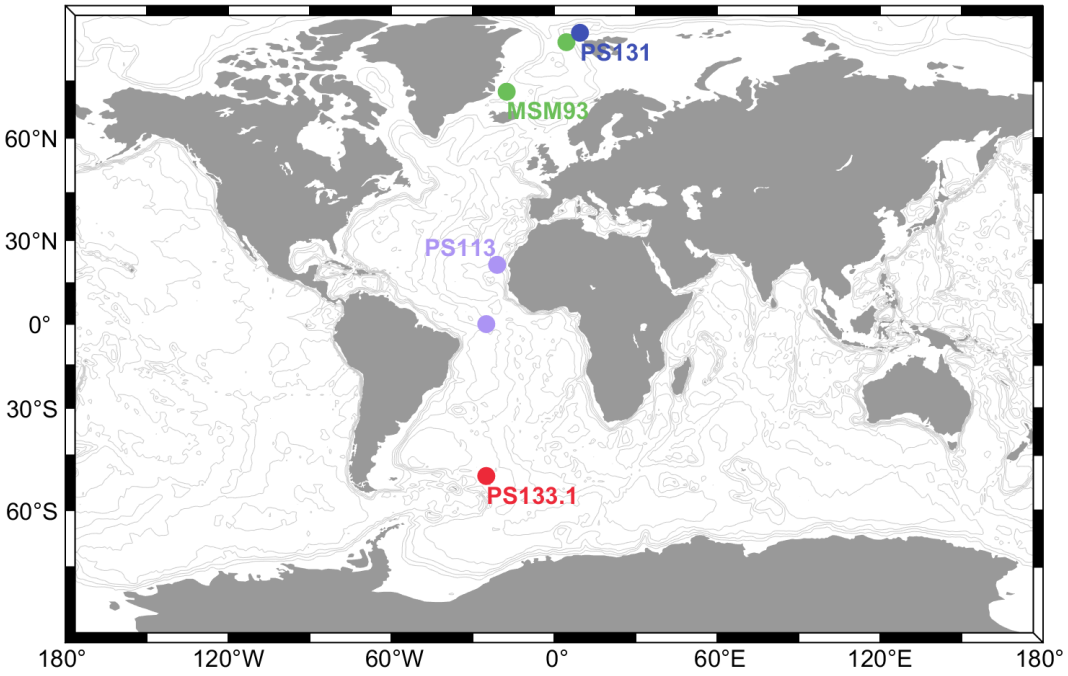

Figure 5. Global map with rough position of topAWI sections as indicated by colored dots, which are annotated with the name of the corresponding cruise: PS131 in blue, MSM93 in green, PS113 in purple, and PS133.1 in red. The map is overlain with bathymetry contours (in gray) spaced in 1000 m-intervals.

2.1 TRIAXUS

A TRIAXUS E (extended version) steerable towed system from MacArtney Underwater Technology was used for the collection of multiple transects (Fig. 6). It serves as a sensor carrier and is cuboid in shape - measuring 1.95 m in width, 1.25 m in height, and 1.85 m in length (MacArtney Underwater Technology, 2019). A towing cable tethers the system to the ship, provides power, and connects it to the deck unit via optical data transmission allowing a computer based control of the system in real time. Having flaps for vertical and horizontal steering, the system can be operated in different preassigned flight patterns. Such patterns include trajectories with a permanent distance to a reference source, with a fixed depth, and with a saw-tooth pattern undulating between two depths (Fig. 11b). A combination of the former and latter are possible. However, if the distance falls below the specified threshold to the reference source, the system will automatically begin the turn, leading to a turning point deeper than the set upper limit for some profiles. Trajectories are maintained by a built-in attitude sensor, depth sensor, and an upward looking altimeter. The platforms allows underway profiling at ship speeds between 2 and 8 knots (1 and 4 $\mathrm{m\,s^{-1}}$), undulations down to 350 m, lateral shearing up to 100 m on both sides behind the ship, and vertical speed up to 1 m/s.

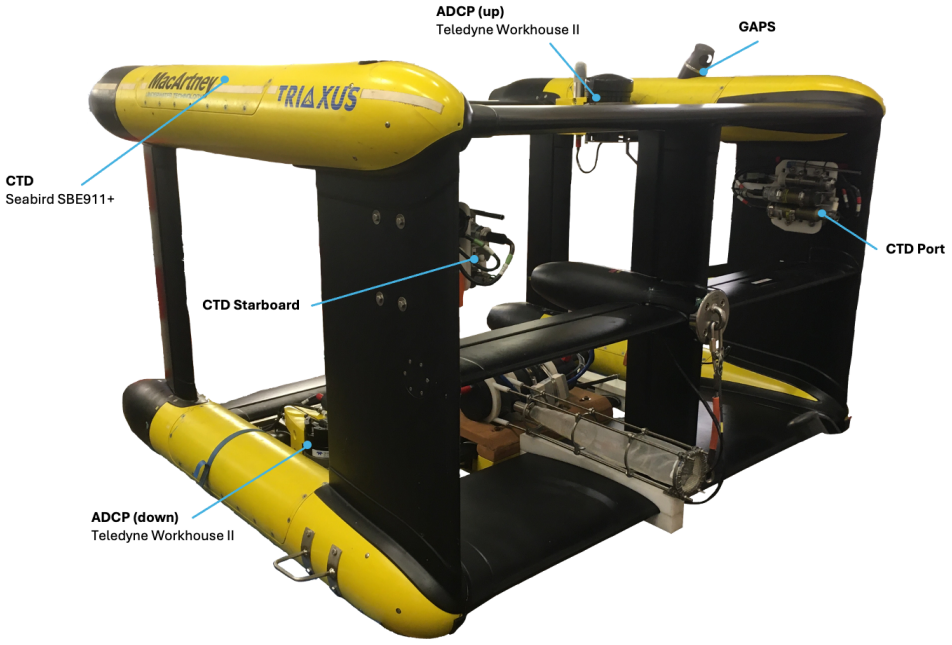

Figure 6. Sensor composition of the topAWI platform during PS133.1. The position of both CTDs and the pressure probe, the up- and downward looking ADCPs, and the GAPS system are marked by blue dots. Figure adapted from R. Mole (pers. comm. 2024).

The attachment of a set of selected sensors and equipment to the TRIAXUS forms the towed ocean profiler of the AWI (topAWI). This set includes a SeaBird SBE911+ with dual temperature and conductivity sensors, an SBE18 pH sensor, an SBE43 dissolved oxygen sensor, a WETLabs C-Star transmissiometer, a WETLabs WETStar environmental characterization optics (ECO) fluorometer, and a Satlantic photosynthetically available radiation 726 (PAR) sensor. Due to aforementioned possibility in maneuvering the system, these sensors can be used on a new scale, such as outside of the ship's influence, for under ice measurements, and for profiling with high horizontal spatial resolutions. In addition, the mounting position of the CTD, namely in the front area of the system, allows the usage of down- and upcast data as the probes are exposed to a permanent flow without any swirling of system parts. Additionally, a Gaps ultra-short baseline positioning (USBL) system is mounted on the Triaxus allowing to determine the position of the platform in the water with an accuracy better than $\pm 10\,\mathrm{m}$. Not used in this thesis, yet always part of the topAWI setup, is the acquisition of velocity data with a 1200 kHz upward-looking and 1200 kHz downward-looking acoustic Doppler current profiler (ADCP). The sensor composition is shown in Fig. 6.

2.2 Study site - Northern Fram Strait

Novel undulating under ice measurements were collected during the expedition PS131 **AT**latic **WA**ter pathways to the **ICE** in the Nansen Basin and Fram Strait (**ATWAICE**), which took place from June 27 to August 17, 2022. The topAWI was deployed in open water near the northern MIZ (Fig. 7) and a northward section crossing the MIZ on the Yermak Plateau north of Svalbard was initiated at July 16 at 80°20′N/10°36′E. The section is from now on referred to as MIZ1-1. The TRIAXUS was operated in a saw-tooth pattern with turning points at 10 m and 150 m depth and therefore outside of the water which is interacting with the sea ice. Data were acquired at a ship speed of 6 knots (3 m/s) and an undulating speed of 1 m/s. Consecutive upcasts were performed with a mean sampling interval of 700 ± 150 m. Due to the novel operation under ice using the technical capability of horizontal shearing was not used which resulted in casts occasionally measuring in the ship's wake. After $>$ 8 hours of underway acquisition over 85 km the section was interrupted at 81°00′N/08°38′E for 2.5 days due to station work and mooring deployment. The undulating platform was redeployed on July 19. Due to increasing ice coverage and harsher conditions in the inner MIZ the upper turning point was decreased to 15 m and then to 20 m before deciding to recover the TRIAXUS at 81°32′N/6°57′E. Over the total section distance of 147 km, 396 up- and downcasts were performed. Data can be found on PANGAEA (see von Appen, Kanzow, et al., 2023).

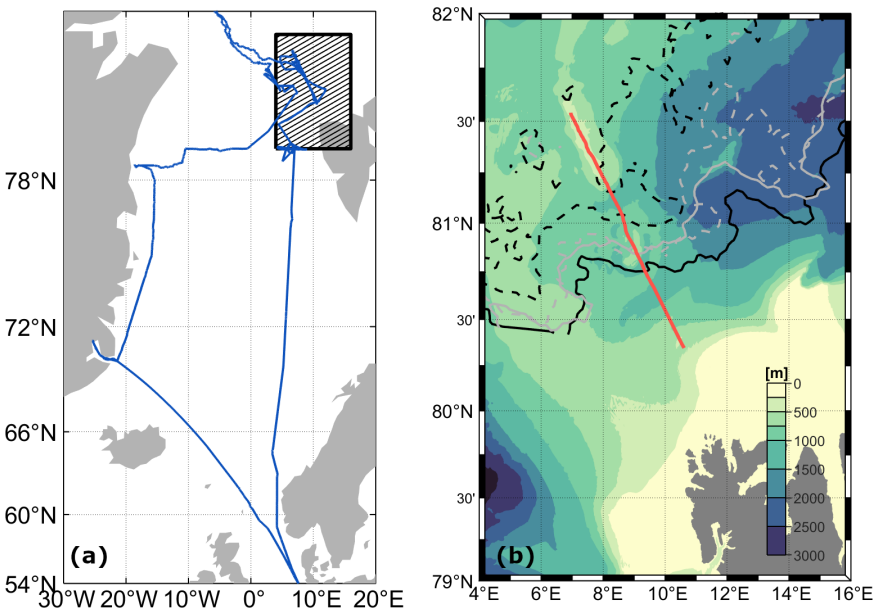

Figure 7. (a) Map of Fram Strait with black hatched boxes indicating the study region and the blue line indicating the cruise track of the PS131 expedition. **(b)** Study region northwest of Svalbard with regional bathymetry (GEBCO Compilation Group, 2021). Transect MIZ1-1 is indicated by the orange line and the SIC on 16 and 19 July 2022 are displayed as black and gray contours, respectively (dashed for 80% and solid for 20% SIC).

2.3 Study site - Central Fram Strait and EGC crossing

The TRIAXUS was heavily operated on the cruise MSM93 of RV *Maria S. Merian* in central Fram Strait and across the EGC (Fig. 8a). The expedition started on June 26, 2020 in Emden, Germany and ended there on July 30, 2020. The first and main working area is located between 79°15'N and 79°35'N and 2°45'E and 4°45'E (Fig. 8b) and involved an extensive study of a front between PW and AW in the open ocean region near the ice edge. The survey consisted, inter alia, of five transects, of which each was occupied multiple times with the undulating topAWI between July 14 and July 16. This thesis, however, only uses one of the occupations of the fifth transect along 79°30'N (from now on referred as FST1-1), which was conducted between 15-Jul-2020 00:36 UTC at 2°58'E and 15-Jul-2020 03:30 UTC at 4°40'E. Data were acquired in a saw-tooth pattern with turning points at 5 and 100 m at a ship speed of 5-6 knots (2.5 - 3 m s^{-1}) and a vertical speed of the sensor carrier of 1 m s^{-1}, resulting in an average horizontal resolutions of 600±30 m between consecutive upcasts/downcasts, respectively.

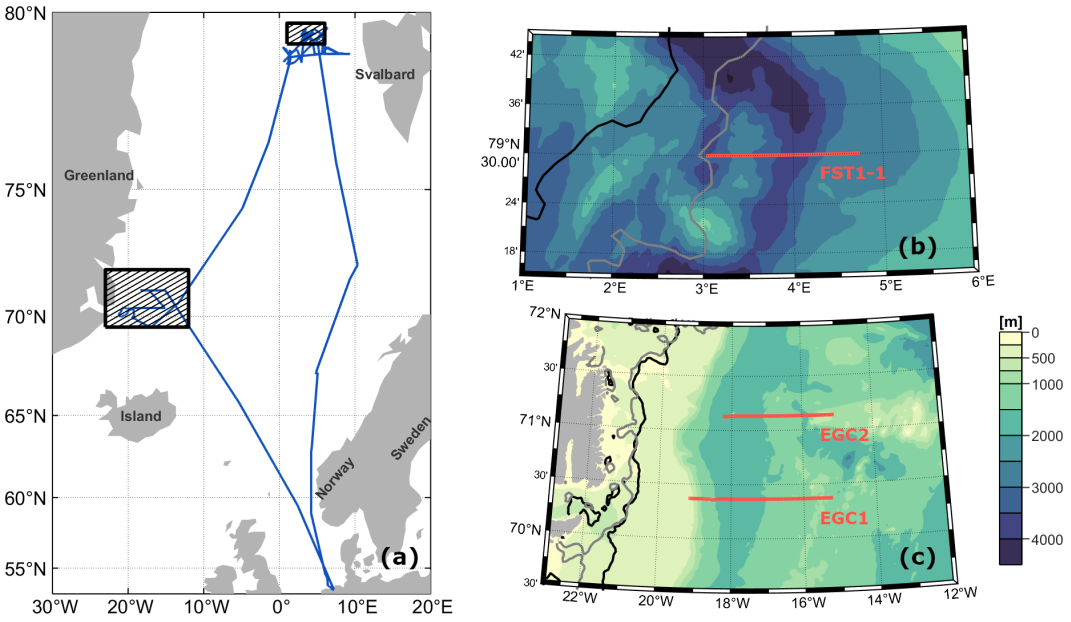

Figure 8. **(a)** Map of Fram Strait with black hatched boxes indicating the study regions and the blue line indicating the cruise track of the MSM93 expedition. **(b)** Study region in central Fram Strait with regional bathymetry (GEBCO Compilation Group, 2021). Transect FST1-1 is indicated by the line in orange and 20% SIC on 14 and 15 July 2020 are marked as black and gray contours, respectively. **(b)** Study region offshore of Scoresby Sund with the same bathymetry, as well as transect EGC1 and EGC2 in orange and the 20% SIC on 21 and 25 July as black and gray contours, respectively.

Further usage of the TRIAXUS happened across the EGC (Fig. 8c) near the shelf-break offshore of Scoresby Sund in East Greenland after sea ice conditions prohibited to enter the fjord for an intended recovery of moorings. With no improvement of the environmental condition, six TRIAXUS sections were conducted instead. The

first three sections were occupied along 70°21'N between 21 July and 24 July, 2020 and are assigned to transect EGC1 as EGC1-1, EGC1-2, and EGC1-3. All three sections were initiated with little delay between each other. However, the conduction of EGC1-3 was interrupted due to technical problems on 22 July for more than 20 hours after an along-track distance of about 37 km and redeployed the day after. The remaining sections were conduced further north along 71°08'N on 24 July 2020 and 25 July 2020 and are assigned to transect EGC2 as EGC2-1, EGC2-2, and EGC2-3. The flight pattern of the device carrier was alternately switched between a saw-tooth and fixed-depth pattern from section to section (cf. Table 1) contributing to horizontal profile spacings varying between $\mathcal{O}(\mathrm{m})$ and $\mathcal{O}(\mathrm{km})$. Data can be found on PANGAEA (see Hofmann et al., 2022).

2.4 Study site - Equatorial/Tropical Atlantic

The topAWI was for the first time tested and commissioned during the expedition PS113 of RV *Polarstern* across major oceanographic regimes of the Atlantic, from Punta Arenas, Chile, to Bremerhaven, Germany (Fig. 9a). The cruise started on May 8, 2018 and ended on June 11, 2018. The research program involved intensive testing of the platform under various operational settings. Among the testing, two long TRIAXUS transects were occupied in areas with expected strong gradients at a ship speed of 8 knots (4.1 m s^{-1}) that will be used in this thesis. The first one (Fig. 9c) was conducted, after finishing a parallel course to the coast of South America, along 25°W across the equator from 24-May-2018 13:37 UTC at latitude 2°S to 25-May-2018 22:41 UTC at latitude 2°N. The section is from now on referred to as EQT1-1. The platform undulated between 3 and 300 m, and more than 150 casts were performed over a distance of 460 km. A 278 km long section was occupied offshore of northwest Africa in the Cape Verde Frontal Zone from 19°51'N/21°08'W to 22°25'N/20°34'W (Fig. 9b) with a saw-tooth pattern between 3-4 m below the surface down to 350 m depth. The section, from now on referred to as CVF1-1 was initiated on 30-May-2020 17:30 UTC and ended on 31-May-2020 16:00 UTC. 111 up- and downcasts were performed with an average horizontal distance of around 2.5 km between subsequent down- and upcasts, respectively. Data can be found on PANGAEA (see von Appen et al., 2019).

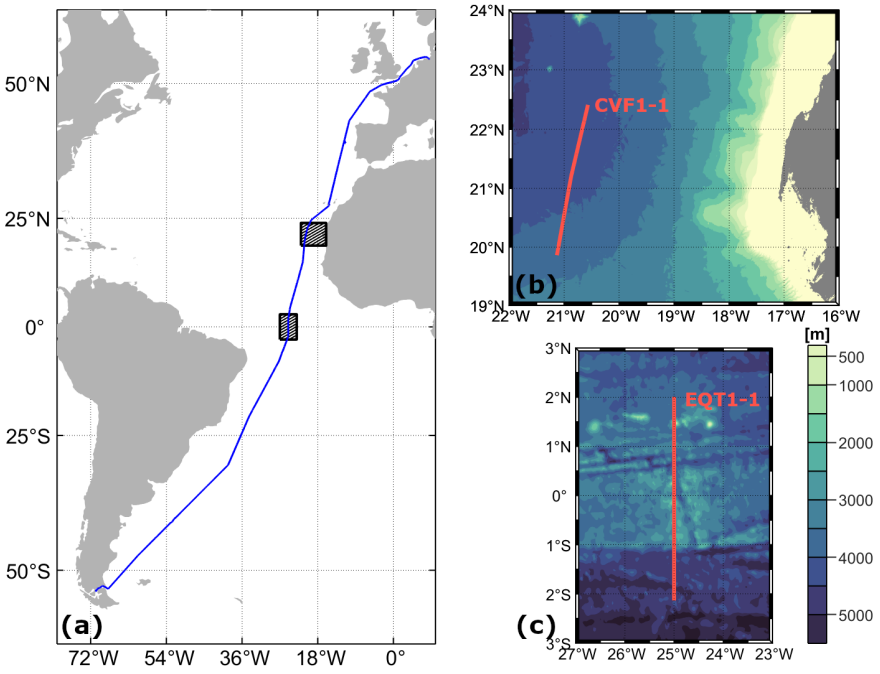

Figure 9. (a) Map of the Atlantic with hatched boxes indicating the study regions and the blue line indicating the cruise track of the PS113 expedition. **(b)** Study region in the upwellig region offshore of the northwest African coast with regional bathymetry (GEBCO Compilation Group, 2021). Transect CVF1-1 is indicated by the line in orange. **(c)** Equatorial crossing EQT1-1 as orange line with the same bathymetry.

2.5 Study site - ACC crossing

The most recent operation of the towed system occurred in the expedition PS133-1 of RV *Polarstern*. The cruise started on October 2, 2022 in Cape Town, South Africa and ended on November 17, 2022 in Punta Arenas, Chile (Fig. 10a). The topAWI/Triaxus was towed along one long transect at longitude 25°W, from now on referred to as ACC1-1, crossing the main flow of the ACC (Fig. 10b). The section was conducted on 19-Jul-2020 22:56 UTC at 49°30'S north of the Polar Front and was finished after crossing the Southern Boundary on 20-July-2020 15:05 UTC at 54°00'S. The towed vehicle was operated in a saw-tooth pattern undulating between 15 m and 300 m providing a 500 km long section of measurements with an average horizontal resolution of 1.9 km. 511 profiles were obtained. Due to the rougher weather in the Southern Ocean with high seas up to 4 m, the cable tension varied between 3000 and 7000 N with an earlier reaction of the automatic overload function of Triaxus software as a consequence. Therefore, some upcasts were initiated significantly above the preset lower turning point. Data can be found on PANGAEA (see von Appen, Hölemann, et al., 2023).

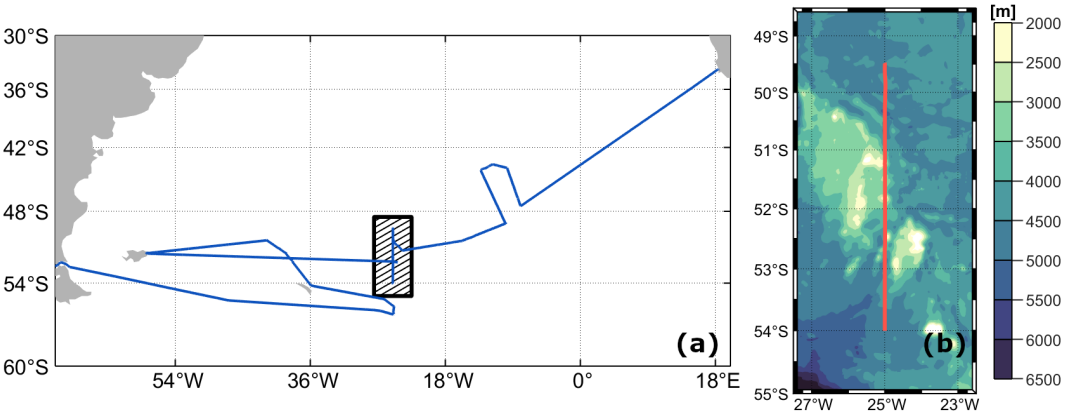

Figure 10. **(a)** Map of the Southern Ocean with black hatched box indicating the study region and the blue line indicating the cruise track of the PS133-1 expedition. **(b)** Study region across the ACC with regional bathymetry (GEBCO Compilation Group, 2021). Transect ACC1-1 is indicated by the orange line.

Table 1. Overall list of TRIAXUS sections with the minimum and maximal turning point [m], along-track distance [km], mean spatial resolution between upcasts [m], mean temporal resolution between upcasts, and the baroclinic Rossby radius of deformation R_d [km] of the study regions after Chelton et al. (1998).

Section	Min Depth [m]	Max Depth [m]	Distance [km]	Spatial/temporal resolution $\mu \pm \sigma$ [m]/[mm:ss]	R_d [km]
MIZ1-1	10	150	147.4	700 ± 150/ $04{:}17 \pm 00{:}08$	6
FST1-1	5	100	34.5	600 ± 30/ $03{:}00 \pm 00{:}02$	5
EGC1-1	5	300	146.7	1900 ± 250/ $09{:}15 \pm 00{:}02$	9
EGC1-2	10	10	160.4	2.3 ± 2.0/ -	9
EGC1-3	5	50	146.1	300 ± 50/ $01{:}16 \pm 00{:}11$	9
EGC2-1	10	10	123.1	2.3 ± 2.0/ -	9
EGC2-2	5	50	111.7	300 ± 90/ $01{:}17 \pm 00{:}04$	9
EGC2-3	30	30	124.4	2.3 ± 2.0/ -	9
EQT1-1	3	300	460.3	2900 ± 380/ $11{:}28 \pm 00{:}06$	230
CVF1-1	3	350	284.1	2500 ± 300/ $10{:}57 \pm 00{:}10$	46
ACC1-1	15	300	502.1	1900 ± 460/ $08{:}50 \pm 01{:}00$	14

2.6 Preprocessing

In preparation for the analysis presented in this thesis, the raw data sets underwent essential pre-processing steps. While the details of these procedures are not the primary focus of this study, we would like to give a brief summary, as without these steps, the data would have been unsuitable for meaningful analysis. Standard SeaBird routines were applied to the raw data including low pass filtering of the pressure data, cell thermal mass correction, and the removal of outliers. In case of undulating sections, the up- and downcasts were determined from the vertical velocity of the CTD sensors. In order to find the depth offsets, which are caused by the different placement of the sensors on the rigid frame relative to pressure sensor, a pitch and roll analysis was performed on the undulation transects. Another lag that had to be considered is the temporal lag attributed to the different sensor response times, which is especially large for the conductivity sensors. As an attempt to determine the time lag and correct the data in time in regards to the data of the temperature sensor, a correlation analysis between all upcast-downcast and downcast-upcast pairs was performed. In order to reduce further inconsistencies from sensor lags, data from up- and downcasts will, however, be handled separately in analysis. A detailed description of the preprocessing is found in (Hofmann et al., 2024). Further processing, that is actually performed within the scope of this thesis will be addressed in the next paragraph.

2.7 Data Gridding

The preprocessed data sets included all values between the deployment and the recovery of the undulating system. Thus, we remove any data that do not align with the intended sections. We use a criterion where we flag values when the CTD sensors deviate by more than a specific threshold from the preset turning points. For the determination of the start and end point of each section, this threshold is set to ± 2 meters (Fig11a). For undulations within the intended section this criterion is rather used as an indicator only, and profiles with large deviations from the target depths, as well as intermittent stops are identified by visual inspection of depth time series and then removed, if necessary. In case of constant depth tows, the threshold is extended to ± 5 meters and used strictly throughout the total section. Moreover, location time series are also inspected in order to sort out values that were not acquired over a straight line.

Along-track distances x are then computed for each profile. Despite their tilt along the water column, values of each profile are assigned to the same coordinates from the measurements collected at the middle of each undulation. The first profile to be completed is used as a reference point $x_0 = 0\,\mathrm{km}$. For the multiple

occupations of the EGC crossings, the western most profiles are used as x_0 independently of the time of completion. As further analysis will only rely on relative distances, an additional correction by the cable length is left out.

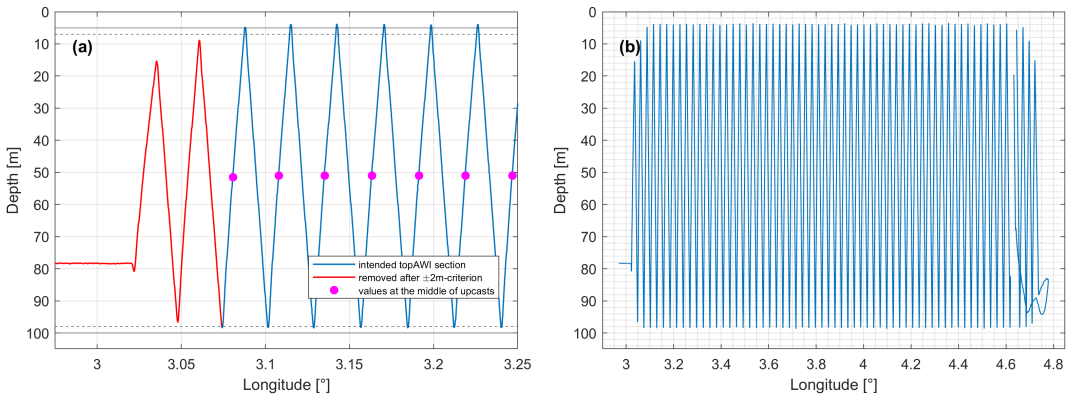

Figure 11. **(a)** Exemplary subset of sawtooth profiles subdivided in values removed from analysis (in red) not satisfying the ±2m-criterion (dashed gray lines) and values of intended section (in blue) of preset turning points (gray lines). The magenta points indicate the value at the middle of the respective upcast. **(b)** All undulations plus deployment/recovery operations along section FST1-1 conducted between 15-Jul-2020 00:36 UTC and 15-Jul-2020 03:30 UTC along 79°30'N.

The undulating measurements from the Triaxus are gridded with the minimum curvature method with an added tension parameter (W. H. Smith & Wessel, 1990). The tension parameter is set to 5, where 0 corresponds to Laplacian interpolation resulting in tent pole-like behavior around data points, and ∞ corresponds to spline interpolation offering a smoother field with the potential for spurious peaks or valleys. The results are checked by visual inspection validating a grid closely aligned with the actual measurements. By applying a search radius of ±20 grid points, an uniform grid is achieved covering even depths of limited data due to deviations from the preset undulations depths (for example, sections conducted during PS131 and PS133.1). Data of each section are interpolated onto a regular grid with a vertical grid size of 0.5 m and an individual horizontal grid size corresponding to the mean distance between up- and downcasts, respectively (cf. Tab.1). All grids extend over a horizontal distance of 0 km to the length of the section, and over individual depth ranges defined by the preset turning points. Measurements from up- and downcasts are gridded independently. A linear interpolation was applied on measurements from the constant depth sections, that is EGC1-2, EGC2-1, and EGC2-3, by simply using the interp1() of MATLAB.

2.8 Data Resampling

The data resampling basically counts on the conceptual two-step progression of a so-called decimator (Crochiere & Rabiner, 1983), a multirate-filter that reduces the sampling frequency f_s of an one dimensional input series $x(n)$ with sampling indices n by a factor Q. The process initiates by applying a 4th order Butterworth filter to $x(n)$ for low-pass filtering. The cutoff frequency of the filter is set at four times of the targeted resampling rate f_s/Q. In digital processing, this step is used as an anti-aliasing filter to obtain an output sequence $w(n)$ with reduced bandwidth, ensuring adherence to the Nyquist theorem when compressing it. However, in this context, our goal is merely to obtain a coarser representation of the data without any intention of reconstructing the original signal. Hence, the filter is applied for the reduction of high frequency noise only and the subsequent decimation is not constrained by the Nyquist frequency. The second step involves the actual resampling of the now smoothed output sequence $w(n)$ with an integer down sampling of Q-to-1, that is to say every Q-th value is kept starting at index 1 and interim samples are removed.

In this study, we resample the topAWI/TRIAXUS density data along the horizontal spatial scales. Signal filter leverage on the capabilities of a Fourier transform to decompose and manipulate a signal in terms of their frequency components. This involves the removal of the mean and a linear trend, usually handled within the routines. Note that we, however, have to use the potential density anomaly σ_θ for the analysis, as the background constant of $1000\,\mathrm{kg\,m^{-3}}$ lead to undesired responses of the low-pass filter. In case of sections conducted with an undulating pattern, measurements from the same depth are treated as individual input series. Moreover, measurements from up- and downcasts are manipulated independently. Therefore, an M x N data grid, where z and x are (M x N), results in 2M individual input series on which the subsampling routine is applied to. On the other hand, data of topAWI/TRIAXUS sections at constant depth, such as EGC1-2, EGC2-1, and EGC2-3 are one-dimensional already, not affected by the sensor lag that comes with undulating tows, and could simply be passed into the resampling routine. Every data series (>3000 in total) is subsampled between the initial horizontal resolution dx, corresponding to $Q = 1$, and the length of the section (only considering the first and last value of $w(n)$). From every resampled data series $w(m)$ with sampling indices $m = n \cdot Q^{-1}$ we compute the density differences $\Delta\rho$ between adjacent sampling values. A subsequent multiplication with f_s/Q produces a new data series of density gradients $\nabla\rho$ assigned to a fixed sampling interval, henceforth referred to as the length scale λ.

While the data gridding as described in 2.7 accounted for a spatial continuity of the input series, temporal breaks that occurred in the data acquisition such as in EGC1-3 and MIZ1-1 would not be considered in the resampling routine presented

so far. In order to avoid the computation of density gradients between closely spaced sampling points over an extended time lapse, additional adjustments were implemented for resampling the aforementioned sections: First, we define the area $A = \{(x, \rho) \,|\, |x_0 - x| \leq R_\mathrm{d}\}$, whereby R_d is the Rossby radius of deformation and x_0 marks the along-track distance at which the data acquisition had been continued after a significant temporal break. The gradient computation is based upon two sampling values in density $\rho_\mathrm{i} = \rho(x_\mathrm{i})$ and $\rho_{\mathrm{i}+1} = \rho(x_{\mathrm{i}+1})$. The removal of a gradient from further analysis involves two conditions: First, at least for one of the two sampling points $\rho \in A$ must hold, which could simply be performed by assigning all data points within A to NaN values. While this approach would be quick to implement technically, it leads to a loss of valid gradients which we is to be avoided, especially for undulating tows. Therefore, we additionally demand the crossing of x_0, which allows to maintain gradients computed between x_0 and $x_0 \pm R_d$.

For every section a .mat-file is saved with one structure for each depth grid containing the respective density gradients, length scales, and absolute along-track positions.

2.9 Assessment of scale sensitivity

In order to study the sensitivity of lateral density gradients to the spatial resolution, we make use of descriptive statistics such as bivariate histograms - a graphical representation of the joint distribution of two continuous variables, namely the horizontal density gradients and the length scales. The range of each variable is divided into bins with bin sizes of $0.005\,\mathrm{kg\,m^{-3}\,km^{-1}}$ and 0.1 km, respectively, along two axes and the number of observations falling into each pair of bin intervals is counted. The resampling routine as described in 2.8 yields a decreasing number of samples as the length scale is incrementally increased for which reason the frequency of observations in each bin is not displayed by the raw number count. Instead, the relative occurrence of observations is visualized and used in further analysis by shading the joint distribution with the percentage count of each gradient for each length scale bin. This normalization prevents the bias by the absolute number of samples.

The evaluation of the joint distributions between horizontal density gradients and length scales is initiated by a visual inspection, which is done to find trends or patterns. While this approach might provide first insights into the scale sensitivity of density gradients, it is not standardized and less suitable to compare hundreds of histograms. Therefore, we draw on repeatable and automated approaches such as the computation of the marginal and conditional means of the density gradients, which are the mean value over all gradients and the mean value of gradients for

each length scale bin, respectively. The standard deviation is computed to imply the uncertainties of these values.

Yet, in order to compare various distributions, we mainly opt for a parametrization of each histogram by obtaining the 99%-envelope and other relevant percentage marks and fitting each of them to a power law function of the form ax^{-k} with the normalization constant a and the exponent k. This is achieved by placing the joint distribution of absolute density gradients $|\nabla\rho|$ and lateral length scales λ on a double-logarithmic scale, which enables a linear regression analysis as a power law function appears as a straight line when double-logarithmic scaled:

$$\log(\nabla\rho) = -k\log(\lambda/\lambda_0) + \log(a) \tag{1}$$

where $-k$ and $\log(a)$ are the slope and the intercept in log-log-space, respectively. The length scale is normalized by $\lambda_0 = 1\,\mathrm{km}$ in order to obtain consistent units for both parameters. The slope (or exponent in linear space) can be used as a measure of the decay rate of gradients with increasing length scales and a (factor in linear space) serves as an indicator for the magnitude or strength of the density fronts. A beforehand re-categorization of the data pairs $(\lambda, \nabla\rho)$ onto equally double-logarithmic bins prevents an increasing resolution with the length scale and therefore a regression line that is biased toward large spatial scales. This is because the regression process will give more weight to regions with more data points and thereby bias the best-fit parameters toward the distribution in the mesoscale. In order to evaluate the statistical significance of both parameters, uncertainties in the best-fit coefficients (95%-confidence intervals) are estimated by the use of the `polyparci` function of MATLAB. For undulating sections, the starting index in the subsampling process was moved between 1 and Q-1 in order to increase the denseness of the histograms and thereby improve the robustness of the parametrization.

2.10 Fractal dimension D

The estimation of the fractal dimension, a measure for statistically self-similar geometric feature, depends on the fractal length, which is defined as a function depending on the horizontal length scale λ (McHardy & Czerny, 1987; Wijesekera, 1996):

$$L(\lambda) = \frac{1}{\lambda}\int_0^{\Delta x} |F(x+\lambda) - F(x)|\,dx \tag{2}$$

where F is any function of the horizontal distance x, such as our gridded data series of potential density. The horizontal length scale varies between the initial resolution dx of F and the total sampling length Δx of the gridded data series, which are different for each of the conducted topAWI/Triaxus sections. The unit of $L(\lambda)$

equals the one of the function F, in this study [kg m^{-3}]. The fractal dimension is given by

$$D = -\frac{d\ln[L(\lambda)]}{d\ln[\lambda]} \tag{3}$$

and varies between 0 and 1 as we are considering a one-dimensional problem. A fractal dimension of 1 implies a high small-scale fluctuations in the evaluated density signature. Due to the linearity property of integrals, we are allowed to pull λ^{-1} into the integral. By doing so we can capitalize on the resampling algorithm as described in 2.8 whose output can directly be used for the computation of $L(\lambda)$. The fractal lengths are plotted against the length scales and D can then be estimated by fitting a regression line following equation (3).

2.11 Density ratio R_ρ

To explore the relative contribution of temperature and salinity variations to the lateral density gradients, the density ratio R was estimated:

$$R_\rho = \frac{\alpha\nabla T}{\beta\nabla S} \tag{4}$$

where $\alpha = \rho^{-1}(\partial\rho/\partial T)$ and $\beta = \rho^{-1}(\partial\rho/\partial S)$ correspond to the thermal expansion and haline contraction coefficient, respectively. The coefficients are computed using the MATLAB routine of the *gsw* toolbox. ∇T and ∇S are the horizontal gradients in temperature and salinity, respectively, and are obtained over a wide range of spatial scales with the help of the subsampling routine as described in 2.8. As we only consider absolute gradients, the density ratio will vary between 0 and ∞. Full compensation is represented by $R_\rho = 1$ and deviations indicate uncompensated lateral gradients dominated by either temperature ($R_\rho > 1$) or salinity ($0 < R_\rho < 1$).

In order to avoid infinite values, which occur when the salinity variations fade, we follow Rudnick and Martin (2002) and look at the Turner angle Tu:

$$Tu = \arctan(R_\rho) \tag{5}$$

which offers the advantage that regions dominated by temperature and salinity occupy areas of equal size on the Turner axis (from 0 to $\pi/2$) and a more effective handling of $\nabla S = 0$. Note that other formulations of Tu involving R_ρ exist (e.g. Stewart & Haine, 2016) with an offset of $-\pi/4$. Definitions are mathematically equivalent, but due to the boundary shift, which is sometimes introduced to distinguish the vertical and horizontal Turner Angle (e.g. Tippins & Tomczak, 2003), direct comparisons with other studies should be performed carefully.

2.12 Buoyancy frequency N^2

The stratification and stability of the water column can be indicated with the buoyancy frequency squared N^2 representing the vertical gradients of potential density ρ along a water column. It is calculated from density profiles for each depth grid point j with a vertical grid interval of $\Delta z = 0.5\,\mathrm{m}$:

$$N(j)^2 = \frac{g}{\rho(j)} \cdot \frac{\rho(j-1) - \rho(j+1)}{2\Delta z} \tag{6}$$

where g is gravity and is calculated from the latitudes of each profile using the MATLAB routine of the *gsw* toolbox. In order to remove data noise from the highly resolved vertical grid, each density profile is low-pass filtered by a 4th order Butterworth filter with a cutoff frequency of 5 m prior to the application of equation (6). Further smoothing is achieved by a centred difference of $2\Delta z$, which, however, leads to a loss of a value at the top and the bottom of the vertical grid. Thus, a NaN is inserted for each, ensuring the grid remains consistent. The leveling of the density data contribute to a significant reduction of negative values. Remaining negative values are set to the smallest positive value calculated for each profile. As N^2 can vary over several orders of magnitude, the analysis in regard to the stratification is performed by looking at the logarithm of N^2 compressing the wide range of values into a more manageable scale.

2.13 Mixed Layer Depth

In order to compare the lateral variability of the density field within a quasi-uniform layer of ρ, such as the mixed layer, and within the stratified interior, the mixed layer depth (MLD) was determined from individual profile data. Therefor a difference criterion was used, which requires the deviation of ρ from a reference value (uppermost measurement of corresponding profile). The difference criterion is subjective (Chu & Fan, 2011) and depending on its choice it can lead to significantly different MLDs (Treguier et al., 2023). A threshold of $0.05\,\mathrm{kg\,m^{-3}}$ produced results that satisfy the needs of the present work, and therefore, was utilized for all study regions. In the statistical part of the analysis, the MLD for each section will refer to the mean of all corresponding along-track values computed.

Chapter 3

Results

This section is divided into multiple parts. First, hydrographic transects will be depicted in order to get an idea on the different study areas and their characteristic features. In another part, the sensitivity of horizontal density gradients to the spatial sampling rate will be assessed using the developed subsampling method. Its functionality is demonstrated using the example of the EGC sections followed by an upscaling of the analysis to the other oceanic regions. The third part involves the study of fractal properties, absolute gradient values, and *T*-*S* contribution, as a way to support observations made by the new multi-scale routine.

3.1 General hydrography

3.1.1 East Greenland Current

EGC1

The first and deepest occupation of transect EGC1 is seen in Fig. 12 and reveals a remarkably similar hydrographic structure as described by Håvik et al. (2017). A layer of water with relatively low potential temperature (< 0°C) is found above the shelf break extending eastward across most of EGC1-1 to an along-track distance of 115 km (Fig. 12a), where it meets a maximum in potential temperature. This cold surface layer reaches a depth of 120 m, thins down by around 40 m offshore, and holds water with a potential density anomaly smaller than 27.7 $\mathrm{kg\,m^{-3}}$ (Fig. 12c) fitting into the PSW definition after Rudels et al. (2002) . An intermediate maximum in potential temperature is located in the vicinity of the shelfbreak right below the fresh PSW layer at approximately 120-240 m and progressively weakens to the east and to greater depths. This intermediate layer of warmer and saltier water corresponds to the Atlantic-origin layer and is restricted to the east by colder ambient water of the Greenland Sea. The transition between the two water masses coincides with the outer edge of the PSW layer and is associated with a pronounced upward tilt of the 27.95 and 28 $\mathrm{kg\,m^{-3}}$ isopycnals indicating the outer branch of the EGC

(marked with green triangle). Colder water appears also deeper in the water column at depths between 200 - 300 m between 60 and 90 km, but due to the shallowness of the section it remains unclear whether it indicates the lower intermediate layer or just an intermittent disruption of the Atlantic-origin layer. A minimum in salinity is located between the western end of the transect and $\approx$ 55 km (Fig. 12b), where the 0 °C isotherm and the 26 kg m^{-3} isopycnal outcrop to the surface. Proceeding from this well-mixed freshwater plume, salinity values increase rather gradually offshore and a thin layer of warmer water presumably due to summer insolation overlies the PSW layer. A subsurface front between PSW and Atlantic-origin water is present at 25 km accompanied by a slight shoaling of the 27.6, 27.7, and 27.8 kg m^{-3} isopycnals possibly indicating the Shelfbreak EGC. A clearer identification would require, however, the evaluation of absolute geostrophic velocity, which we did not calculate here as it is out of scope of the main goal of this thesis. Aforesaid isolines in density separate a fresher surface from the more saline interior along the total section exhibiting no significant tilting throughout the rest of the PSW layer and eventually come together at 115 km isolating the warm surface water from the cold and saline ambient water.

The distribution of the buoyancy frequency squared, N^2, is depicted in Fig. 12d. A line of high values in N^2, suggesting a strong stratification, is located at around 20 m depth within the PSW exhibiting a step-wise deepening by 10 m around 60 km and by another 10 m around 100 km. Proceeding from this main pycnocline, stratification weakens to greater depths, whereby the AW layer appears to be slightly more stable than the stratification in the ambient water of the Greenland Sea. A highly stratified surface layer is present along the entire section, probably as a result of the melt water, indicative for the absence of a mixed layer or the presence of a very shallow one. Note that negative values in the buoyancy frequency squared, caused by measurement or interpolation errors, have been replaced with the lowest positive value which explains the intermittent occurrences of weakly stratified water.

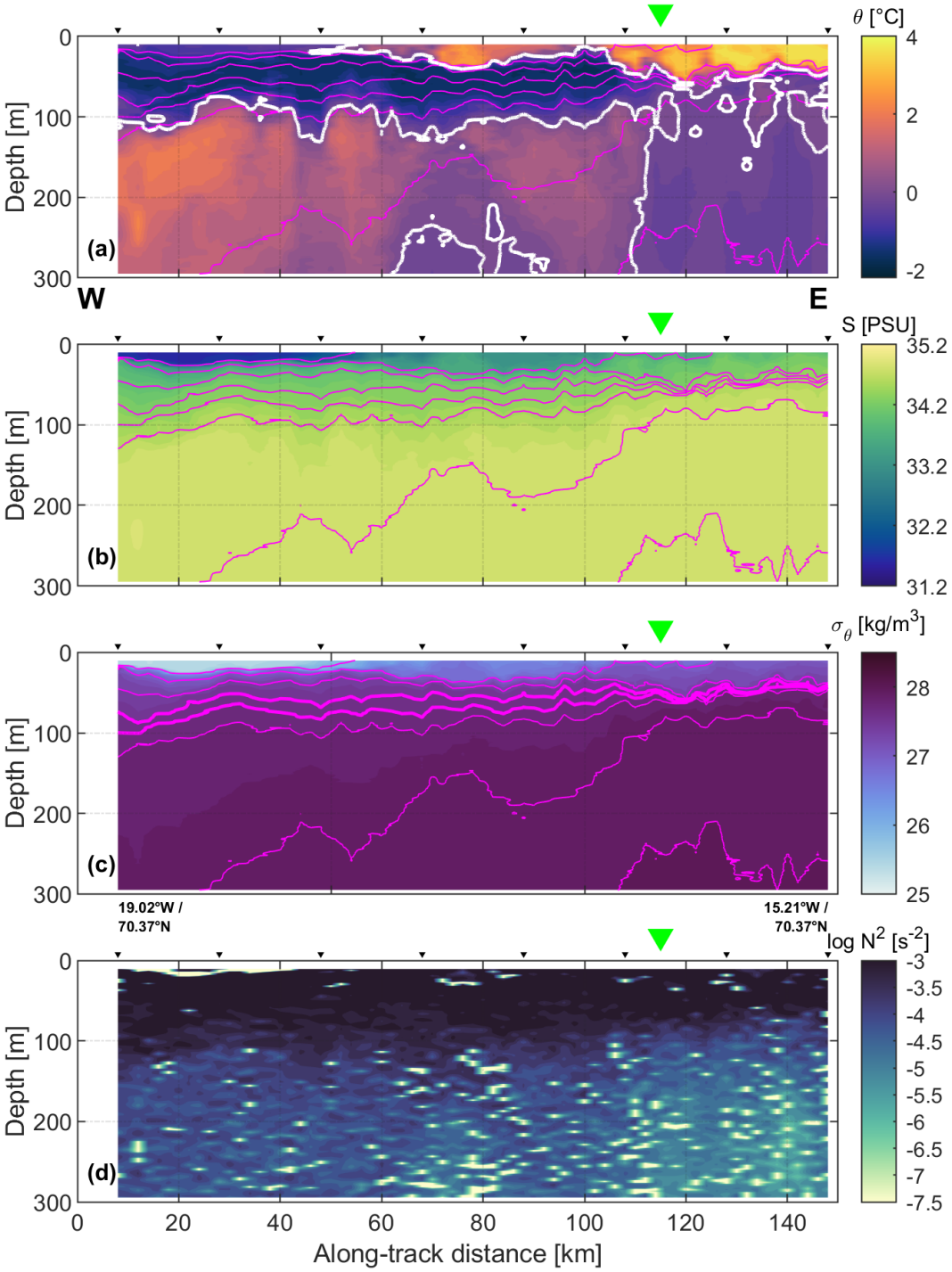

Figure 12. Gridded vertical sections along EGC1-1 of **(a)** potential temperature (θ) [°C], **(b)** salinity (S) [PSU], **(c)** potential density anomaly (σ_θ) [kg m^{-3}], and **(d)** the logarithm of the buoyancy frequency squared (N^2) [s^{-2}]. The magenta lines in **(a)** - **(c)** indicate the 26-, 27-, 27.4-, 27.6-, 27.7-, 27.8-, 27.95-, and 28-isopycnals; for guidance reasons the 27.6 and 27.7 kg m^{-3} isolines are displayed as thick lines in **(c)**. The white line in **(a)** represents the 0°C-isotherm. The reference point (0 km) for the along-track distances corresponds to 70.37°N/19.17°W. Coordinates of section start and end are given below **(c)**. Small black triangles on top indicate every tenth individual profile and the large green triangles indicates the offshore boundary of the EGC.

A horizontally more detailed look on the transition between the EGC and the open ocean was achieved along EGC1-3 (Fig. 13). Potential temperature (Fig. 13a) reveals a downward sloping of the 0°C isotherm to the east possibly indicating the subduction of the PSW layer below warmer surface water from the open ocean. This overlying water, which was in general less saline and dense (Fig. 13b,c) than the water laterally adjacent to the PSW layer, showed a local maximum in potential temperature and salinity at 75 km associated with a pronounced deepening of the 0°C isotherm and 27 $kg\,m^{-3}$ isopycnal to about 45 m depth. A distinct change in regimes at 105 km presents the offshore boundary of the PSW layer and was accompanied with closed isopycnals, which are usually associated with instabilities in the density field. Oceanic fronts can become unstable to instabilities that form mixed layer eddies, but due to the rare prevalence of density instabilities during in-situ observations we assume that those measurements might have arisen from a combination of noise, salinity spiking, and the tilt of the profiles. Note, that typical oceanographic observations usually do not have the spatial resolution to resolve such instabilities. While a pronounced tongue of melt water accounted for the upper 20 m of the PSW layer right before it gets subducted below solar warmed water, the open sea regime offshore of the EGC reveals less obvious features such as slightly colder and fresher water at the surface between 120 and 135 km exhibiting a filamentous structure and bits of the intermediate ambient water close to the lower end of the undulating pattern. The regime change is also highlighted by a drastic change of N^2 (Fig. 13d), which is apparent at 80 km. The EGC region is characterized by a water column that is stratified to the uppermost measurements, while the solar warmed water east of it holds much lower values in N^2. Moreover, the step-wise progression of a highly stratified layer as found in Fig. 12d from west to east follows the base of the freshwater plume, then the upper boundary of the PSW layer, and then the boundary between solar warmed water and the deeper ambient water. A disruption of this layer was found between 60 and 80 km, where the local deepening of the 0°C-isotherm occurred.

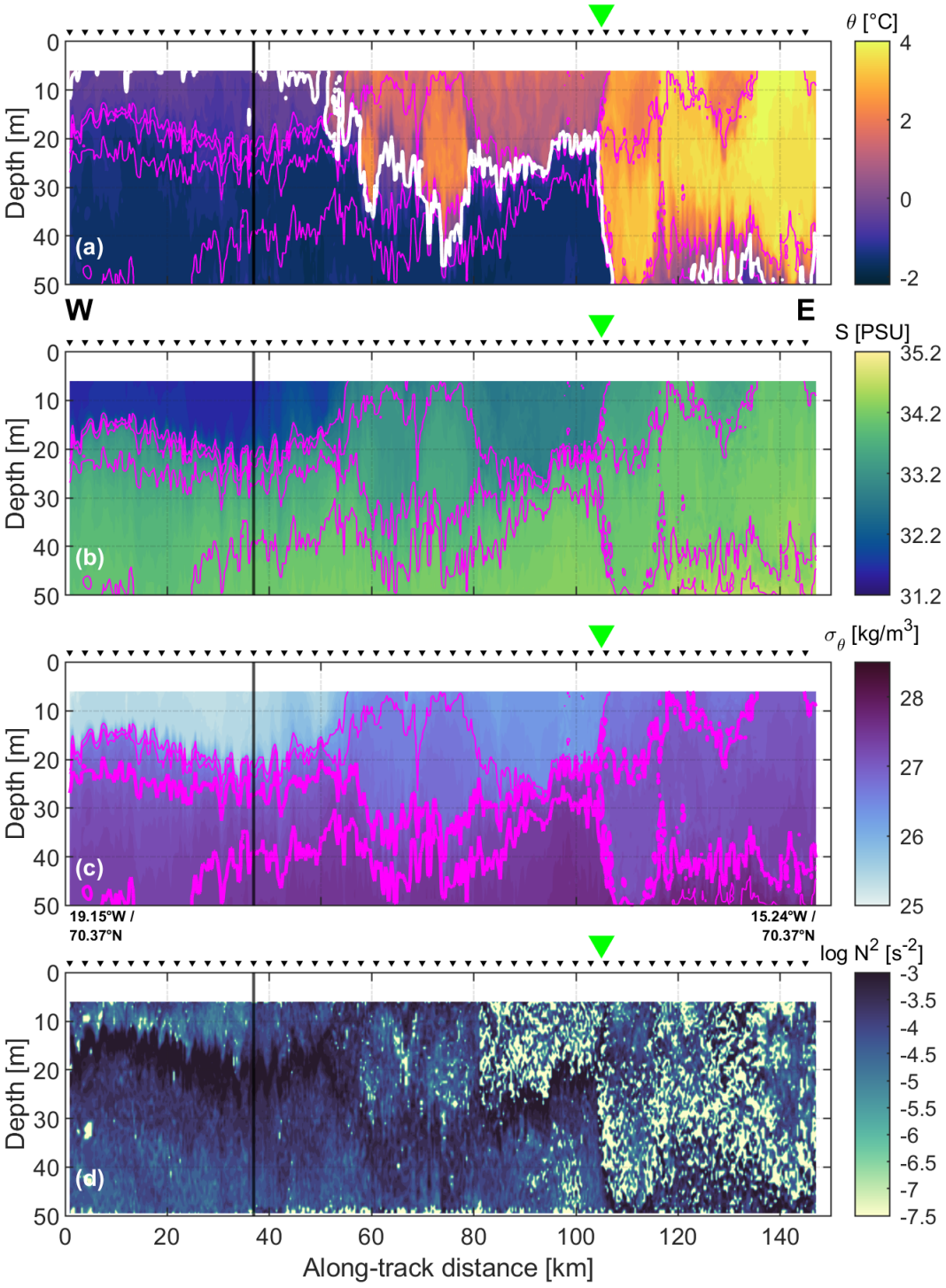

Figure 13. Same as Fig. 12 except for EGC1-3. The magenta lines in **(a)** - **(c)** indicate the 26.2-, 26.6-, 27-, 27.4-, and 27.8-isopycnals; for guidance reasons the 27 and 27.4 kg m^{-3} isolines are displayed as thick lines in **(c)**. The reference point (0 km) for the along-track distances corresponds to 70.37°N/19.17°W. The black vertical lines indicate the position where the section was interrupted for >20 hours.

Measurements from 10 m depth were extracted from EGC1-1 and EGC1-3 in order to facilitate a comparison with the constant depth section EGC1-2 and are displayed in Fig. 14. At first glance, the three occupations covered similar signatures in the physical parameters exhibiting a calmer region in the west and a more energetic one in the east. A more detailed look reveals the compensation of smaller scale features in the undulating sections, which was to be expected due to the more sparse resolution. The pronounced jump in potential density anomaly and salinity at 45 km (Fig. 14b,c), corresponding to the near-surface encounter between the freshwater plume within the PSW and the warmer water offshore, shows different characteristics depending on the section that is looked at. It was possible with EGC1-2 to resolve smaller scale fluctuations within the rather abrupt regime change. While those fluctuation were in large part already compensated in EGC1-3, the data series with the lowest spatial resolution looses information insofar as the transition between the regimes is much more gradual, close to linear. Assuming that this regime change was associated with the EGPF, the front would have lied quite offshore of the continental shelf even though the ice edge retreated behind it (cf. Fig. 8c) suggesting that the front would not have kept pace with the ice edge. It is, however, also possible that the EGPF was missed entirely. In general, the constant depth section shows that the meltwater tongue between 0 and 50 km is characterized by almost constant parameters, while variations at all observed scales are apparent in the rest of the section. More distinct jumps in all parameters are located at 100 km, and 125 km around the eastern border of the PSW layer as identified in Fig. 12 and 13.

Moreover, a peak in potential density anomaly and salinity at 15 km accompanied with a local minimum in potential temperature was recorded in EGC1-1, however, is not even indicated in EGC1-3. Whether it is a surface anomaly that dissolved within few hours or a result of a technical cause remains unclear. Although the constant depth section grants such a spatially detailed look on the hydrography, it comes with a trade-off with the information gained in the vertical: The data series suggests that the layer of PSW ($\theta < 0$°C) ends in the vicinity of 50 km (Fig. 14a). While this is true for a depth at 10 m, we know from the undulating sections that the PSW layer extends by a far amount further to the east, albeit at greater depths. It should be reminded that the last occupation of EGC1 was not continuous but because of technical problems was completed in two parts with time gap of >20 h in between (black line in Fig. 14). This unintended break, however, allows an additional evaluation of the spatiotemporal development of the observed hydrography. Changes are seen to a large part on the most eastern and more energetic side, where the less pronounced jumps are spatially shifted and compressed to the east suggesting a slight eastward extension and further alternations of the edge of the PSW layer. It also comes with a general decrease in salinity and density of the

eastern regime. In addition, a filamentous structure seems to have developed indicated by the dip in potential temperature, salinity, and potential density anomaly around 130 km. Some kind of salinity intrusion arose at the end of the melt water tongue around 45 km.

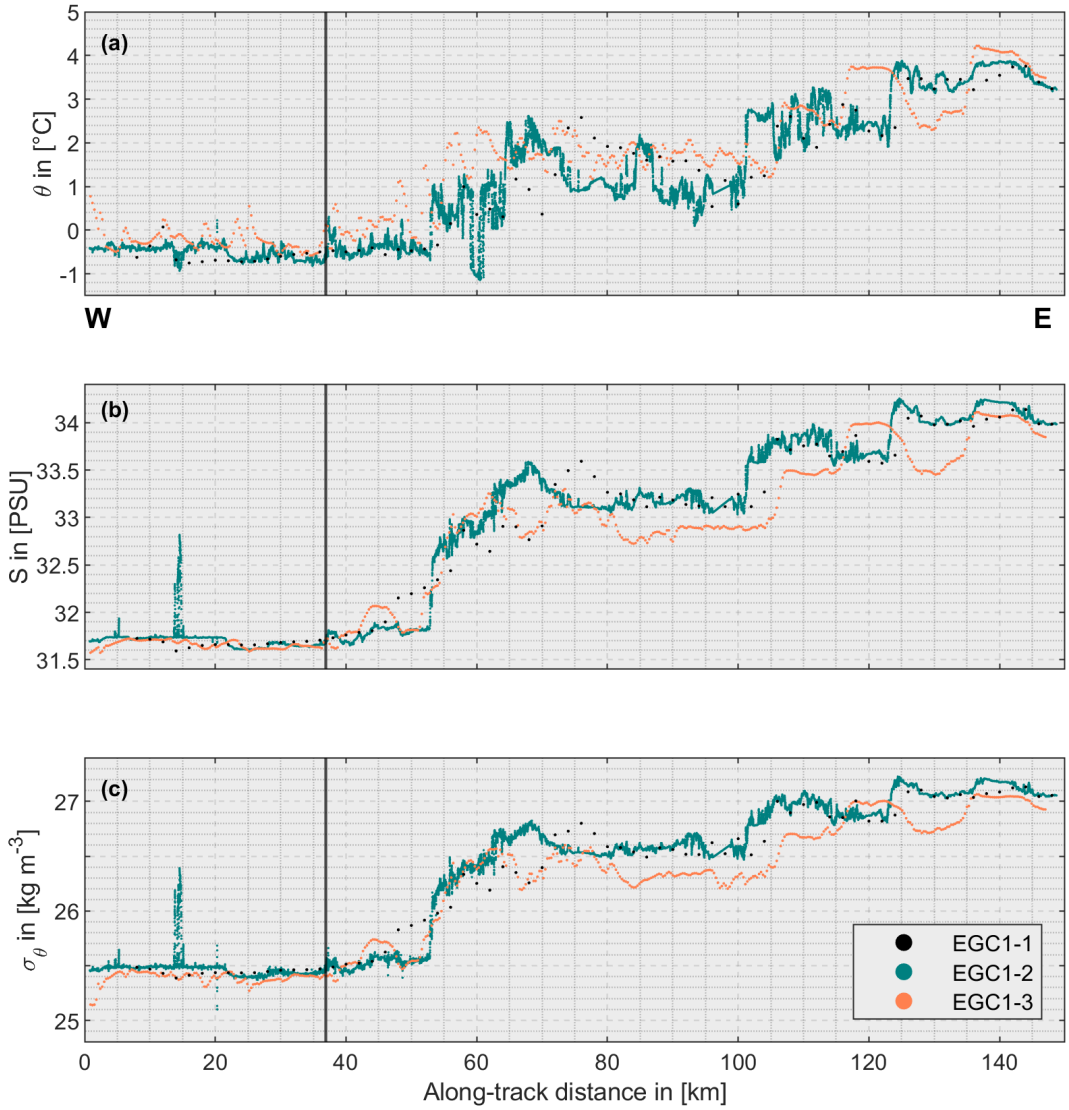

Figure 14. Continuous measurements from the topAWI CTD probe of **(a)** potential temperature (θ) [°C], **(b)** salinity (S) [PSU], and **(c)** potential density anomaly (σ_θ) [kg m^{-3}] at 10 m depth extracted from undulating tows along EGC1-1 (in black) and EGC1-3 (in coral), and from a constant depth tow along EGC1-2 (in teal). The reference point (0 km) for the along-track distances corresponds to 70.37°N/19.17°W. The black vertical lines indicate the position where EGC1-3 was interrupted for >20 hours.

EGC2

A slightly different hydrography of the EGC was recorded further north along 71°08′N (Fig. 15). The PSW layer is overlaid by warmer water from the open ocean here as well, but with no distinct edge present indicating a greater extension to the east. This difference in the extension of cold and saline surface water might be a result of the East Icelandic Current branching off the EGC (mainly PSW) between the Jan Mayen Fracture Zone and the Blossville Basin (Macrander et al., 2014). While the least saline water is found again within the upper 20 m right before the PSW subducts, the eastward increase in salinity appears to be more gradual than in EGC1 contributing to a generally light surface layer throughout most of the section with no sudden transition in regimes. Another characteristic feature in EGC2-1 involves the rise of cold and saline water toward the surface at 30 km and 75 km, which is also reflected in potential density anomaly. As seen in EGC1 stratification sporadically reaches up to the shallowest observations (Fig. 15d). Highest values in N^2 are found at 25 m depth with uplifts by about 10 m around 30 km and 75 km following the base of the freshwater plume and subsequently the upper boundary of the PSW layer. At the very surface between the uppermost measurements and 15 m depth well mixed water are sporadically distributed along the whole section.

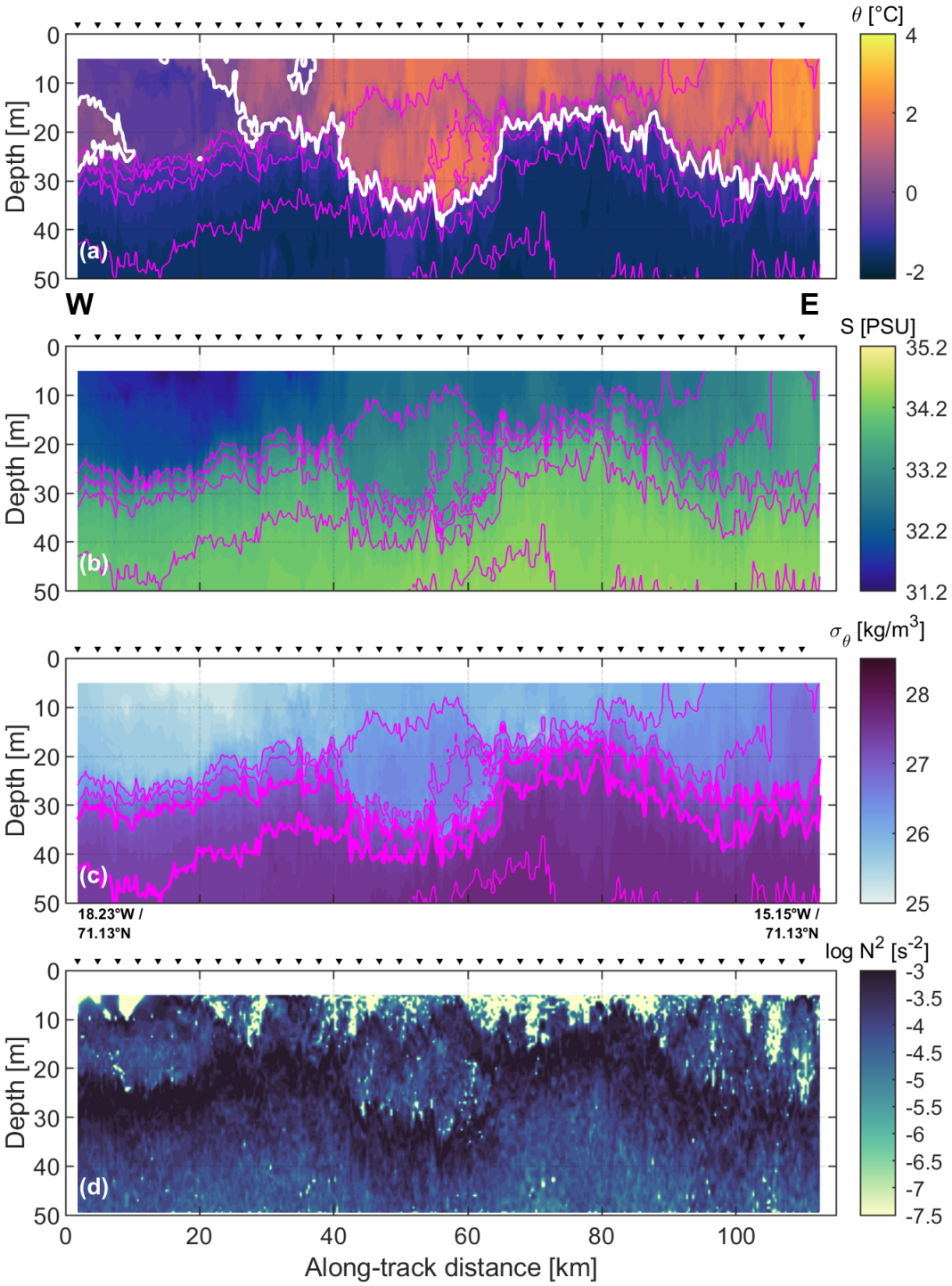

Figure 15. Same as Fig. 12 except for EGC2-2. The magenta lines in **(a)** - **(c)** indicate the 26.2-, 26.6-, 27-, 27.4-, and 27.8-isopycnals; for guidance reasons the 27 and 27.4 kg m^{-3} isolines are displayed as thick lines in **(c)**. The reference point (0 km) for the along-track distances corresponds to 71.13°N/18.29°W.

A more detailed look at 10 m and 30 m depth was gained along EGC2-1 and EGC2-3, respectively. Potential temperature (Fig. 16a) at both depths remains close to the freezing point from the most western measurements to the point where the PSW water subducts indicated by the rise of both signals from below the freezing point to around 2°C. While water at 10 m depth roughly maintains this temperature for the rest of the section, a decline to a minimum of -1.6°C was recorded in the deeper section corresponding to the rise of cold and saline water as shown in EGC2-2. At the offshore side of EGC2-3 the signal starts to oscillate between -1°C and 2°C due to the upper boundary of the PSW layer, which fluctuates around this depth. Water at 30 m depth is greater in salinity and potential density anomaly than at 10 m depth throughout the whole transect (Fig. 16b,c) with two maxima at 30 km and 75 km. Measurements obtained from EGC2-1 complement those from EGC2-3, revealing a notable inverse relationship where the local minima in the signature at 10 m roughly coincide with the highest values recorded at 30 m and vice versa at about 55 km, where values of both signals get closer to each other indicating reduced stratification. As seen before, the undulating section compensates smaller scale variations in the measured parameters (orange and black scatters in Fig. 16). Even though temporal gaps between the occupations were kept short, the hydrography slightly changed at 10 m depth. While no significant alternations are seen along the overlaying warm water, the local minima in the salinity and the potential density anomaly signal shifts slightly to the east possibly indicating a progression of the subduction or rather the retreat of the freshwater plume. Moreover, water temperature increases by 1.5°C at 30 km. Measurements of EGC2-3 match the measurements from 30 m of EGC2-2 very well.

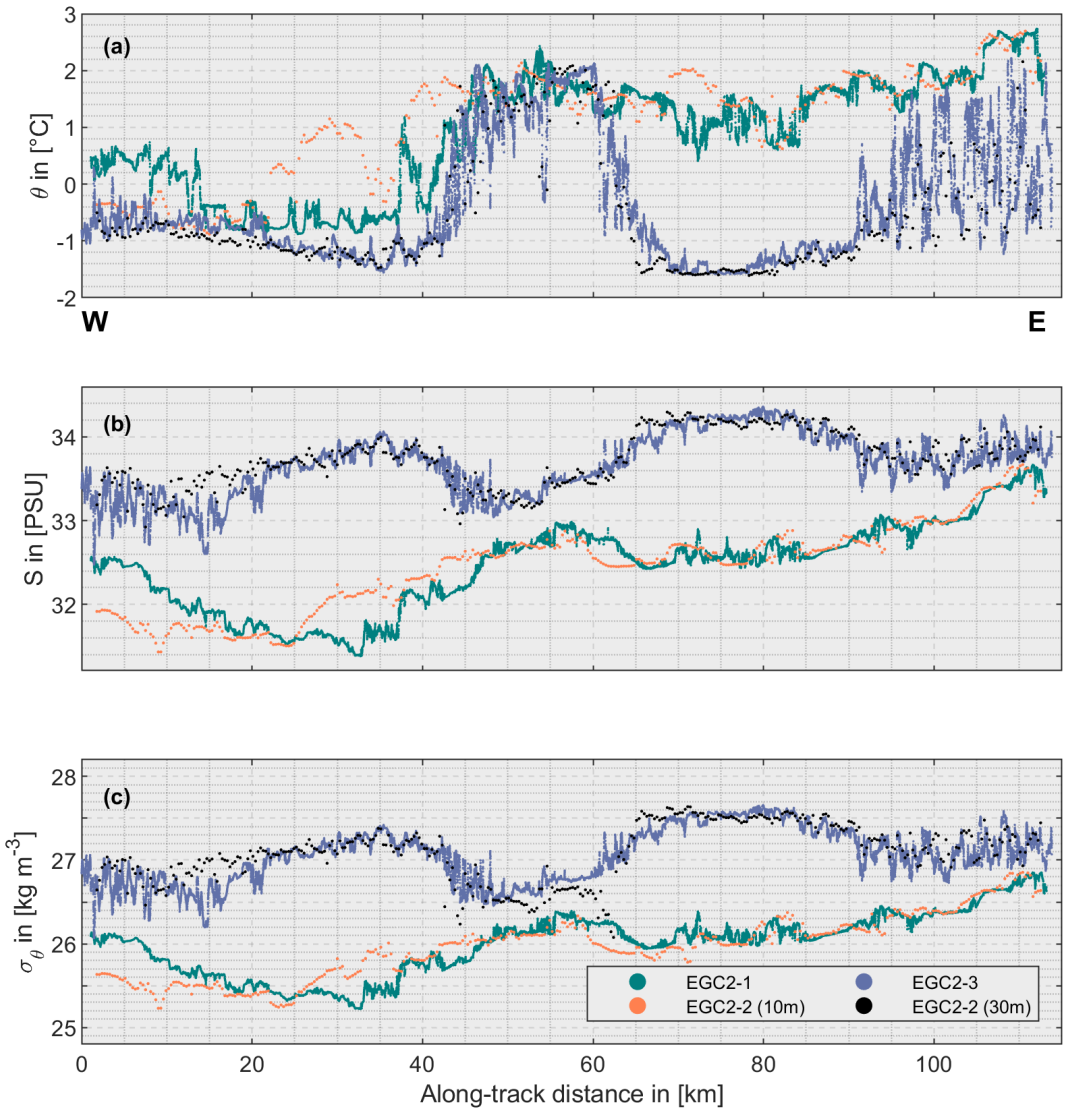

Figure 16. Continuous measurements from the topAWI CTD probe of **(a)** potential temperature in (°C), **(b)** salinity, and **(c)** potential density anomaly in (kg m^{-3}) from constant depth tows along EGC2-1 at 10m depth (in teal) and EGC2-3 at 30m depth (in indigo) and extracted from undulating tows along EGC2-2 at 10 m (in coral) and at 30 m depth (in black). The reference point (0 km) for the along-track distances corresponds to 71.13°N/18.29°W.

3.1.2 Central Fram Strait

The hydrographic section acquired in Central Fram Strait in the vicinity of the ice edge is shown in Fig. 17. In Hofmann et al. (2024) it is called "Transect 5" and its dynamical context is discussed in detail. Here we briefly summarize the pertinent hydrography. A layer of strongly stratified water holding low values in temperature and salinity expands from the uppermost measurements down to 15 m depth - a mixed layer was thus not observed, probably as a result of radiatively driven melt of sea ice. A tongue of more mixed water with $\theta < 0\,°C$ and $\sigma_\theta < 27.7\,kg\,m^{-3}$, fitting the definition of PW after Rudels et al. (2005), extends from the eastern end of the section to about 10 km. The PW layer has a vertical thickness of 55 m in the east and thins down to the west. We found smaller-scale frontal structures at the surface around 13 and 27 km causing localized deepening of the PW layer.

Warmer and more saline AW ($\theta > 2\,°C$ and $\sigma_\theta > 27.7\,kg\,m^{-3}$) resides right beneath the PW between 23 and 32 km and a pronounced filament of AW with a temperature up to 4.5°C and salinity up to 35 occupies even shallower depths to about 50 m depth between 4 and 21 km. The filament consists of two limbs with a width of around 6-7 km as indicated by a separating thin band of warmer and fresher water around 11.5 km. Another intrusion of warm and saline water is found at 7.5 km below the stratified surface layer and a lens of well-mixed water west of 5 km between 40 and 75 m depth restricts the filaments to the west. The subsurface front between AW and PW comes with downward sloping isopycnals between 50-100 m depth indicating a subduction of the AW below the PW.

PW is found on the portion of the section that was more distant from the ice edge, while AW occupies the side nearer to the sea ice, contrasting to the large-scale gradient, that is warmer and more saline water in the eastern side of Fram Strait and colder and fresher water in the western side. Using a combination of a variety of hydrographic data Hofmann et al. (2024) sketched the (sub-)mesoscale variability in the vicinity of the MIZ suggesting that this counter-intuitive distribution of water masses was part of an anticyclonic eddy with a diameter of ∼30-50 km where AW protruded to the northeast and PW to the southwest. The presence of the ice edge to west is indicated by PW within the upper 50 m of the water column west of the AW filament.

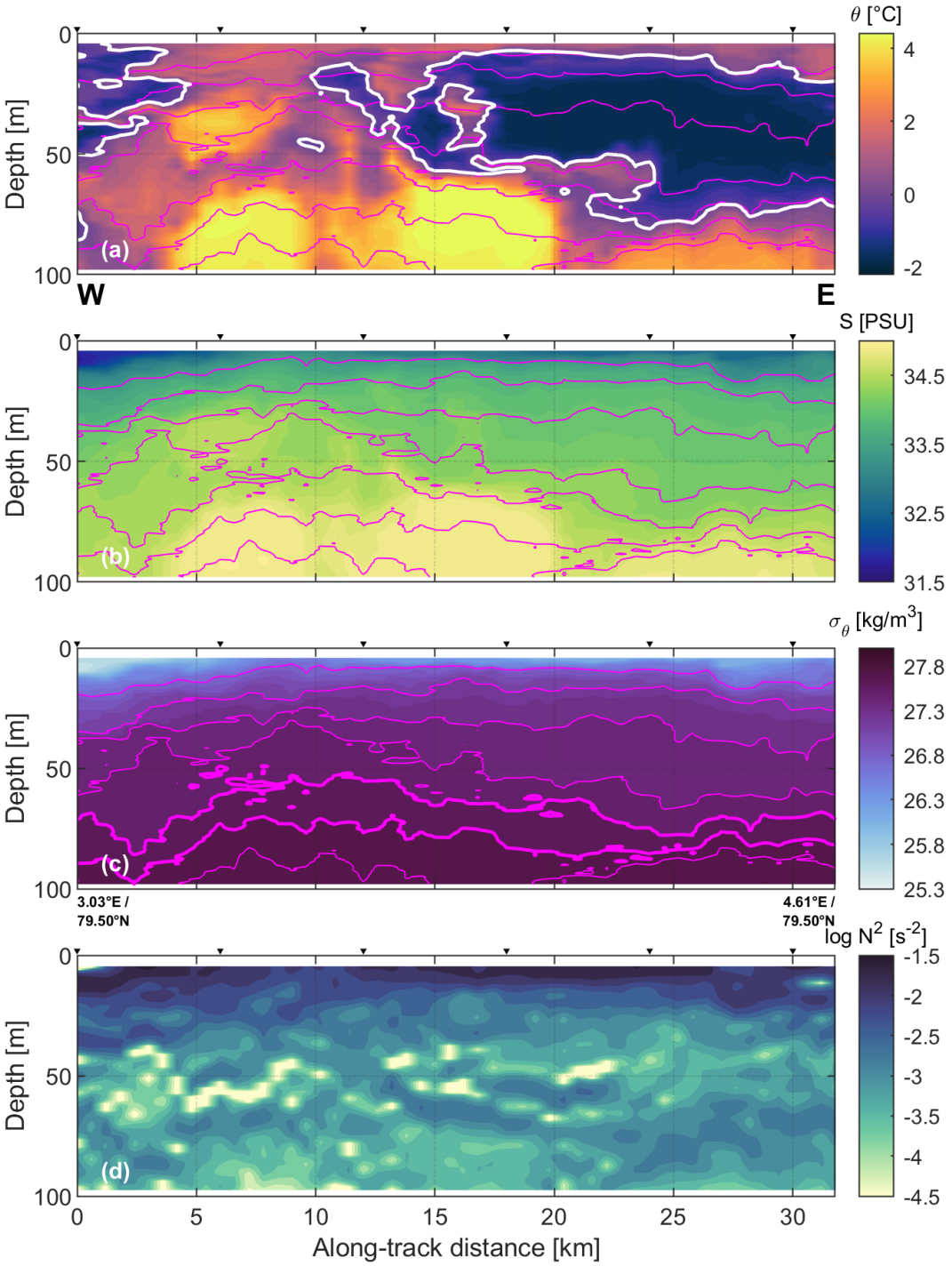

Figure 17. Same as Fig. 12 except for FST1-1. The magenta lines in **(a)** - **(c)** indicate the 26.8-, 27.2-, 27.4-, 27.5-, 27.6-, 27.7-, and 27.75-isopycnals; for guidance reasons the 27.6 and 27.7 kg m^{-3} isolines are displayed as thick lines in **(c)**. The red line in **(a)** represent the 2°C-isotherm. The reference point (0 km) for the along-track distances corresponds to 79.50°N/3.03°E. Note the different colorscale of θ, S, σ_θ, and $\log(N^2)$ compared to Fig. 12.

3.1.3 Northern Fram Strait / MIZ

The hydrographic section acquired from novel under ice measurements in northern Fram Strait is displayed in Fig. 18. The open water made up the first 15 km of the section and held water with temperatures between 2.5°C and 5.6°C with the warmest water occupying the surface (Fig. 18a). Lower salinity values ($\sim$ 34.2PSU) are found here, indicating sea-ice related effects on this part of the open sea. Using TS-diagrams von Appen et al. (pers. comm. 2024) suggested that this freshwater input in the ice-affected open water was caused by AW melting the sea-ice. The saline core of the WSC as indicated by an intermediate maximum of around 35 was located at 100 m depth (Fig. 18b). The mixed layer depth, as computed from a density difference of 0.05 kg m^{-3} with respect to the uppermost values, varied between 11.5 and 22 m in the open water and salinity differs by less than 1 PSU between 11 and 100 m, thus the area southeast of 15 km fits the definition of von Appen et al. (2021) for a mixed layer regime.

The MIZ makes up the the remaining part of the section and is characterized by a layer of PW with a thickness of <100 m. It extends from the end of the section to 30 km with a coinciding progression between the 0°C-isotherm and 27.7 kg m^{-3}-isopycnal (Fig. 18c) marking the lower boundary of the PW. The transition from the open ocean to the outer MIZ is characterized by a significant drop of the near-surface temperature from >2°C at 15 km to -1°C at 38 km. In this area AW remains dominant for most of the water column and is restricted to the northwest by an almost vertical 2°C-isotherm. Meltwater, as indicated by salinity values below 32 and probably originating from radiatively driven sea ice melt (von Appen et al., in prep.), occupies the uppermost measurements of the outer MIZ and near freezing temperatures, marking the core of the PW, are found around 40 m depth between 32 and 80 km. A density difference of > 1kg m^{-3} over a vertical distance < 40 m is crossed between the meltwater and the core of the PW causing a strong stratification above 40 m depth as indicated in Fig. 18d. Between 70 and 80 km AW is again found up to 75 m depth and near-surface temperature exhibits distinct spatial variability, setting the boundary between the outer and inner MIZ.

Within the inner MIZ a thinning of the PW layer to the northwest can be observed, which gets as thin as <50 m, and water holding temperature between 0 and 2°C occupies a large amount of the water column fitting the AAW definition after Rudels et al. (2005) - Atlantic Water that has transited through the Arctic Ocean and was transformed through mixing. The inflow of AW to the Arctic Ocean appears not to be of importance for the water column covered by the inner MIZ. The surface exhibits much less variability in temperature as observed in the outer MIZ, which might be a result of the only solar irradiation that penetrates the water column.

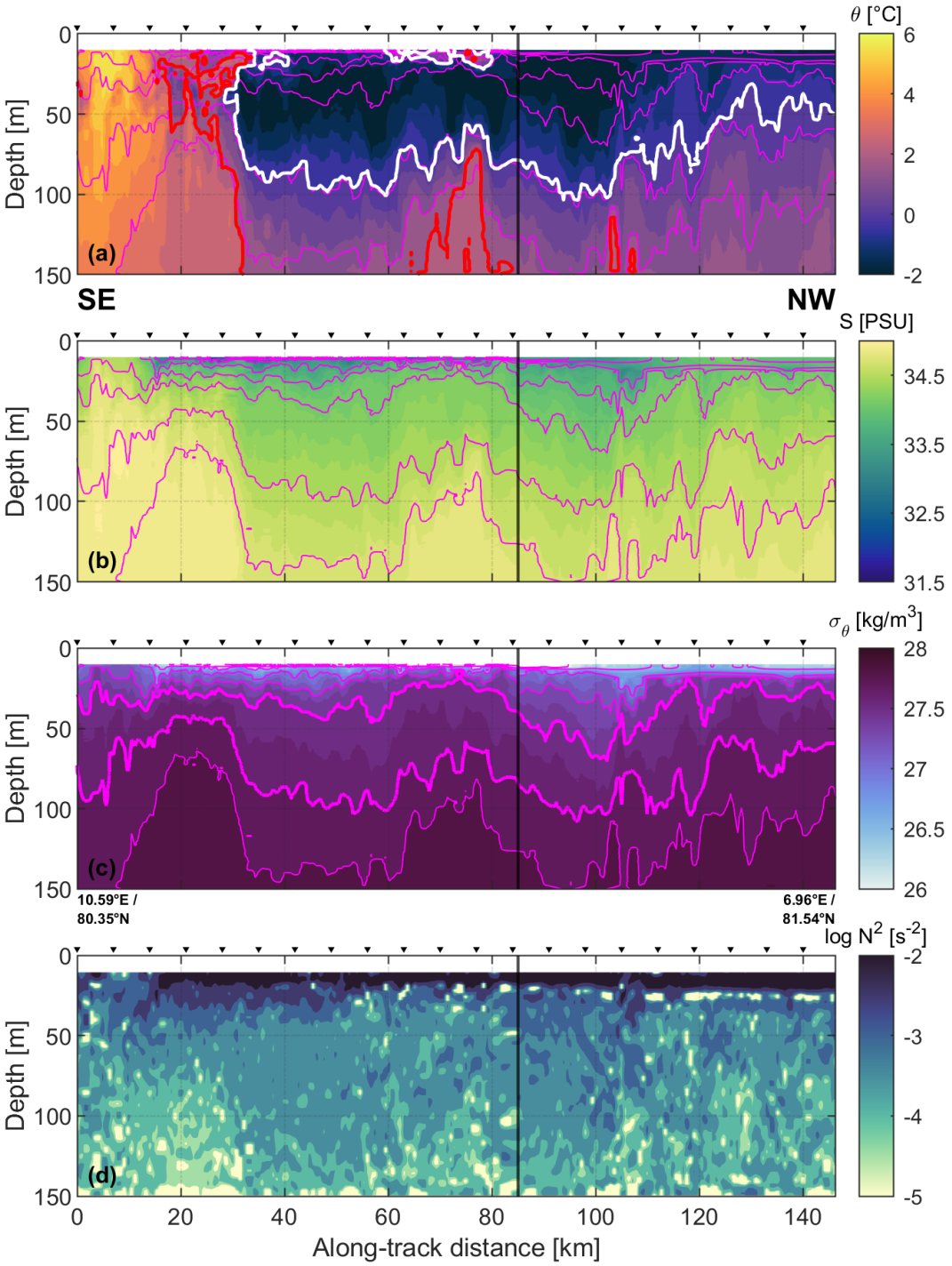

Figure 18. Same as Fig. 12 except for MIZ1-1. The magenta lines in **(a)** - **(c)** indicate the 25.5-, 26-, 26.5-, 27.3, 27.5, 27.7, and 27.8-isopycnals; for guidance reasons the 27.5- and 27.7 kg m^{-3} isolines are displayed as thick lines in **(c)**. The red line in **(a)** represent the 2°C-isotherm and the cyan line in **(a)** - **(d)** represents the depth of the mixed layer, as determined by the criterion of a 0.05 kg m^{-3} density difference relative to the surface. The reference point (0 km) for the along-track distances corresponds to 80.35°N/10.59°E. The black vertical lines indicate the position where the section was interrupted for >2.5 days. Note the different colorscale of θ, S, σ_θ, and log(N^2) compared to Fig. 12.

3.1.4 Equatorial Atlantic

The hydrography along the equatorial crossing is shown in Fig. 19 and revealed potential temperatures between 11°C at 300 m depth and 28°C close to the surface (Fig. 19a). There, slightly colder water was found south of the equator between an along-track distance of 150 and 200 km with an increasing gradient to the north. The position of the thermocline (roughly estimated with the 20°C-isotherm) varied between 65 m and 80 m depth. The least saline water appeared at the bottom of the section (Fig. 19b) and an intermediate maximum of around 36.5 extends throughout the whole crossing at 65 m depth. This high-salinity layer got as thick as 40 m at a distance of 325 km and from there thins down north- and southward, indicating the location of the EUC, whose core is associated with a local maximum in salinity (Blanke et al., 2002). Based upon the corresponding velocity profiles (not used in this study) Mathieu (2019) showed that the EUC actually acted as a net eastward transport of salinity. Above, the water generally contains lower values in salinity with a surface maximum again between 150 and 200 km accompanied by outcropping isopycnals. This area might correspond to the upwelling region in the eastern Atlantic extending from the coast of Guinea all along the equator. A decreasing gradient in salinity toward the ends of the section was found exhibiting slightly fresher water at the northern side - probably caused by the location of the Intertropical Convergence Zone (ITCZ). It is known to shift northward during northern summer and to be a region with a high precipitation potential, which could also explain the shallowing of the MLD (cyan line) from 42 m at 0 km to 5.5 m at 456.4 km as the surface freshening can lead to a stronger stratification and impedes mixing. This is highlighted by a thick layer of stratified water ($N^2 < 10^{-3}\,\mathrm{s}^{-2}$) the upper boundary of which progresses to smaller depths in the north (Fig. 19d). The gridded section of potential density anomaly is shown in Fig. 19c exhibiting a wider span of density values than all the other regions with the heaviest water of $\sigma = 26.75\,\mathrm{kg\,m}^{-3}$ at 300 m depth and the lightest water of $\sigma = 22.55\,\mathrm{kg\,m}^{-3}$ within the mixed layer for the northernmost measurements. The isopycnals within the EUC exhibits a high degree of vertical compression, indicating a strong density gradient and stratification. A similar, but less pronounced compression of isopycnals was located at 300 m possibly indicating the permanent pycnocline. The area in-between was relatively well-mixed with an especially weak stratification around 200 km between 200 m and 250 m depth. In addition, we found outcropping isopycnals as a result of the thermohaline gradients at the surface.

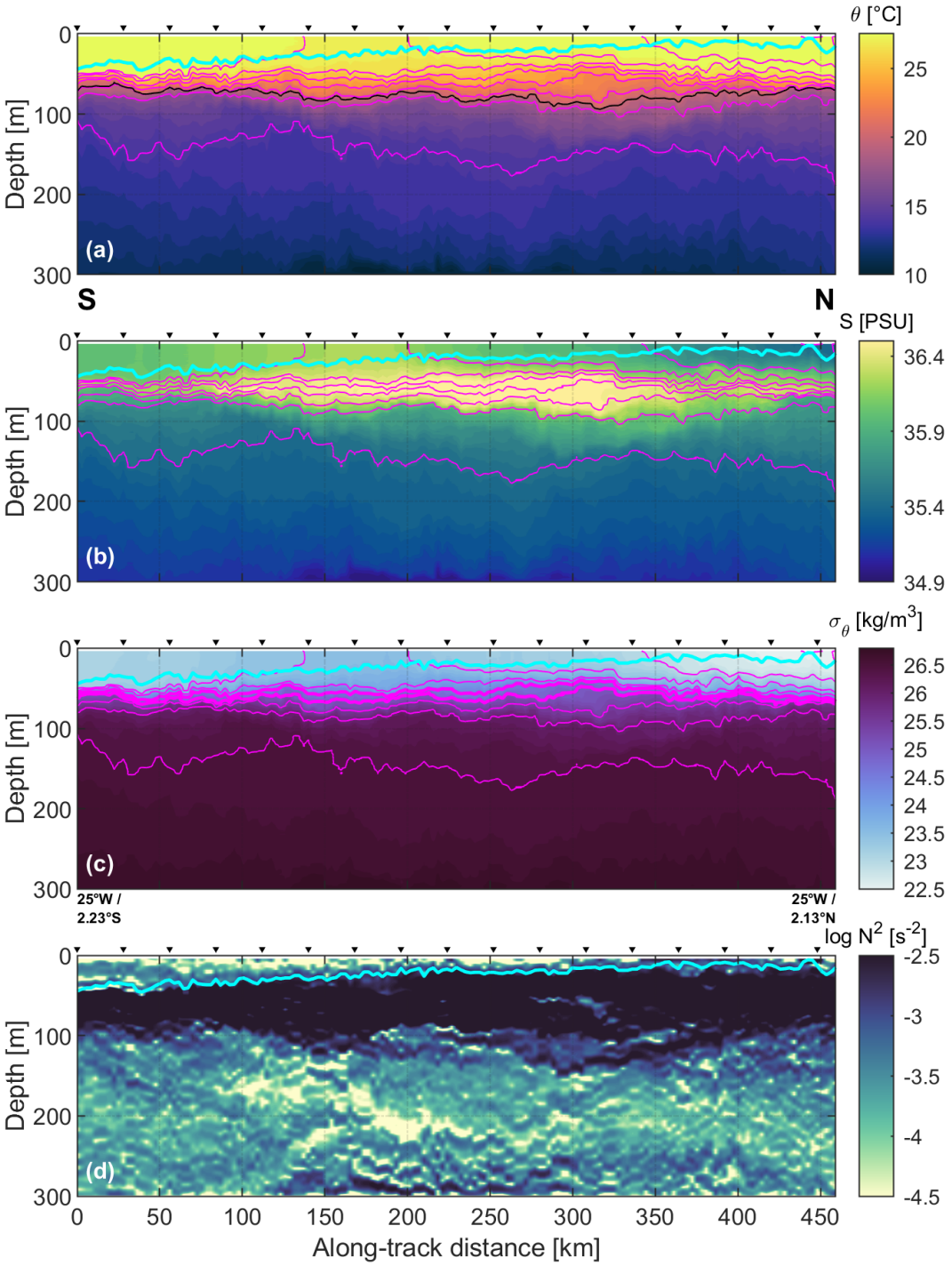

Figure 19. Same as Fig. 12 except for EQT1-1. The magenta lines in **(a)** - **(c)** indicate the isopycnals in a 0.5-spacing; for guidance reasons the 24.5 and 25 kg m^{-3} isolines are displayed as thick lines in **(c)**. The black line in **(a)** represents the 20°C-isotherm and the cyan line in **(a)** - **(d)** represents the depth of the mixed layer, as determined by the criterion of a 0.05 kg m^{-3} density difference relative to the surface. The reference point (0 km) for the along-track distances corresponds to 2.23°S/25°W and the equator is crossed at an along-track distance of 460 km. Note the different colorscale of θ, S, σ_θ, and $\log(N^2)$ compared to Fig. 12.

3.1.5 Cape Verde Frontal Zone

The topAWI section obtained offshore of the northwest African coast is shown in Fig. 20. The following will cover the key features of the hydrography as described in a previous study by von Appen et al. (2020) which we refer to for a more detailed assessment of the data. They used remote sensing information, such as sea surface temperature (SST) and sea level anomaly (SLA) data, to reveal a westward advection of cold upwelled water from the coast to outside of the upwelling region and the presence of an anticyclonic mode water eddy (ACME) centered around 21.5°N/20.5°W. These mesoscale structures were also captured by the towed system. Slightly colder and fresher water at the surface is found between 120 and 135 km (Fig. 20a,b) corresponding to the filament of upwelled water from the upwelling region to the east. The southwestern edge of the eddy is indicated by downward and upward sloping isopycnals (Fig. 20c) between 150 and 170 km below and above $\approx$ 150 m depth, respectively. The MLD (cyan line) get as shallow as 20 m around 50 km and as deep as 70 m at 150 and 230 km corresponding to the edges of the anticyclone, whereby the northeastern edge is also indicated by thermohaline gradients within the mixed layer. Intrusions of more saline water ($\sim$36.8 PSU) frequently occur below the mixed layer, such as at 60, 80, and 270 km. Moreover, the mixed layer within the mesoscale eddy exhibits higher values in the potential density anomaly causing a horizontally decreasing gradient to the south as shown by outcropping isopycnals to the surface. Highest values of N^2 (Fig. 20d), indicating a strong stratification, are found along the base of the mixed layer. An intermediate minimum in N^2 is located in the interior of the eddy between 150 and 250 m depth indicating a homogeneous layer of mode water with a lens-like structure (upward doming isopycnals above and downward doming one below) trapped in the core of the anticyclone. Compared to the ambient water within the same depth range, salinity is slightly higher in the mode water. Steep isolines in temperature and salinity around 60 km separates cold and fresh water from warmer and more saline water. Performing an isopycnal decomposition von Appen et al. (2020) showed that these thermohaline gradients corresponded to a front between generally fresher South Atlantic Central Water (SACW) and saltier and warmer North Atlantic Central Water (NACW) as expected from the Cape Verde Frontal Zone, where these water masses are confluent (see Tomczak Jr, 1981). The front, however, has no dynamic signature as indicated by the rather flat isopycnals. On the other side of the section a saline and cold band with a width less than 20 km north of 240 km was classified as SACW. The decomposition also revealed that the southwestern half of the mixed layer is composed of SACW with a decreasing concentration to the northwest and that the ACME consisted of almost pure NACW with the highest concentration located within the mode water.

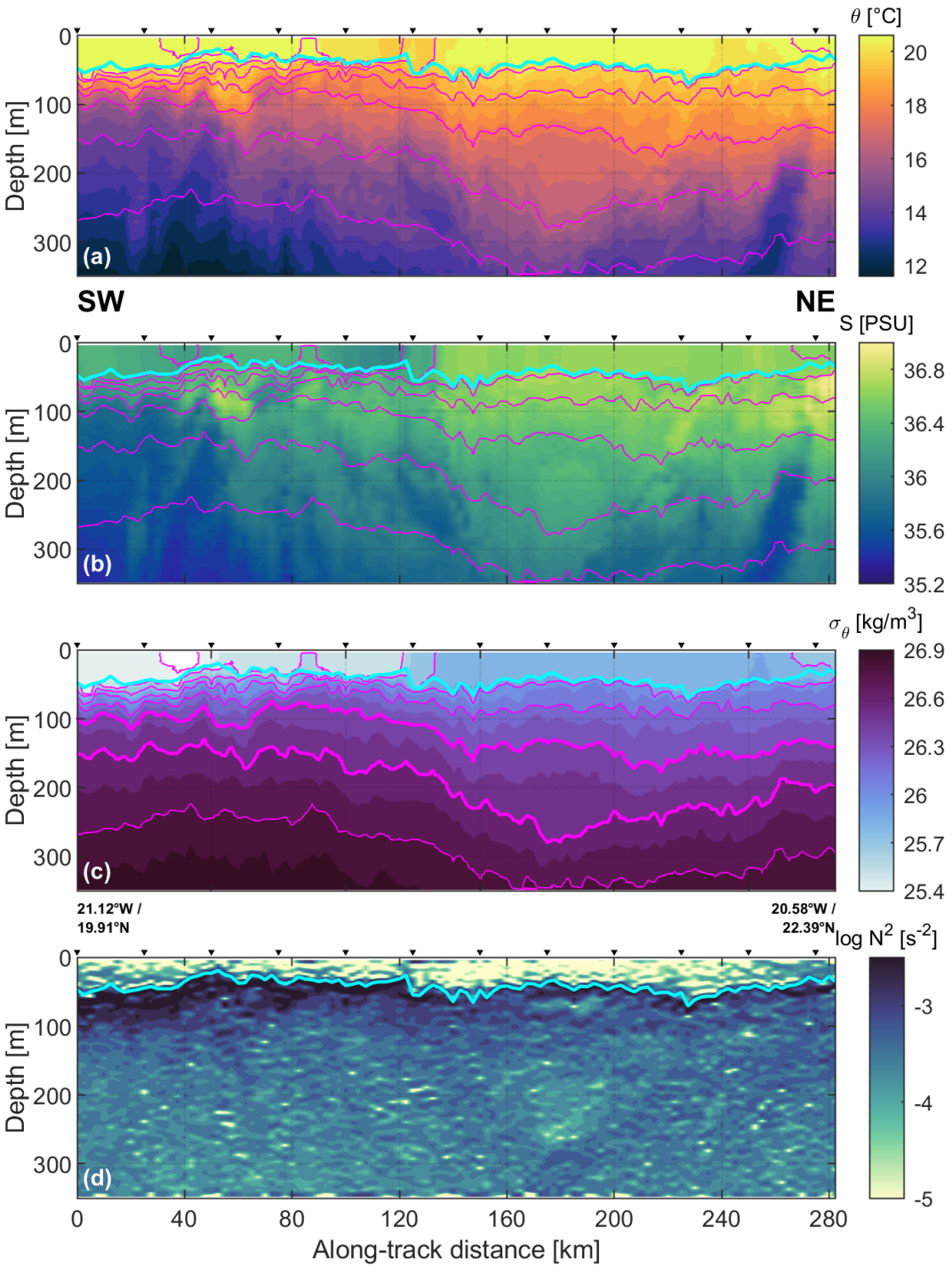

Figure 20. Same as Fig. 12 except for CVF1-1. The magenta lines in **(a)** - **(c)** indicate the 25.4-, 25.6-, 25.8-, 26-, 26.2-, 26.4-, 26.6-, and 26.8-isopycnals; for guidance reasons the 26.4- and 26.6 kg m^{-3} isolines are displayed as thick lines in **(c)**. The cyan line in **(a)** - **(d)** represents the depth of the mixed layer, as determined by the criterion of a 0.05 kg m^{-3} density difference relative to the surface. The reference point (0 km) for the along-track distances corresponds to 19.91°N/21.12°W. Note the different colorscale of θ, S, σ_θ, and $\log(N^2)$ compared to Fig. 12.

3.1.6 Antarctic Circumpolar Current

The longest hydrographic section, conducted along 25°W in the Southern Ocean, is shown in Fig. 21 and displays the traditional view of the ACC as a multi front structure. At the southern end of the section, the water column exhibited rather vertically homogeneous properties marking the limit of the circumpolar flow, namely the Southern Boundary (SB). It represents the poleward edge of the divergence zone, which here showed up as saline and warm upwelled NADW south of 400 km causing a local uplift of the MLD. The divergence came with a band of sharp thermohaline gradients with large poleward isopycnal tilts. Due to the geostrophic balance of the mass field such steep tilts are exhibited by eastward flows on the southern hemisphere and can be used for the localization of jet-like currents (Park et al., 2019). The SB is typically not associated with such a jet.

A second band of sharp gradients was found around 300 km, which might be attributed to the SACCF corresponding to the northernmost extent of the deep water. Another one could be located south of 100 km, which we identify as the Polar Front. The steep rise of isopycnals coincides with the location of the northernmost extent of winter water (2°C-isotherm at 200 m depth), and therefore fitting the definition of the PF after Botnikov (1963). It separates the Antarctic Zone from the Polar Frontal Zone. Most of the occupied section laid within the former one characterized by AASW with highly variable surface values (Fig. 21b): more saline to the south as it mixed with NADW and less saline to the north probably due to higher precipitation rates. The regime enclosed by the SACCF and the PF displayed a disruption of the winter water between 300 and 225 km by warmer and fresh water masses with similar properties as water between 120 and 80 km. This might be a result of crossing the edge of a mesoscale structure, resembling a cyclonic eddy (R. Mole, pers. comm. 2024). This assumption is emphasized by an upward doming of isopycnals between 220 and 100 km indicating upwelling, that is vertical motion that might have been induced via eddy pumping. This could also explain why a distinct cold core of the winter water, such as in the southern half of the section (Fig. 21a), was not found here.

The Polar Frontal Zone, roughly the first fifth of the section, was occupied by the warmer and more saline Subantarctic water and exhibited a northward deepening of the MLD from 100 m to around 180 m depth. This indicates the subduction of AASW heading north of the PF forming AAIW. As the cold and fresh layer deepened, the stratification below the mixed layer weakened (Fig. 21d) facilitating deep mixing, which here is indicated by a distinct deepening of the MLD. Thus, the main process of the ACC - the upwelling of deep water, which is modified at the surface as it moves north across the fronts and the subsequent subduction as AAIW (Tomczak & Godfrey, 2003) - was fully captured, horizontally that is.

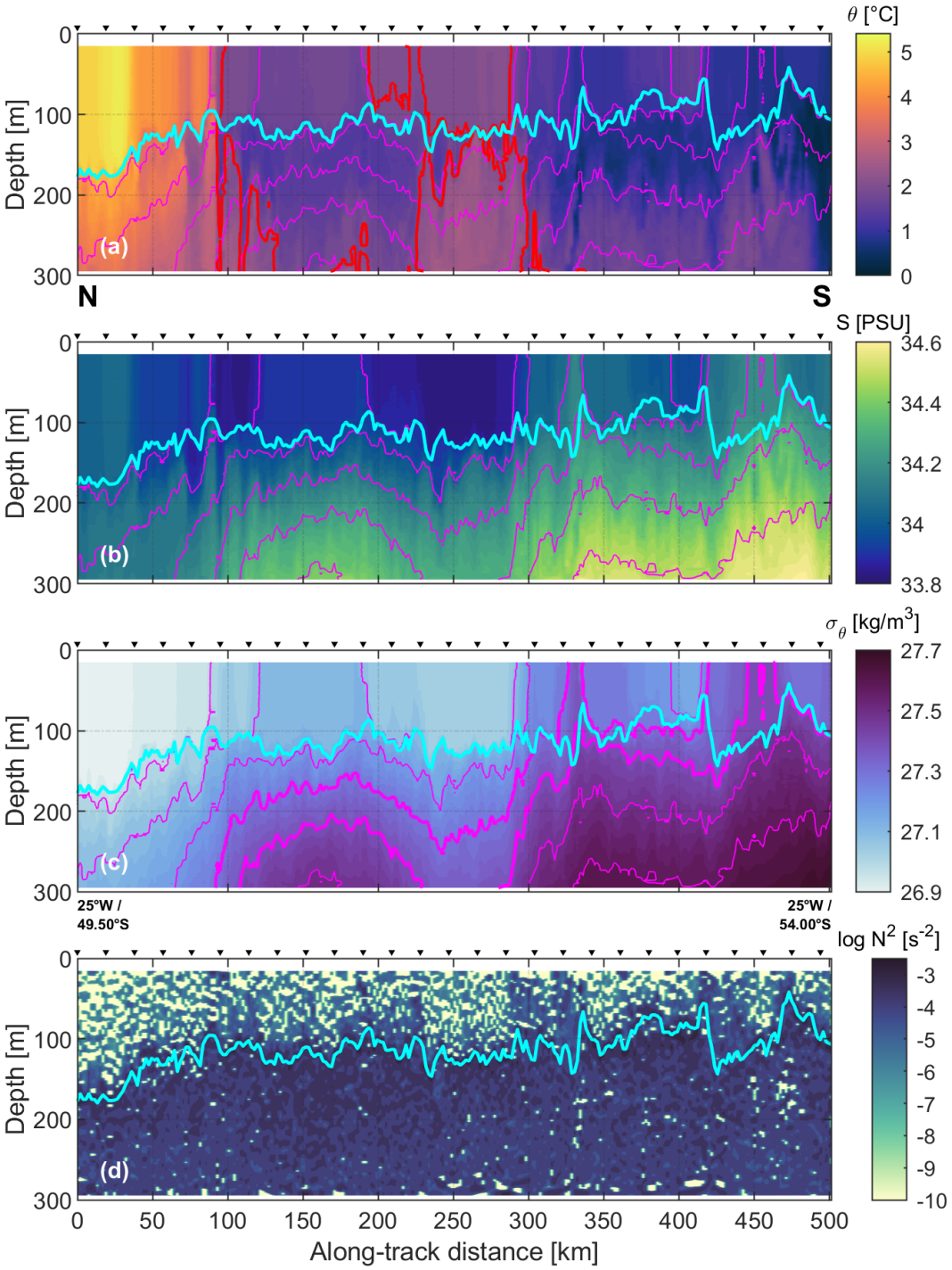

Figure 21. Same as Fig. 12 except for ACC1-1. The magenta lines in **(a)** - **(c)** indicate the isopycnals in a 0.1-spacing; for guidance reasons the 27.3- and 27.4 kg m^{-3} isolines are displayed as thick lines in **(c)**. The cyan line in **(a)** - **(d)** represents the depth of the mixed layer, as determined by the criterion of a 0.05 kg m^{-3} density difference relative to the surface. The red line in **(a)** indicates the 2°C-isotherm. The reference point (0 km) for the along-track distances corresponds to 49.50°S/25°W and the ACC is crossed at an along-track distance of around 500 km. Note the different colorscale of θ, S, σ_θ, and $\log(N^2)$ compared to Fig. 12.

3.2 Subsurface gradients and their scale sensitivity

3.2.1 An idealized case

Vertical sections obtained in the northern polar region revealed a strong lateral anisotropy in the density signatures as a result of covering multiple distinct oceanic regimes. As an attempt to assess the multi-scale behaviour of density gradients across such regime changes, which mostly corresponded to a sudden jump in the signature, the resampling routine as described in 2.8 and 2.9 was executed on an idealization - a single step function $H(x - x_0)$: $H(x < x_0) = 25.5$ & $H(x \geq x_0) = 25.5 + 0.5 \cdot h$ with varying factors h of 1, 2, and 3 (Fig. 22a-c). These are referred to as H-1, H-2, and H-3 in the following. Even though these data series are artificially created and thus technically unitless, they are treated as density signals over the distance of 100 km with a resolution of 2.5 m ensuring that they fit into the analysis, while maintaining consistency when compared to the in situ measurements later on. Out of convenience, the point of discontinuity was set to $x_0 = 50$ km.

One particular feature the joint distributions all had a common is a distinct thin layer of data pairs (Fig. 22A-C), which was to be expected when computing the quotient between the same difference in density, that is the height of the step, and various sampling distances. These layers follow a negative non-linear progression. Moreover, a base of smaller gradients ($< 0.005\,\mathrm{kg\,m^{-3}\,km^{-1}}$) made up a noticeable amount (> 10%) of computed gradients for all observed length scales. This was most likely a result from the application of a low-pass filter right before downsampling the data, where gradients near the discontinuity become close to zero, but not zero values. The distributions exhibited a sporadic pattern between the base and the characteristic line, which transitioned into a pocket-like pattern for lenghtscales $\lambda > 2.6$ km. When the binning intervals were adjusted from 200 m to the resolution of the density signal, this pattern is reduced (not shown) suggesting a technical combination of low pass filtering and binning as a cause for gradients differing from the characteristic line. While an increase of the signal jump resulted trivially in a larger strength of gradients as indicated by increasing values in a for the outer envelope ($a_{\text{H-1}} = 0.57 \pm 0.01\,\mathrm{kg\,m^{-3}\,km^{-1}}$, $a_{\text{H-2}} \approx 2 \cdot a_{\text{H-1}}$, $a_{\text{H-3}} \approx 3 \cdot a_{\text{H-1}}$), the scaling parameter m remained almost unaffected ($k_{\text{H-1}} = 0.971 \pm 0.008$, $k_{\text{H-2}} = 0.973 \pm 0.007$, $k_{\text{H-3}} = 0.980 \pm 0.007$). It should be noted that the parametrization did not work well for the lower envelopes due to the inner sporadicity of the joint distributions, and therefore are not considered for the idealized density signals.

In a forth example H-4, the same method was applied on a dual step function (Fig. 22d), with one step at $x_0 = 25$ km with the same height as H-1 and another one at 50 km with the same height as H-3. The corresponding bivariate histogram (Fig. 22D) features a bimodal behaviour resembling the characteristic lines as seen

in aforesaid signals and slightly greater gradients at $\lambda > 25\,\mathrm{km}$ (not shown) as at these scales a density difference of $\Delta\sigma_\theta = 2\,\mathrm{kg\,m^{-3}}$ gets resampled. The outermost envelope appeared to be determined by the largest density difference that gets subsampled by most scales, which resulted in almost identical parameters $k = 0.980 \pm 0.007$ and $a = 1.67 \pm 0.03\,\mathrm{kg\,m^{-3}\,km^{-1}}$ as estimated for H-3. It is to be expected that less dominant signals like the step 25 km have an impact on the inner pattern of the joint distribution, however, large uncertainties in the parametrization of lower envelopes ($k_{\text{H-3,80\%}} = 0.89 \pm 0.16$, $a_{\text{H-3,80\%}} = 1.73 \pm 0.75\,\mathrm{kg\,m^{-3}\,km^{-1}}$, $k_{\text{H-4,80\%}} = 0.84 \pm 0.15$, $a_{\text{H-4,80\%}} = 1.18 \pm 0.49\,\mathrm{kg\,m^{-3}\,km^{-1}}$) would suggest that the inner distributions do not differ between H-3 and the dual step function.

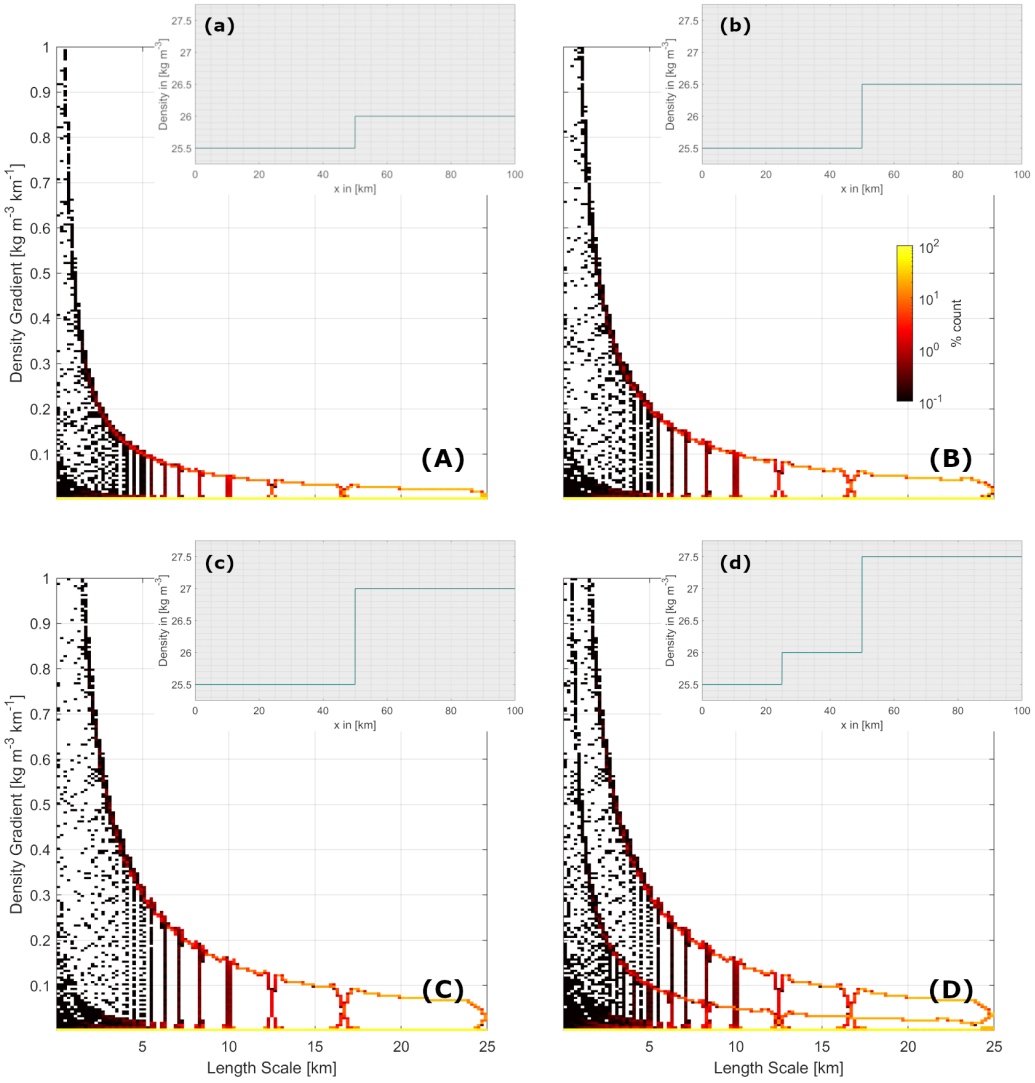

Figure 22. Simplified density signals as single step function with jumps of **(a)** 0.5, **(b)** 1.0, **(c)** 1.5 $\mathrm{kg\,m^{-3}}$ and **(d)** as a dual step function and their corresponding distribution of lateral density gradients ($\mathrm{kg\,m^{-3}\,km^{-1}}$) **(A)-(D)**. The relative occurrence (%) of gradients at various horizontal length scale (0.1 to 25 km) bins is displayed by the logarithmic color scale.

3.2.2 EGC: Functionality of the subsampling routine

A descriptive approach

Fig. 23 presents the joint distribution in density gradients along EGC1 as subsampled by various length scales from occupations with mean sampling intervals of 2.3, 300, and 1900 m. As addressed in 3.1.1, the different resolutions resulted in a significant loss on information in the density signal from EGC1-2 via EGC1-3 through to EGC1-1, which here translates into the the bivariate histograms. Measurements obtained from EGC1-2 allowed the most detailed multi-scale analysis (Fig. 23b) of the density gradient distribution, displaying a non-linear relation between horizontal density gradients and sampling length scales: as the length scale is progressively increased, a distinct decrease in gradients becomes evident. The joint distribution resembled a boomerang-shaped form, a comparable pattern was obtained by a Sailbuoy survey in the Antarctic MIZ (Swart et al., 2020), where the most notable decline coincided with the region between the internal R_i and the full-depth Rossby radius R_d of deformation. The validity of this observation, however, could not be confirmed for our density gradients as the calculation of the internal Rossby radius depends on the depth of the mixed layer, which was not present within the EGC regime covering most of the section. Further differences are a distinct multi-modal pattern extending over all spatial scales and resembling the findings of subsampling a step function, which will be addressed later on, and density fronts of much higher magnitude. The largest gradients ($> 300\,\mathrm{kg\,m^{-3}\,km^{-1}}$) were found at the smallest spatial scale of 2.3 m and arose from sometimes questionable assignments of coordinates leading to cast-to-cast distances of zero or close-zero values. Gradients of these magnitudes, however, had an infrequent occurrence over length scales of $\mathcal{O}(\text{meters})$ only and represented just a small percentage $\sim 0.001\%$ at these sampling scales. These gradients were not considered in any analysis or interpretation. The majority (18-100% depending on the lengthscale that is looked at) was sampled at $< 0.03\,\mathrm{kg\,m^{-3}\,km^{-1}}$ contributing to an almost constant conditional mean gradient (mean value for each length scale bin) varying around $0.015\,\mathrm{kg\,m^{-3}\,km^{-1}}$, that is the mean gradient for each length scale bin, from the largest sampling length scale down to $R_\mathrm{d} = 9\,\mathrm{km}$ (Chelton et al., 1998). The marginal mean (mean value over all density gradients) and its standard deviation was $0.240 \pm 0.001\,\mathrm{kg\,m^{-3}\,km^{-1}}$ and is generally determined by the gradients as sampled at higher sampling frequencies due to the resampling algorithm that yields less gradients for larger down sampling factors.

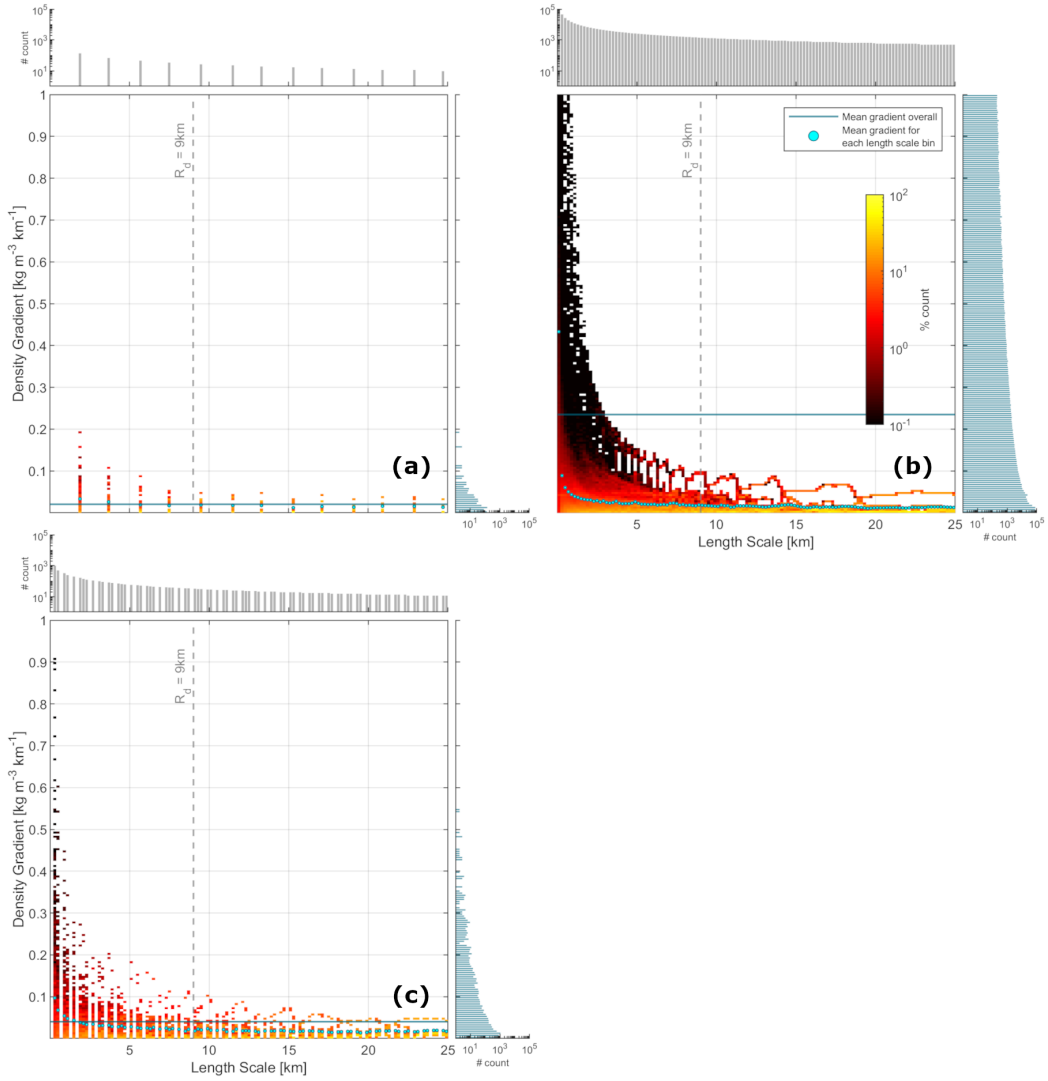

Figure 23. Distribution of lateral density gradients [kg m^{-3} km^{-1}] at various horizontal length scales (λ) [0.1 to 25 km] at 10 m depth for **(a)** EGC1-1, **(b)** EGC1-2, and **(c)** EGC1-3. The relative occurrence [%] of gradients at each length scale bin is displayed by the logarithmic color scale. The dashed gray line indicates the Rossby deformation radius R_d of the study region (Chelton et al., 1998). The marginal means (mean value over all gradients) are indicated by the teal line and the mean gradient for each each length scale bin is displayed by the teal scatters. The marginal distributions of the sampling length scales and the density gradients are displayed as univariate histograms on the horizontal and vertical axes, respectively.

As observed in Fig. 14c all three occupations of EGC1 exhibited aligning characteristics in the density signal at 10 m depth suggesting that an overall similar hydrography had been sampled. This allowed us to have insights into how the horizontal resolution in the data acquisition affects the joint distribution between density gradients and sampling length scales. Some variations in the histograms were plausible and already expected, they should, however, not to be disregarded in the analysis: The total number of gradients calculated lessened from > 780·10^3 for the constant depth tow to ∼6700 and ∼650 for EGC1-3 and EGC1-1 (Fig. 23), respectively. As a result, the relative contribution of density gradients at each length

scale gets much coarser.

Gradients at scales that were not resolved by the initial sampling rate got compensated causing a reduction of the covered variance in density gradients: for an initial sampling interval of 300 m, density gradients up to $0.925\,\mathrm{kg\,m^{-3}\,km^{-1}}$ were computed, and for a sampling interval more than six time as coarse the distribution does not exceed $0.2\,\mathrm{kg\,m^{-3}\,km^{-1}}$. Moreover, the amplitude of density gradients within the same length scale bins decreases, which is quite perceptible for EGC1-1 for which gradients in density just reached up to $0.195\,\mathrm{kg\,m^{-3}\,km^{-1}}$ within the length scale bin of 1.8-2 km, while density gradients got as high as $0.275\,\mathrm{kg\,m^{-3}\,km^{-1}}$ and $0.340\,\mathrm{kg\,m^{-3}\,km^{-1}}$ for the same spatial scale bin for EGC1-3 and EGC1-2, respectively. The distribution got more scarce especially along the length scale axis, which is a result of the resampling algorithm that can increases the sampling length scale only as fine as the initial resolution of the data set. Moreover, a decline of the mean over all gradients with a decreasing horizontal resolution ($0.040 \pm 0.001\,\mathrm{kg\,m^{-3}\,km^{-1}}$ for EGC1-3 and $0.020 \pm 0.001\,\mathrm{kg\,m^{-3}\,km^{-1}}$ for EGC1-1) could be observed emphasizing the loss of information at higher sampling frequencies.

Some features as observed in Fig. 23b remained rather unaffected by a reduced horizontal resolution, for instance, all bivariate histograms showed a dense occurrence of gradients around $0.03\,\mathrm{kg\,m^{-3}\,km^{-1}}$ and beneath, which is also reflected by only minor differences in the conditional means in density gradients.

While specific thresholds such as that no gradients greater than $0.1\,\mathrm{kg\,m^{-3}\,km^{-1}}$ and $0.2\,\mathrm{kg\,m^{-3}\,km^{-1}}$ are calculated for length scales larger than 8.8 and 3.8 km, respectively, and the additional layer of gradients as seen in the joint distribution of EGC1-2 were also found or indicated in the scale analysis of gradients along EGC1-3, all of these details got lost when subsampling the lowest resolved section. Similar alternations in the histograms by lower resolved data were observed also further north for EGC2 (Fig. 25).

The multi-modal pattern as inspected in the joint distributions in Fig. 23b,c exhibited somewhat artificial characteristics at first sight. Considering the thin-layer-patterns in the density distribution from resampling a step discontinuity (Fig. 22), and the original density measurements (Fig. 14c) which exhibited an abrupt rise in the signal resembling the inspected idealized case, we assumed that the additional layer consisted of real oceanic gradients. A technical issue in the resampling algorithm was ruled out. In order to verify these assumptions, the frontal area (defined as the rise in density between $x = 56\,\mathrm{km}$ and $x = 56.37\,\mathrm{km}$) was isolated from the resampling routine by excluding all gradients from the histogram that are formed by one sampling point west and one sampling point east of the defined area. Gradients calculated from sampling points in-between the frontal

structure were removed as well. Fig. 24a shows the bivariate histogram after applying this isolation technique on the density signal, which showed quite clearly the disappearance of the bi-modal distribution. In order to evaluate to what extent the frontal structure was contributing to the density distribution, we subtracted this distribution from the one of full variance in gradients and displayed the differences in Fig. 24b shaded with the raw number count. Around $14 \cdot 10^3$ gradients distinguished both distributions from each other accounting for a rather small part of the total amount of gradients ($\sim 780 \cdot 10^3$) of resampling the original data series. This is also reflected by barely affected statistical characteristics: the marginal mean is $0.230 \pm 0.001\,\mathrm{kg\,m^{-3}\,km^{-1}}$ and the conditional means also shifted to only slightly weaker fronts. The shape exhibited very similar characteristics as the gradient distribution obtained from subsampling a step discontinuity. We could observe a dominant layer of increasing gradients as the sampling frequency gets increased, accompanied by non-zero data pairs beneath that develop a pocket-like behaviour from around scales of 5 km and above.

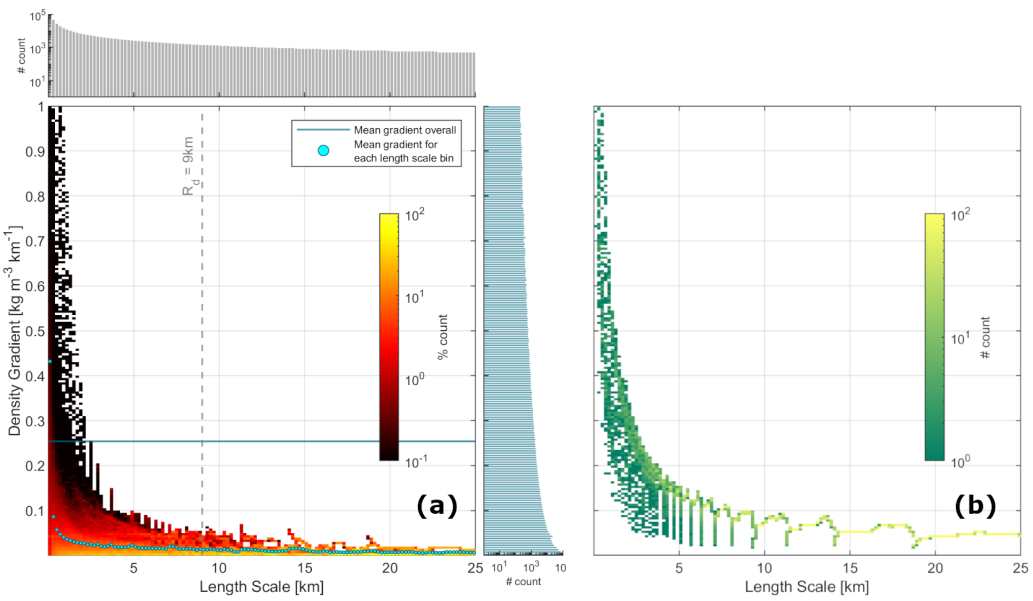

Figure 24. **(a)** Same as Fig. 23b after the application of an isolation technique as described in the text. **(b)** Distribution of remaining lateral density gradients [$\mathrm{kg\,m^{-3}\,km^{-1}}$] at various length scales (λ) [0.1 to 25 km] after subtracting the distribution as seen in (a) from the original one (Fig. 23b). The absolute occurrence [#] of gradients at each length scale bin is displayed by the logarithmic color scale.

The exclusion of a hydrographic feature as described above appeared to give detailed insights on its contribution to the overall joint distribution between density gradients and length scales. One might tend to apply this approach on other jumps in the density signal such as around $x = 108$ km or $x = 132$ km, which we expect to also contribute to the overall distribution similar as we have observed in Fig. 24. However, one has to bear in mind that the signal consisted of such jumps at various

length scales (an expanded view will reveal more and more jumps). Therefore, it seems infeasible to use this approach for the identification every pattern in a bivariate histogram and the assignment to a specific feature in a density signal.

More constant depth tows, which, as we have seen, provided detailed statistical insights, were conducted further upstream in the EGC allowing an investigation of regional differences in the scale sensitivity of density fronts. The gradient distribution calculated from data along EGC2-1 (Fig. 25a) exhibited a significantly larger marginal mean in density gradients ($0.360 \pm 0.002\,\mathrm{kg\,m^{-3}\,km^{-1}}$) than EGC1-2 suggesting an overall greater richness of the density structure at 10 m depth, especially in the submeso- and finescale. Although the amplitudes of density fronts at various spatial scales appears to not depend on the area along the EGC, one has to regard that the distribution in Fig. 23b was dominated by a single feature of the subsampled data series leading to a superimposing layer of gradients. Contrary, the joint distribution obtained further north exhibited no multi-modal behaviour but rather a filled pattern between the weakest and strongest fronts at almost all spatial scales. In addition, no distinct base of gradients could be observed due to a fairly even relative contribution of most gradients indicating a more homogeneous distribution of density fronts across the EGC in the north. As sections of both transects were conducted with hours to day in-between, it might be possible that the amplitudes of density gradients lessened from north to south due to changes of external forcing.

Deeper in the water column, at 30 m depth, fine-scale density fronts showed an even stronger presence as indicated by a larger marginal mean in density gradients ($0.580 \pm 0.002\,\mathrm{kg\,m^{-3}\,km^{-1}}$) and by larger conditional means, most noticeable for scales $\lambda < 5\,\mathrm{km}$. Larger gradients (>$0.3\,\mathrm{kg\,m^{-3}\,km^{-1}}$) occurred for a broader range of spatial scales and taking the color scale into account, it gets apparent that these gradients did occur rather frequently and accounted for a non-negligible contribution of $\sim$1% of gradients at these scales. As the two constant depth tows were conducted multiple hours apart, it is essential to consider that the hydrography could have developed to an extent that might have contributed to the observed differences in the gradient distribution at higher sampling frequencies. In this case, one would expect some sort of transitional distribution calculated from measurements along EGC2-2. Instead, such a transition was not observed and the histograms extracted from 10 and 30 m depth (Fig. 25b,c) resembled the distinct distributions from the constant depth tows, respectively, suggesting that the displayed variations in the histograms were actually related to the different depths of observation. The differences might be associated with the position of the tows with respect to the highly stratified layer as identified in section 3.1.1: While EGC2-1 was conducted

above it and partially crossed lenses of well-mixed water, the target depth of EGC2-3 corresponded to the depth by which this layer varied. A steepening of such interfaces, for instance due to the vertical displacement associated with internal waves, can drive a lateral redistribution of water masses of significantly different density, and thus, are especially susceptible for establishing horizontal density gradients.

Moreover, a distinct dip in gradients at length scales between 23 and 23.6 km appeared in the gradient distribution calculated along EGC2-3, very different to all the other histograms with more homogeneous distributions at scales above R_d.

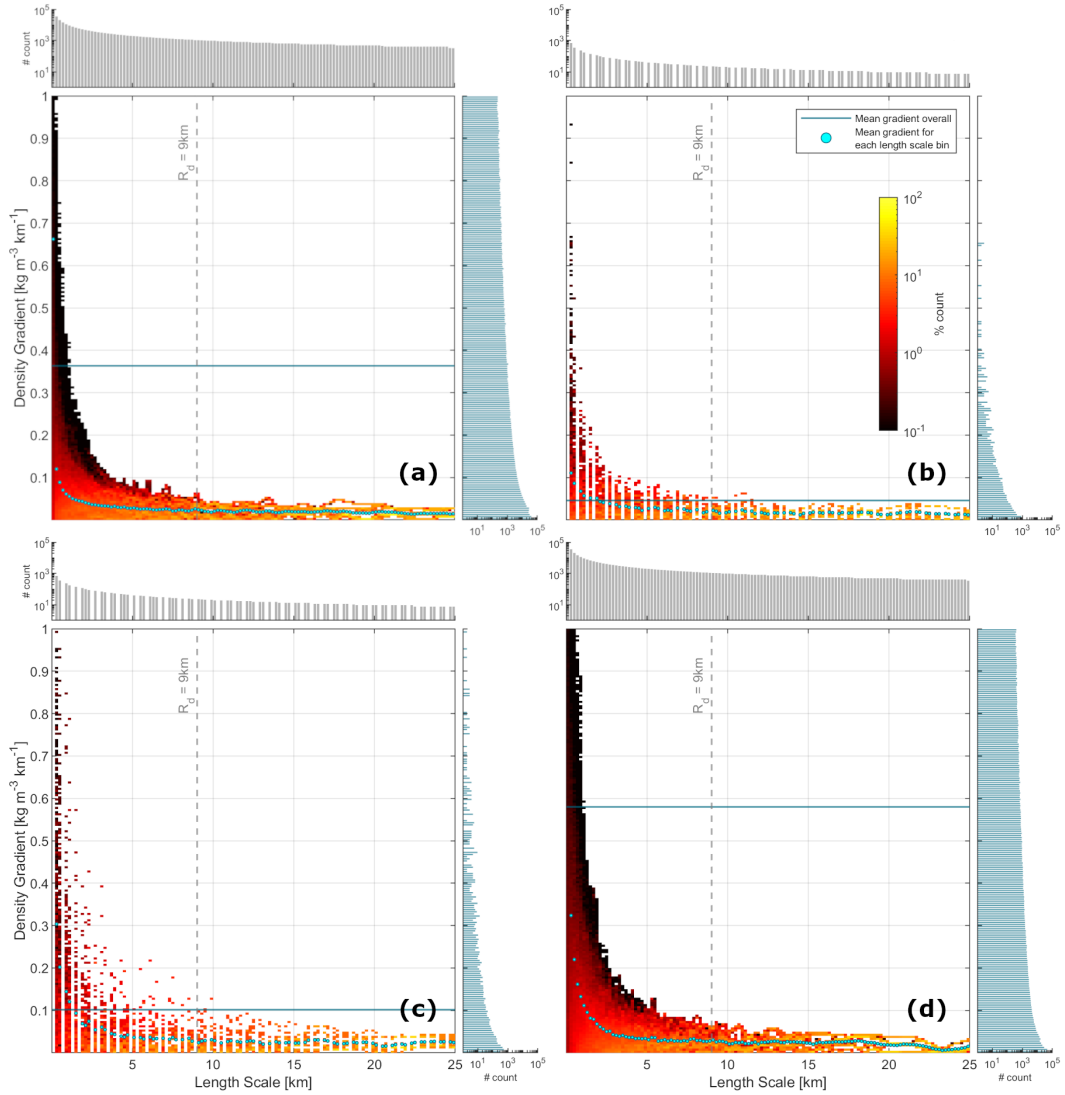

Figure 25. Same as Fig. 23, but for **(a)** EGC2-1, which was a constant depth tow at 10 m, **(b)** EGC2-2 extracted from an undulating tow at 10 m depth, **(c)** EGC2-2 extracted from undulating tow at 30 m depth, and **(d)** EGC2-3, which was a constant depth tow at 30 m.

Parametrization

As shown in the previous sub-chapter, the visual inspection of the bivariate histograms between density gradients and lateral spatial scales enabled a first look on meso-, submeso- and, finescale density fronts, the recognition of patterns/clusters, and even a regional comparison of joint distributions along the EGC. However, one half of the sections were operated with an undulating flight pattern providing valuable vertical information down to 50 and 300 m depth, respectively, with a vertical resolution of 0.5 m. As measurements at each depth grid are treated as independent discrete data series, one ends up with more than 750 joint distributions that are to be analyzed. So far, the descriptive approach served well for contrasting seven histograms over two distinct depths, yet, it will not be suited to assess the variability of density gradients over various scales for the full water column that was covered. For this reason, we fall back on a parametrization as described in 2.8. Exemplary visualizations of the estimate of k and a at various percentage marks for the constant depth tows are shown in Fig. 26. Even though this second half of the multi-scale analysis is introduced in order to avoid a side-by-side comparison of bivariate histograms, we once again compare those of the constant depth tows alongside each other highlighting two findings.

First, for EGC2-3 at 30 m depth we observed a stagnation of $|\nabla\rho(\lambda)|$ for around $\lambda < 0.1$ km at all relative proportions of the distribution contributing to a deviation from a strict power law (Fig. 26e,f). Despite the evidently different behaviour of the gradient spread at different sub-ranges of λ, regressions were yet performed over all observed scales in order to maintain a consistent procedure. Thus, the parameters got underestimated as addressed later on. This flattening of the envelopes toward the fine-scale was not observed for the other EGC sections at constant depth and undulating tows did not resolve variability in the density field at these scales.

Secondly, the outer envelopes for EGC1-2 (Fig. 26a,b) and EGC2-1 (Fig. 26c,d) with $a_{99\%} = 0.380 \pm 0.02\,\mathrm{kg\,m^{-3}\,km^{-1}}$ and $a_{99\%} = 0.270 \pm 0.001\,\mathrm{kg\,m^{-3}\,km^{-1}}$, respectively, suggested comparable horizontal variations in the density field along 71°08'N and further south of the EGC at 10 m depth - considering the outer envelope solely that is. Yet, lower percentage-marks featured a reversed ratio for both regions showing that the overall strength of density gradients and their decay rate with increasing length scale for EGC1-2 is weak relative to the gradient distribution obtained upstream of the EGC. This can be traced back to the previous observation that a distinct jump in the density signature as found in EGC1-2 contributed to a bi-modal layer of $(|\nabla\rho|, \lambda)$. Thus, the highest percentile of gradients appeared to not be necessarily representative for the whole bivariate histogram, which is why we will equally pay attention to the inner distributions in the following.

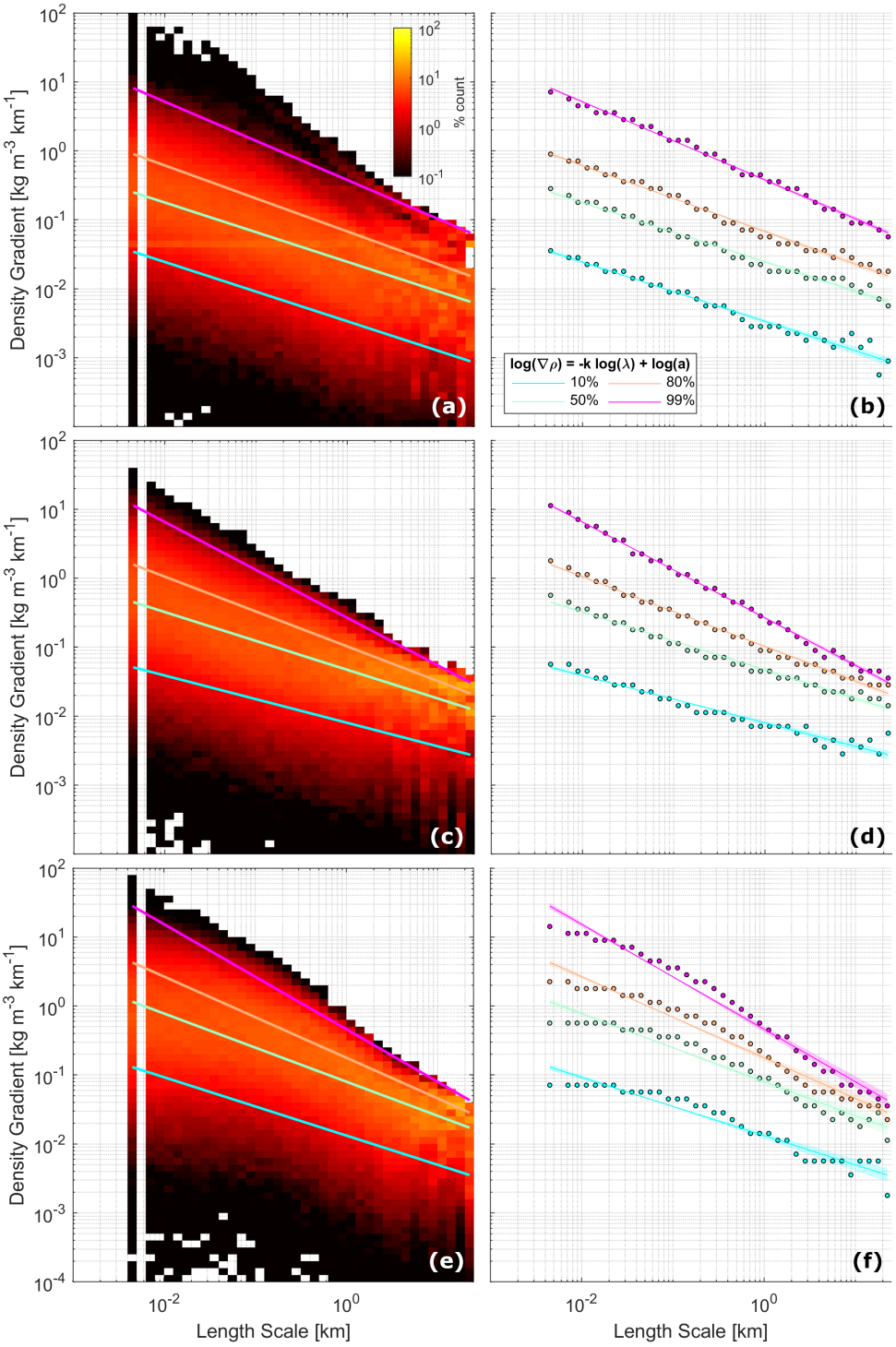

Figure 26. Distribution of lateral density gradients ($\nabla\rho$) [kg m^{-3} km^{-1}] at various horizontal length scales (λ) **(a)** at 10 m depth for EGC1-2, **(b)** at 10 m depth for EGC2-1, and **(c)** at 30 m depth for EGC2-3; note that the data pairs are distributed over uniform double logarithmic bins. The relative occurrence [%] of gradients at each length scale bin is displayed by the logarithmic color scale. The colored lines are the 10%-, 50%-, 80%-, 99%-envelope fits (cyan, green, orange, magenta) and discrete points used for the fitting are shown in **(b),(d),(f)** in the corresponding color. The shaded areas indicate the 95% confidence band from the uncertainties in the best-fit parameters a [kg m^{-3} km^{-1}] and k [].

The estimated slopes and y-intercepts for all depths of the EGC sections are displayed in Fig. 27. Contrasts in the strength and decay rate of the density gradients as determined for the 99%-envelope (Fig. 27 g,h) allowed a clear identification of multiple vertical regimes. The uppermost measurements are characterized by flat rate changes and by density fronts of lower magnitude corresponding to the layer dominated by a freshwater plume, solar warmed water and sporadic occurrences of well-mixed water (cf. Fig. 12, 13, and 15). A distinct intermediate steepening of $k(z)$ and rise in $a(z)$ covers a noticeable amount of the recorded water column (15-50 m depth) and can probably be assigned in a great part to the water identified as PSW. It consists of several sub-regimes as indicated by local minima and maxima in both the decay rate and magnitude of density fronts. Slight differences of the described subdivision of the upper water column mark regional variations of the scale dependency of the density fronts along the EGC.

Further north (in red) the overall horizontal density gradients gradually strengthen from the surface to the ceiling of the PSW and remain constant between 18 and 37.5 m ($a \approx 0.65\,\mathrm{kg\,m^{-3}\,km^{-1}}$). At the upper and lower boundary of this sub-regime, steep slopes ($k_{99\%}(18\mathrm{m}) = -0.99 \pm 0.06$ and $k_{99\%}(37.5\mathrm{m}) = -0.94 \pm 0.09$) indicate a strong decay rate. These boundaries coincide with the depths at which the layer of highly stratified water was up- and downlifted, respectively. From 36.5 m downwards the water column was purely occupied by PSW with no crossing of distinct interfaces (cf. Fig. 15) which is mirrored by a sudden decline in $a_{99\%}(z)$ and flattening of $k_{99\%}(z)$. This drop will be referred to as the core regime of the PSW.

Downstream of the EGC (in dark blue) both parameters change more sharply between the surface layer and the PSW. Two distinct sub-regimes cover the area between 14 and 22 m depth and between 28 and 46 m depth mirroring the steepwise deepening of the line of highly stratified water (cf. Fig. 13). The former, coinciding with the base of the observed freshwater plume, is marked by $a \approx 0.95\,\mathrm{kg\,m^{-3}\,km^{-1}}$ and again by two peaks in $k(z)$ at the upper and lower boundary ($k_{99\%}(14\mathrm{m}) = -0.86 \pm 0.08$ and $k_{99\%}(22\mathrm{m}) = -1.08 \pm 0.07$). The latter, coinciding with the ceiling of the PSW, features a lower variance of density gradients ($a \approx 0.43\,\mathrm{kg\,m^{-3}\,km^{-1}}$), which might be explained by the disruption of the line of stratified water and the occupation of the section by well-mixed water from the open sea.

Distributions obtained from data along EGC1-1 (in light blue) reveal that this regime extends further down to 55 m depth and another local maximum in the decay rate $k_{99\%}(56\mathrm{m}) = -1.2 \pm 0.2$, which could be associated with the boundary between solar warmed water and the ambient water of the Greenland Sea, followed by a significant drop of both parameters between 55 m and 120 m depth. This part of the water column was almost purely occupied by PSW and probably equals the

core regime as observed along EGC2-2. The much earlier and sudden drop for the last depth grid at 50 m depth as indicated by EGC1-3 is probably a result of an interpolation error. The deepest regime, which can only be observed for the undulating section down to 300 m depth, features values of the lowest magnitude for both parameters. This layer extends from 120 to at least 300 m depth and corresponds to the area of the water column that was occupied to a large part by AW and to a smaller extent by ambient water of the Greenland Sea. The transition between PSW and AW is indicated by a slight steepening of the slopes and strengthening of density gradients around 95 m depth. In general, the ocean interior exhibits much less variability in the scale dependency of density fronts and in the magnitude of density gradients compared to the upper water column.

Concerning the parametrization of the inner distributions, general flattening of slopes and decrease in a could be observed as the percentage threshold for the envelopes is lowered (Fig. 27a-f). The qualitative progression with depth as described for the outermost envelope remained more or less the same, only the vertical sub-regimes get smoothed out. Already for the 80%-envelope, peaks in $k(z)$ and abrupt changes in $a(z)$ are noticeably weakened suggesting that mostly upper percentiles of the bivariate histograms are actually impacted by boundary layers of different water masses. The approach of $k(z)$ towards less negative values indicates a weaker decay rate of density fronts with increasing spatial scales for the base of the distributions and a stronger dependency for higher percentiles. The decline in $a(z)$, representing an overall lower magnitude of horizontal density gradients, was an expected outcome for reducing the percentage mark for the best-fit regressions. The parametrization, however, encounters issues with the joint distributions obtained from EGC1-1 especially for 10 and 30% (Fig. 27a-d): There are great deviations between 15 and 30 m depth to the slopes as estimated for EGC1-3, which covered a resembling density structure as shown in 3.1.1. One could argue that the parameters lie in each others confidence intervals, but in case of EGC1-1 uncertainties are so large that the validity of the estimated slopes and y-intercepts are rather questionable. Moreover, between 18 and 20 m depth $k > 0$ are estimated suggesting a positive correlation between density gradients and lateral spatial scales. This would suggest that the density gradients strengthen with increasing length scale, which we presume is not a real oceanographic observation but rather a result of the failure of the parametrization for lower envelopes. The poor performance of the envelope fitting might be attributed to the sparse resolution of the data input that caused sporadic histograms (cf. Fig. 23a). In general, parameters obtained for EGC1-1 exhibit large uncertainties at all envelopes, and thus, should be treated with caution in the analysis.

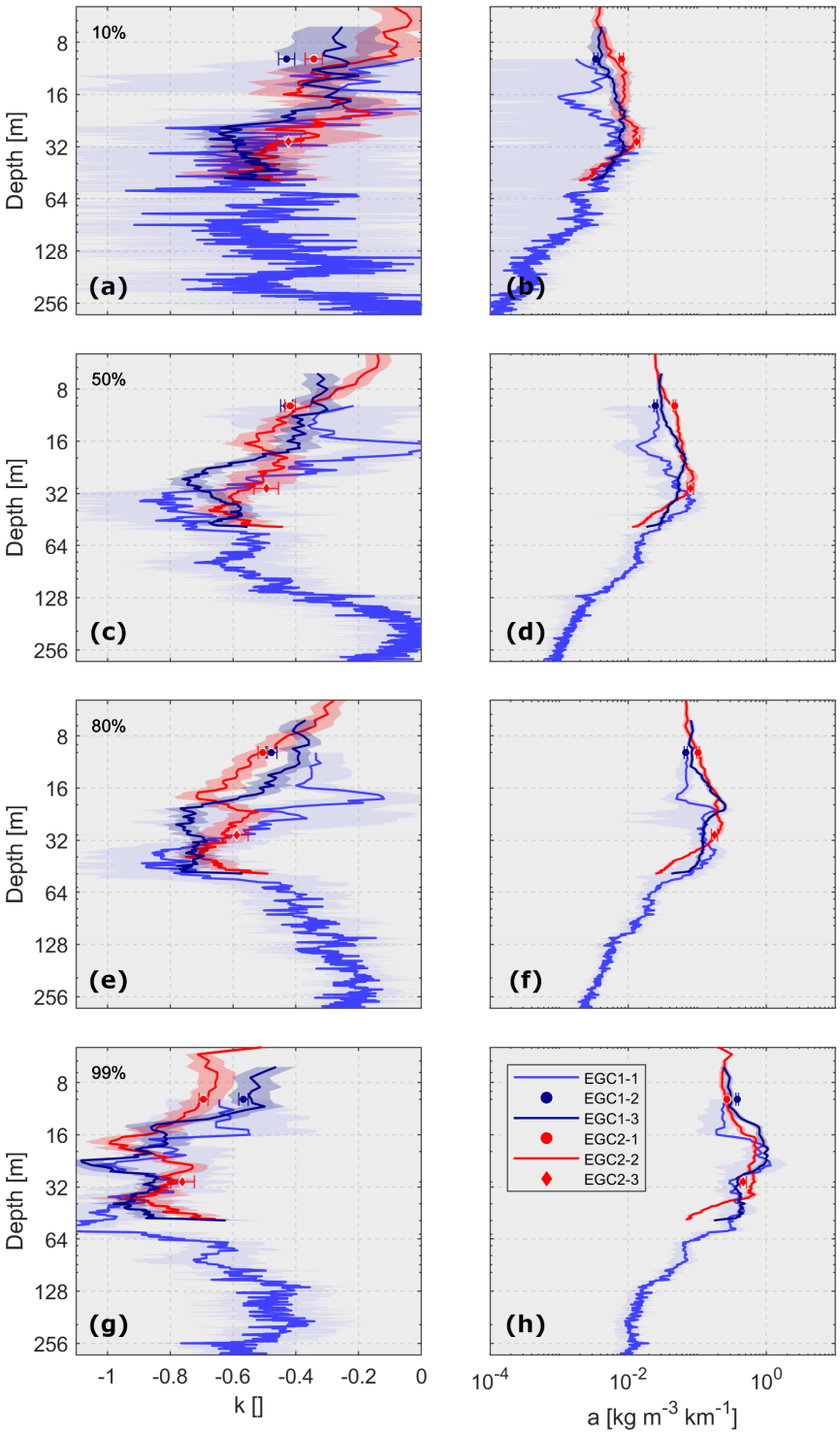

Figure 27. (Left panel) Estimated power law exponents (k) and **(right panel)** normalization constants (a) [kg m^{-3} km^{-1}] determined by a linear regression through the **(a),(b)** 10-, **(c),(d)** 50-, **(e),(f)** 80-, and **(g),(h)** 99%-envelope of the joint distributions between density gradients and horizontal length scales for all conducted EGC sections at various depths z. The shaded areas and error bars indicate the 95% confidence intervals. Note the non-linear scale for depth (z) [m].

Having another look on k and a for the constant depth tows (scatters) reveals not too large deviations from the decay rates and strengths of density gradients as estimated for the undulating tows with a turning point at 50 m depth, and thus data sequences of lower horizontal resolution (cf. Tab. 1). There is actually a good agreement (considering the uncertainty bands) for most distributions. One exception is $a(z)_{99\%}$ for EGC2 at 30 m depth, which might be attributed to the stagnation of density gradients for $\lambda < 0.01$ km as found in Fig. 26e,f causing lowered values in both parameters. As this baseline initiated not earlier than a spatial scale of 0.1 km it could not be predicted by the lower resolved measurements of EGC2-2. However, the observed stagnation appears not to stay in conflict for the lower envelopes. Other exceptions are $k(z)_{80\%}$, $a(z)_{80\%}$, and $a(z)_{50\%}$, which could have arisen from the long delay between both sections. Even though, the overall density signal was considered similar, submeso- and finescale structures could have developed to an extent that impacts the gradient distributions.

3.3 A global perspective

In the previous section, we demonstrated the functionality of our statistical pipeline using data from the EGC and we have seen distinct distributions between density gradients and horizontal length scales for different vertical regimes. To provide a more comprehensive understanding of the scale-dependant nature of density gradients and how it differs for different oceanic regimes, we upscaled the multi-scale analysis to all regions around the world, where the topAWI had been operated (cf. Fig. 5). A side-by-side depiction of all vertical sections of potential density anomaly is shown in Fig. 28.

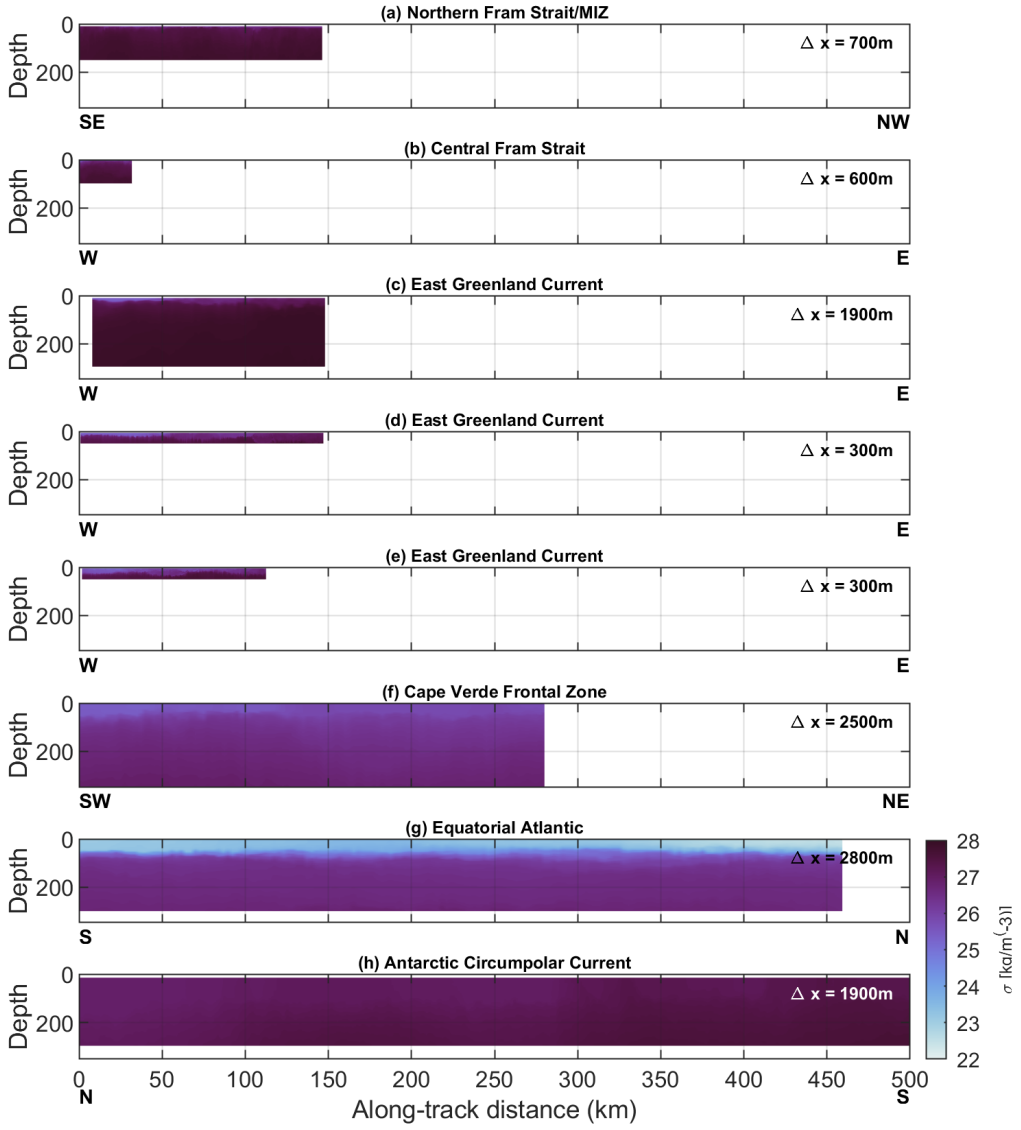

Figure 28. Gridded vertical sections of potential density anomaly (σ_θ) [kg m^{-3}] obtained **(a)** in northern Fram Strait, **(b)** in central Fram Strait, **(c)-(d)** across the East Greenland Current, **(e)** in the Cape Verde Frontal Zone, **(f)** in the equatorial Atlantic, and **(g)** across the Antarctic Circumpolar Current. Note, that the reference point (0 km) for the along-track distances corresponds to different geographic coordinates for each vertical section

The parameters k and a as estimated for the different regions at various depths are shown in Fig. 29. It should be noted that parameters were estimated for the 10%-envelope because they are part of the statistical pipeline. However, they exhibited large uncertainties, a high variability with depth and unexpected values (f.e. positive slopes). We therefore do not consider them in the following.

Largest values for $a(z)$ at all percentage marks were computed for the uppermost measurements of the ice-affected sections, that is in central and northern Fram Strait (Fig. 29 left panel). No apparent differences could be found suggesting that the direct presence of ice or its presence in close proximity had a similar impact on the richness in the surface density structure. A sharp drop in $a(z)$ was observed down to 42 m depth, where the two areas started to exhibit slightly different degrees of strength in density gradients: In northern Fram Strait a monotonous decline in $a(z)$ was indicated, albeit much less pronounced than seen in the upper part of the water column. In central Fram Strait, an intermediate maximum in $a(z)$ appeared around 80 m depth, which also coincided with the strongest correlation between density gradients and horizontal length scale ($k > 1.3$) found for all regions. The latter was corresponding to a subsurface front as discussed in Hofmann et al. (2024). The strength of density gradients reduced as the percentage of data below the curve is reduced (Fig. 29b,d,f), similar to the observations made across the EGC, yet distinct features such as the kink in $a(z)$ between the ice-affected surface layer and the subsurface spanning a lower range of gradients, or the intermediate rise as found in central Fram Strait, did not smooth out. Despite a similar vertical development of the density gradient variability, both regions demonstrated a very different complexity in their length-scale sensitivity: Across the MIZ, $k(z)$ showed a comparable qualitative development as described for $a(z)$ for the lower percentage marks, while for the outer envelope density gradients scaled much stronger with the spatial scale again between 120 m and 150 m depth. In Fram Strait, further steep slopes were estimated around 32 and 50 m depth, however, they smooth out for the other percentage marks suggesting a weaker scale-sensitivity for most gradients of the distribution.

The equatorial Atlantic was characterized by much weaker density gradients within the upper layer as indicated by lower values in $a(z)$ associated with the ML, which is a behaviour that was found in the northern polar areas. We found larger values in $a(z)_{99\%}$ for the uppermost measurements, yet this local maximum disappeared for lower percentage marks revealing a rather constant value within the ML. A distinct strengthening of density gradients started around the mean base of the ML (22.8 m) and continued down to around 70 m depth, which roughly corresponds to the core of the EUC (cf. section 3.1.4). The undercurrent exhibited a wide span of density gradients as revealed by values in $a(z)$ comparable to the ones found in the meltwater-layer in northern Fram Strait and the PSW-layer of the

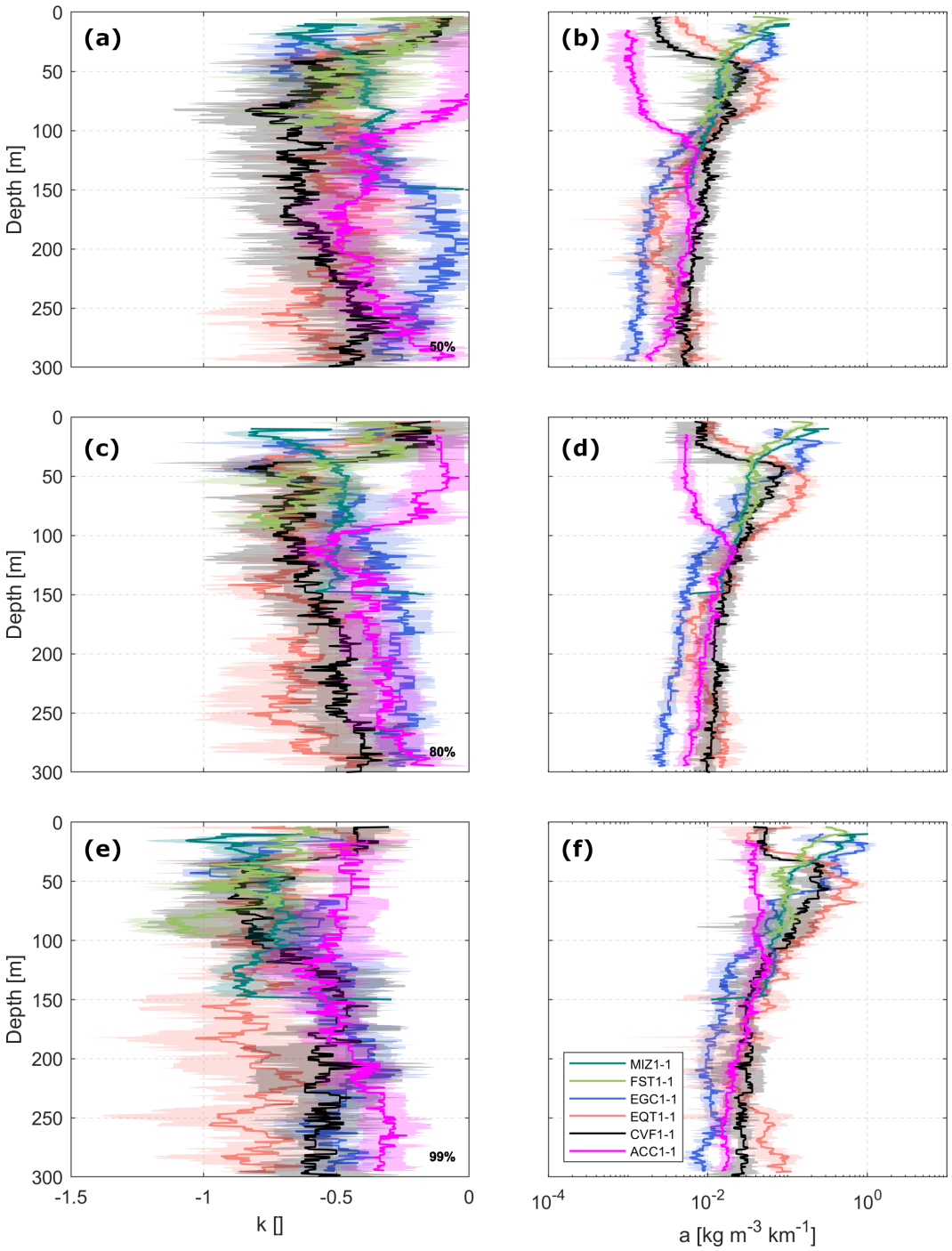

Figure 29. (Left panel) Estimated power law exponents (m) and **(right panel)** normalization constants (b) [kg m^{-3} km^{-1}] determined by a linear regression through the **(a),(b)** 50-, **(c),(d)** 80-, and **(e),(f)** 99-envelope of the joint distributions between density gradients and horizontal length scales for all conducted topAWI sections at various depths z. The shaded areas and error bars indicate the 95% confidence intervals.

EGC at all percentage marks. In geostrophic balance, lateral density gradients can result from flows of different velocities. In the EUC geostrophic balance break down as the Coriolis parameter $f \approx 0$, yet somewhere to the northern and southern end of the section f is large enough for balanced motion to reappear. From that depth downward the strength of density gradients lessened for greater depths probably indicating the lower boundary of the EUC at 110 m, where the strength of density gradients got as weak as within the mixed layer and continued declining more slowly with depth until 220 m. There, $a(z)$ started to increase for all sub-distributions much different to the other study regions that maintain the decline at these depths. In regard to the decay rate of the gradients, we estimated relatively flat slopes within the mixed layer with almost no scale dependency for all gradients below the 80-percentile and varying values around -0.80, -0.70, and -0.55, within the ocean interior for 99%, 80%, and 50% respectively without noteworthy differences between the EUC and the deeper layers. The latter suggests that hydrographic features with stronger density gradients across the range of length scales do not necessarily come with a strong rate of change with the length scale.

Similar progressions in the strength of density gradients were found further north in the CVFZ, where a low variance of density gradients was also estimated within the mixed layer followed by a sudden jump slightly above the mean base of the ML (41.8 m). The maximum indicated slightly weaker density gradients than found in the EUC and are only maintained over few depths before $a(z)$ gradually declined along the stratified water column between 65 and 150 m. A sub-regime in $a(z)_{99\%}$ is found beneath introduced by a kink in the curve characterized by almost constant values between 150 and 300 m depth. For the inner gradient distributions this split of the stratified interior got less and less noticeable. A qualitatively similar progression is exhibited by $k(z)$ for 99% and 80% indicating the strongest correlation between density gradients and horizontal length scale at the MLD. The transition from mixed layer to stratified water is also indicated by the slopes estimated for 50%, however, the density gradients scaled stronger with the length scale deeper down at 80 m depth.

The overall weakest density gradients and correlation to the horizontal length scale were found in the Southern Ocean across the ACC with little variability of both parameters over depth compared to the other study regions. The mixed layer exhibited almost constant values for $a_{99\%}$ and $k_{99\%}$ with slight increases at the base of the deep mixed layer (113.6 m) followed by a minor and gradual decline in both parameters for greater depths, which remained almost constant between 250 m and 300 m. For the other percentage marks, the mixed layer and the stratified water were more distinguishable due to a sudden rise in $a(z)$ and especially $k(z)$ - this flip in the qualitative progression suggested that the distributions within the mixed layer were much more impacted by density gradients closer to the upper boundary

of the distribution at higher sampling frequencies. The mixed layer was characterized by slopes close to zero at 80% and 50% indicating a very small correlation between gradients and length scales potentially for the vast majority of the distribution. At 80% a nose formed between the MLD and 140 m and even there $k(z)$ only got as steep as -0.55. And at 50%, similar to what was observed for the same percentage mark in CVFZ, $k(z)$ did not peak at the base of the mixed layer but further down at around 160 m depth.

In general, the joint distributions between density gradients and lateral scales reveal region specific characteristics within the upper water column before getting close to each other at about 100 m in terms of the richness of the density field and remaining close down to the lowermost measurements. The EGC was an exception showing a progressing departure in $a(z)$ from all the other areas in the stratified interior. The decay rate and variability in density gradients are peculiarly correlated that every rise in $a(z)$ is accompanied by a steepening of $k(z)$, but both parameters do not scale proportionally with each other leading to distinct qualitative progressions in and statistical differences between most regions. Thus, the study regions do not exhibit common decay rates in the ocean interior. Moreover, the percentile of a gradient distribution that is assessed has a considerable influence on the vertical development of decay rate and magnitude of density gradients.

3.3.1 Depth dependency of density gradients

We used $a(z)$ as a measure for the strength of the density gradients, however, exact magnitudes of density gradients are not assessed by the parametrization. For this reason, we utilized bivariate histograms once again to display the distribution of density gradients over various depths (Fig. 30). While no information about the scale sensitivity could be drawn by this data presentation, it provided additional insights on the progression of $a(z)$. As shown in previous paragraphs, smaller length scales yields larger density gradients. In order to achieve a less biased comparison between gradient distributions covered over different ranges in the sampling length scale, only gradients computed for length scale between 3 km and 1.9 km are displayed for this particular presentation.

In general, the envelope of the highest percentiles resembled the qualitative progression of $a(z)_{99\%}$ verifying that the normalization constant can indeed be used as a measure for the gradient richness of the corresponding density field. Near- and subsurface water exhibited region-specific variability of the density field, while the interior at all study areas is characterized by rather weak density gradients getting as low as $0.003\,\mathrm{kg\,m^{-3}\,km^{-1}}$ as observed in the warm core of the EGC (Fig. 30c).

Regions under the influence of melt water exhibited the largest density gradients among all study areas. In the PW layer of the EGC, we found submesoscale density gradients of around $2\,\mathrm{kg\,m^{-3}\,km^{-1}}$ (Fig. 30d,e), while data from EGC1-1

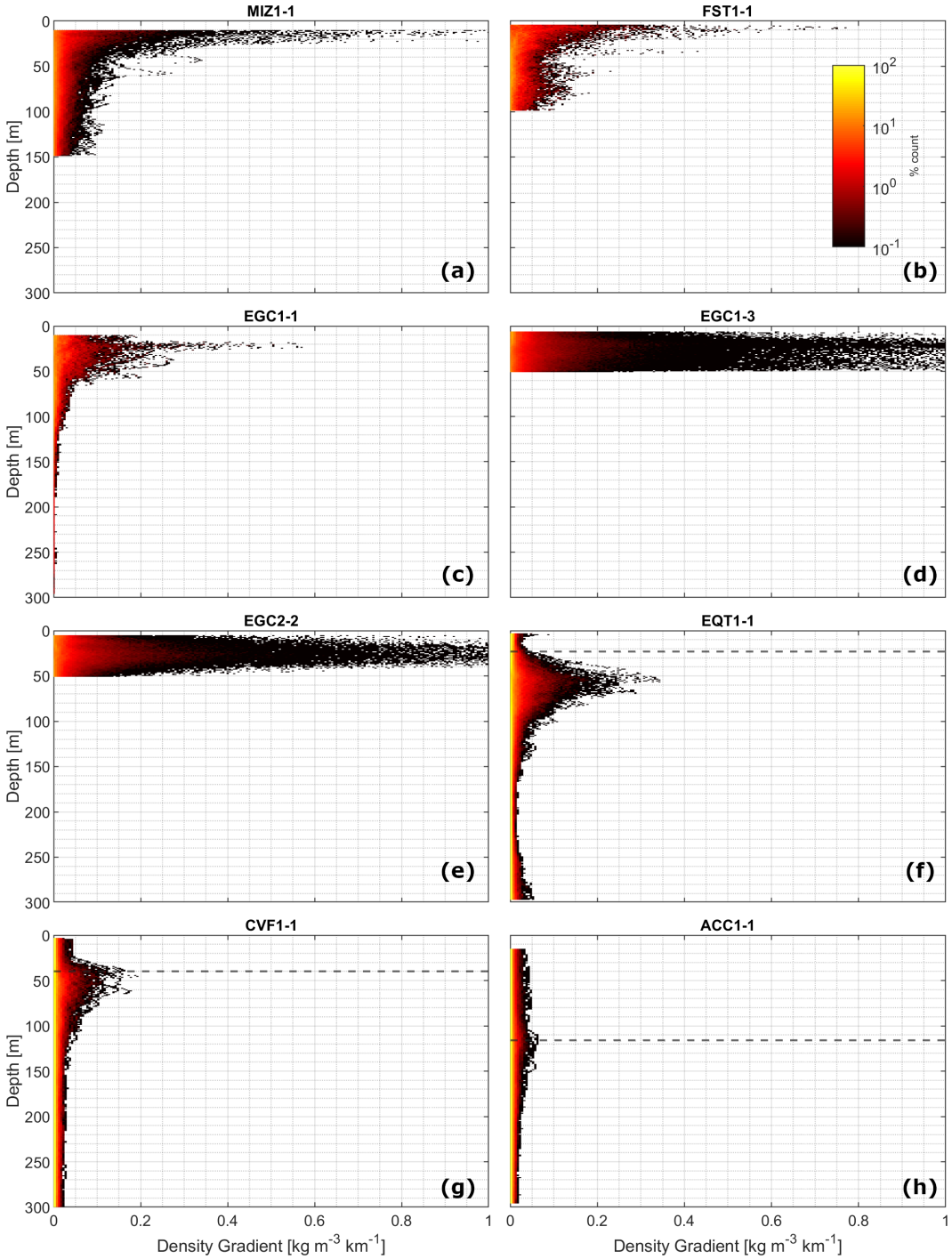

Figure 30. Distribution of lateral density gradients ($\nabla\rho$) [kg m^{-3} km^{-1}], calculated from various sampling length scales (1.9-3 km), at various depths (z) [m] for **(a)** MIZ1-1, **(b)** FST1-1, **(c)** EGC1-1, **(d)** EGC1-3, **(e)** EGC2-2, **(f)** EQT1-1, **(g)** CVF1-1, and **(h)** ACC1-1. The relative occurrence (%) of gradients at each depth bin is displayed by the logarithmic color scale. The MLDs (if identified) are indicated by the dashed black lines.

suggest that gradients did not exceed 0.57 kg m^{-3} km^{-1} there. This indeed is inconsistent with the previous evaluation of parameter $a(z)$ that demonstrated that the strength of gradients is of similar magnitude for all occupations of EGC1. In

northern and central Fram Strait the uppermost layer is characterized by weaker lateral density gradients up to $1\,\mathrm{kg\,m^{-3}\,km^{-1}}$ and $0.77\,\mathrm{kg\,m^{-3}\,km^{-1}}$, respectively (Fig. 30a,b). The stepwise subduction as observed in central Fram Strait is associated with an intermediate, albeit much less pronounced, peak of density gradients of around $0.2\,\mathrm{kg\,m^{-3}\,km^{-1}}$. Moreover, lateral density gradients in this frontal regions are more evenly spread as indicated by a rather uniform color shading (a similar observation was made for EGC1-1 in Fig. 30c) when compared to the gradient-depth distribution as computed for data from the MIZ north of Svalvard.

In the mid-latitude regions, the core of the EUC stood out with a maximum horizontal gradient of $0.35\,\mathrm{kg\,m^{-3}\,km^{-1}}$. In the previous section, our statistical pipeline indicated that the EUC comes close to the variability of the density field as observed in regions influenced by sea-ice. This was not shown by assessing absolute values for the density gradients, which highlights that the upper 1% of density gradients, which was excluded in the parametrization, yet included in Fig. 30, would presumably contribute to qualitatively unequal properties of the gradient/length scale distribution as the 99-percentile.

Minimal variety in gradients along the depth axis distinguished the ACC (Fig. 30h) from the other regimes. Here, lateral density gradient only got as high as $0.06\,\mathrm{kg\,m^{-3}\,km^{-1}}$ at the mean MLD. For all regions for which a ML could be determined, the submesoscale gradient variability within their ML remained roughly as low as in their interior ($<0.04\,\mathrm{kg\,m^{-3}\,km^{-1}}$).

3.3.2 Fractal dimension

The fractal dimension D as estimated for all regions is displayed in Fig. 31b, whereby an exemplary determination via linear regression is shown in Fig. 31a. The multi-occupation of the EGC crossings revealed matching values in D for different sampling intervals supporting that our methods works. In general, the qualitative progression along the water column and the global differences resembled the behaviour of $k(z)_{80\%}$ suggesting a high correlation between those two quantities. This was especially evident for regions that exhibited disproportional scaling between the decay rate and strength of the density gradients such as central Fram Strait and the equatorial Atlantic. The lowest geometrical complexity in the horizontal density field was found within the mixed layers with $D < 0.2$. As the respective MLDs are approached the dimensions rose to values multiple times as large. Deep sections revealed that the interior of most regions was characterized by a lessening of fractal properties as progressing in depth. The largest values in D (> 0.8), indicating a scale-invariant, self-similar density field, were found in the ice-effected regions. Especially melt water, PSW within the EGC, and AW limbs in the front study in Fram Strait appeared to be abundant in small-scale fluctuations in the density field. A distinct correlation between vertical stratification and the fractal dimension could not be observed. It should be noted that for many density signatures, $L(\lambda)$ actually exhibited distinct slopes for different ranges of λ. These sub-scales, however, did not only varies between regions but also through the water column of the same region, which is why we performed the linear regression over all scales. Thus, some values for D might have been under- or overestimated.

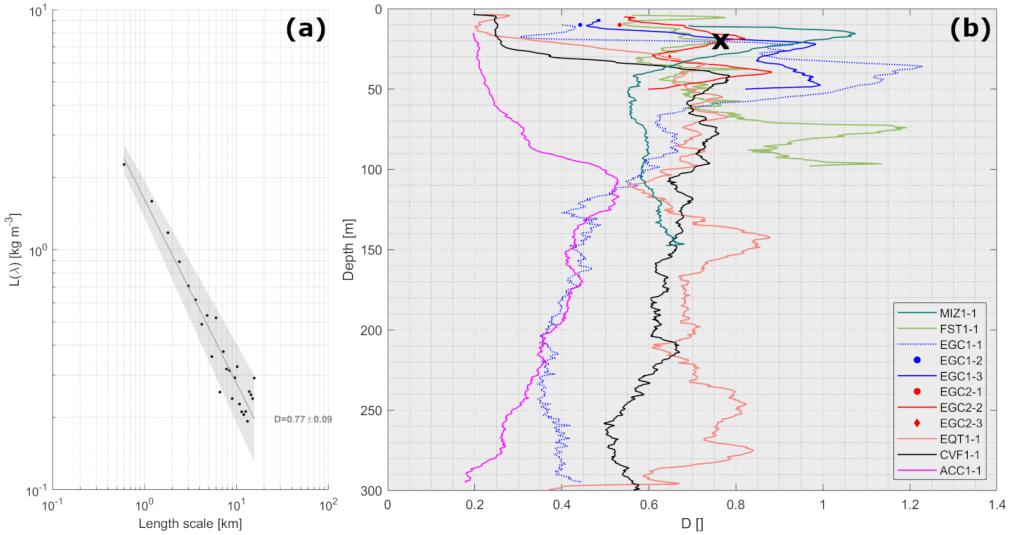

Figure 31. **(a)** Fractal length (L) [kg m^{-3}] for various length scales (λ) [km] at 20 m depth for FST1-1. The shaded area indicate the the 95% confidence band from the uncertainties in the best-fit parameters. **(b)** Estimated fractal dimensions (D) for all conducted topAWI sections at various depths z. The black cross indicates the value of which estimation is shown in **(a)**.

3.3.3 Density ratio over varying horizontal scales

We have seen in the previous section that the joint gradient distributions as estimated for the study regions have overlapping properties, despite environmentally different settings. In order to assess and globally contrast the combination of TS variations that direct the density gradients we compute the density ratio R (eq. 4) for different length scales. Again, bivariate histograms were utilized for the visual evaluation of the statistical distributions of R and generated for each depth grid - individual ones were picked to emphasize differences between the oceanic regimes and to highlight noteworthy features in the water columns. While we used the median (red line) of R at varying scales as a simplified approach to describe the scale-sensitivity of the quantity, the overall R/λ distribution should not be neglected in the following.

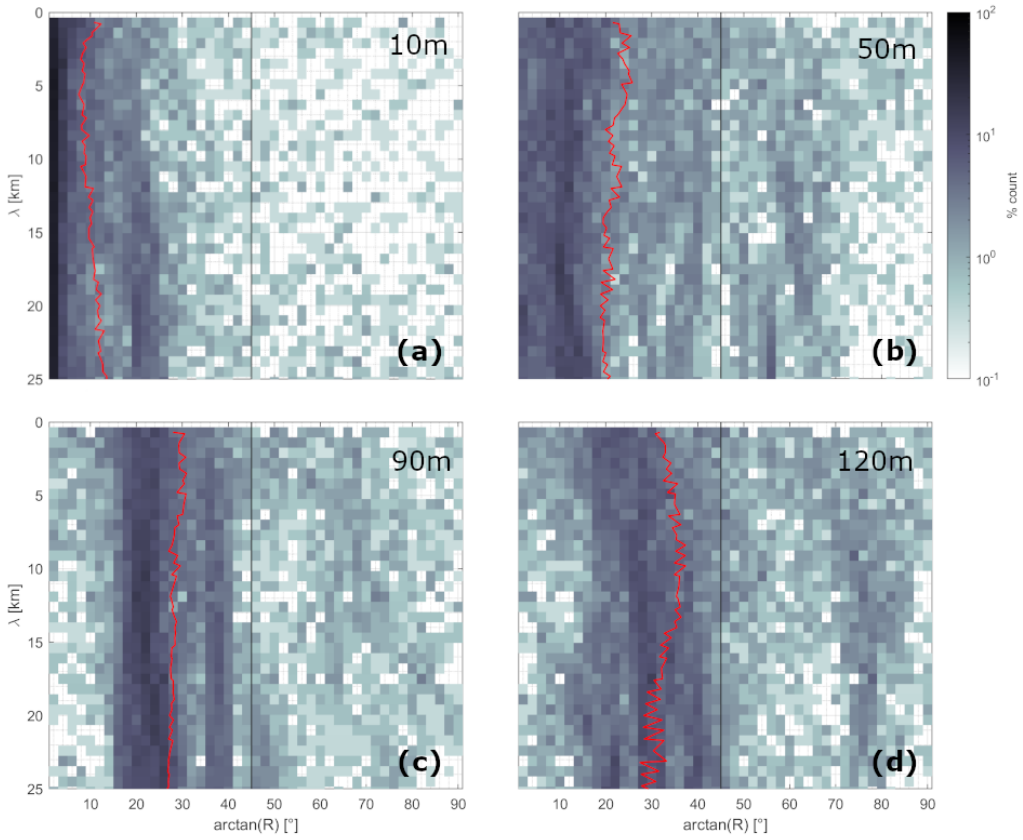

Figure 32. Distribution of the arc-tangent of the density ratio (R) [°] at various horizontal length scales (λ) [km] for MIZ1-1 at **(a)** 10 m, **(b)** 50 m, **(c)** 90 m, and **(d)** 120 m depth. The bin sizes along the y-axis equal the mean sampling interval of MIZ1-1. The relative occurrence [%] of gradients at each length scale bin is displayed by the logarithmic color scale. The red line indicates the median of arctan(R) at each length scale bin. The vertical grey line at 45° correspond to $R = 0$ indicating the transition from salinity dominance to temperature dominance.

In general, areas in the polar regions were characterized by a salinity-driven density field and the gradients estimated at lower latitudes exhibited a temperature domination, fitting the simplified pattern of alpha and beta oceans. The MIZ (Fig. 32) showed a distinct salinity contribution at the surface with a shift of the median toward larger values for increasing spatial scales. A minimum of around $\arctan(R) = 10°$ was found for $\lambda = 2.1$ km, which might be related to the scale of the dominating freshwater structures. As the vertical distance to the surface is increased (Fig. 32b,c), gradients reveal a higher compensation with a rather centered distribution, indicative for a declining influence of the sea ice with depth. For depths below 100 m (Fig. 32d), gradients between length scales of 17.5 km and 25.2 km remained rather unchanged, while the density field at smaller scales continued to approach a more compensated state. The vertical progression suggests a homogenization of the density field with depth, which corresponds well with the decline in the strength of the fronts as shown by the parametrization of the gradient distributions (cf. Fig. 29). Moreover, depths at which the median departed from a centered position coincided with the estimation of steep slopes.

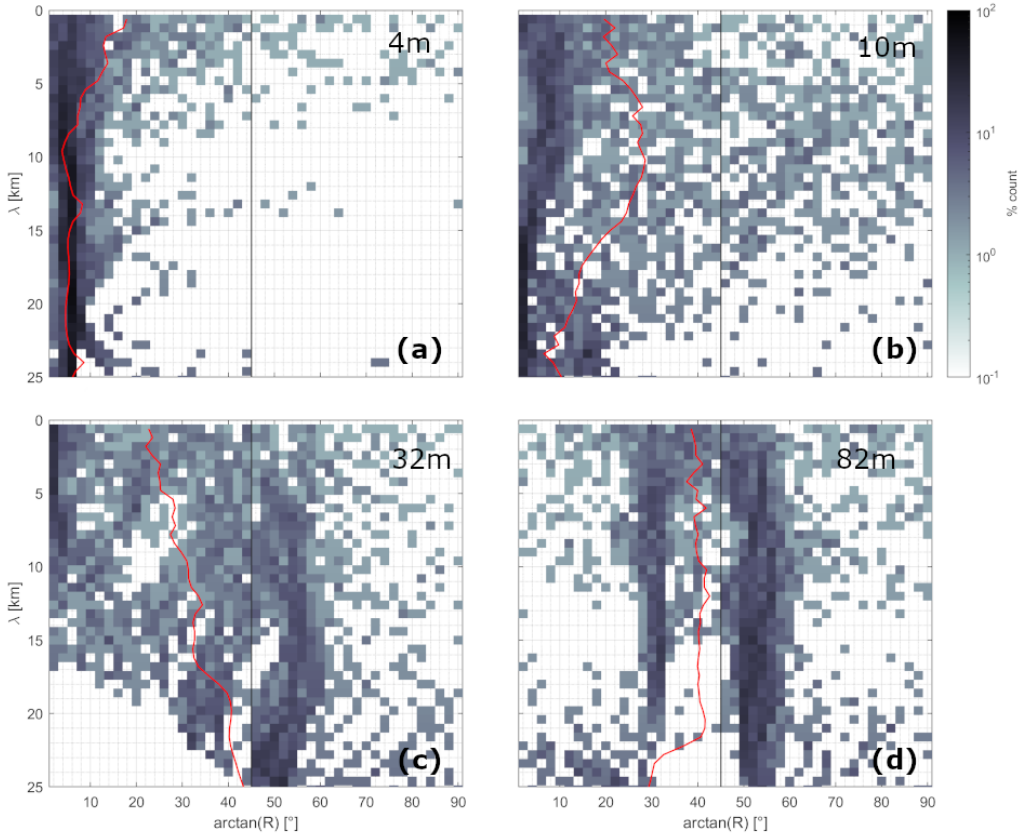

Figure 33. Same as Fig. 32 except for FST1-1 at **(a)** 4 m, **(b)** 10 m, **(c)** 32 m, and **(d)** 82 m depth. The bin sizes along the y-axis equal the mean sampling interval of FST1-1.

In central Fram Strait, the bivariate histograms revealed a compensation of salinity-driven gradients from the surface to the interior at all scales. The development of the density field, however, exhibited a higher complexity in regard to its vertical progression of the TS patterns (Fig. 33). At the very surface, we found a distinct salinity domination with a centered median between 10.2 km and 25.2 km. For the lower submesoscale, gradients appeared to be increasingly compensated as the spatial scale was reduced. Not only does the scale-dependence of the median R-ratio oppose the one observed at the surface of MIZ1-1, which might also be related to the different decay rates of density gradients with λ (cf. Fig. 29), moreover, the general distribution is clearly one-sided with a sporadic occurrence of $\arctan(R) > 45°$. Further down, the spread of $R(\lambda)$ develops a weaker salinity contribution for intermediate scales (around 4.9 - 15.4 km) with lower values in R for the smallest and largest observed scale (Fig. 33b) before exhibiting a drastic change from 30 m depth downwards (Fig. 33c). This change involved an increasing occurrence of temperature-driven variability for increasing length scales resulting in a median with an almost linear progression from salinity-driven small-scale structures to a median large-scale compensation at the largest scales displayed. This distinct scaling behaviour coincides with the vertical peak in the decay rates as estimated for all percentage-envelopes (cf. Fig. 29), which has been associated with the subsurface front of a step-wise water mass subduction. The described multi-scale distribution of R is maintained for few depths only before moving back to a more centered median at all observed scales. From 80 m depth downwards (Fig. 33d) two sub-ranges developed - for $\lambda > 20.3$ km the median of $\arctan(R)$ approaches perfect compensation, while the density field reveal a growing salinity contribution for larger scales coinciding with a second peak in $k_{99\%}$. Note, that whenever the median indicates compensation in the frontal system, it is rather a result of a distinct band of temperature dominated variability ($\arctan(R)$ between 50-60°) of the density field, which occupies a wider span of spatial scales with increasing depth and could be related to the AW limbs.

On the other hemisphere, salinity-driven gradients, yet much more compensated than in Fram Strait, were found across the ACC (Fig. 34). The median R-ratio remained mostly unaffected around 35° at all scales down to 165 m depth. Around the MLD (Fig. 34b), the density field exhibited slightly higher salinity contributions. From 165 m depth downwards the median of the R-ratio started to depart from a centered spread and approached $R = 45°$ at scales beyond 15 km (Fig. 34c). At around 223 m depth small-scale structures of the density field started to approach larger values in R as well. Eventually, toward the lowermost measurements, the TS patterns reached almost perfect compensation for scales between 0 and 10 km (Fig. 34d). In general, the vertical development of the $R(\lambda)$ distribution rather coincides with the estimated progression of $k_{50\%}$. Despite the small changes of the median

line, one could observe that the color shading of the histograms became more uniform with depth eventually showing an even occurrence of all arctan(R) values at all scales. This is a feature only found across the ACC.

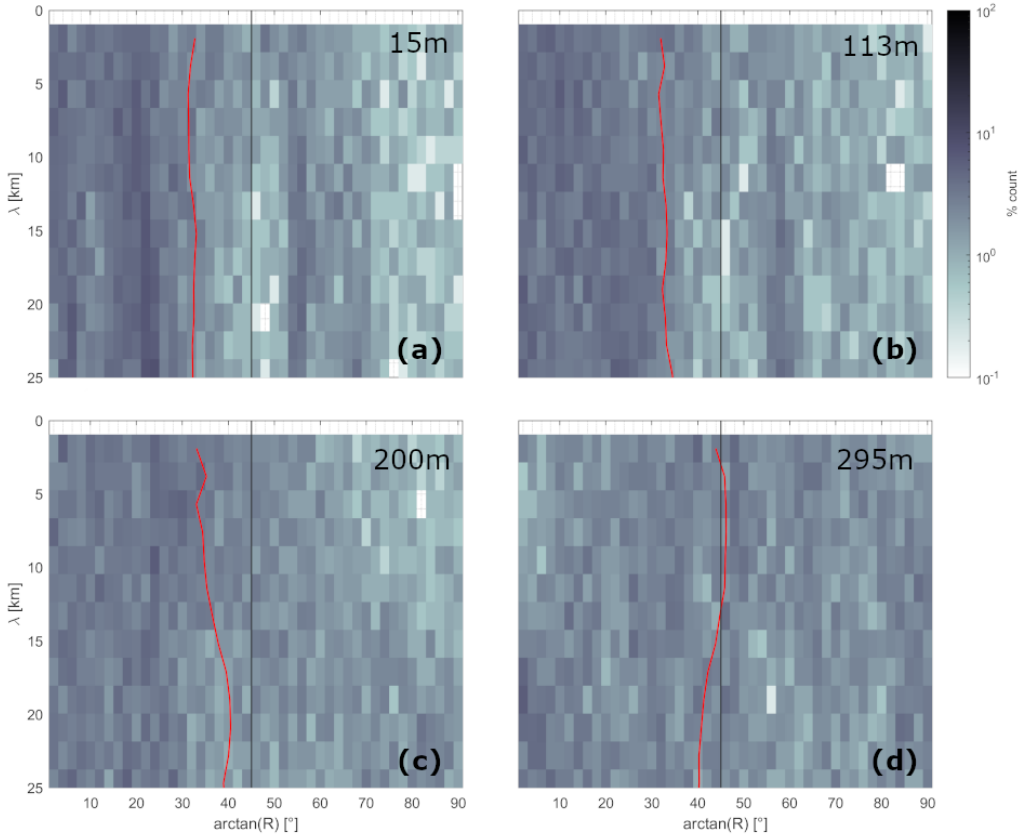

Figure 34. Same as Fig. 32 except for ACC1-1 at **(a)** 15 m, **(b)** 113 m, **(c)** 200 m, and **(d)** 295 m depth. The bin sizes along the y-axis equal the mean sampling interval of ACC1-1.

The lower-latitude regions revealed temperature-driven density gradients. Within the mixed layer of the equatorial crossing the TS patterns varied around perfect compensation (Fig. 35a). As the MLD is crossed, the density field develops a pronounced temperature contribution (arctan$(R) > 45°$) and reached its maximum of around 75° at 55 m depth (Fig. 35b) corresponding with the core of the EUC where we found a gradient field of similar strength as at the (near-)surface in Fram Strait. It highlights that the newly introduced parameter $b(z)$ alone might be insufficient for distinguishing oceanic different regimes and the need of complementing quantities such as arctan(R) for detailed comparisons. Further downwards until the lower boundary of the counter current (Fig. 35c), the T-dominance weakened and reached a median of arctan$(R) = 64°$. The TS-contribution of the density field remained unchanged for the rest of water column as indicated by the median line, but the overall distribution indeed developed a sharp band between 60 and 70° (Fig. 35d). The distribution over varying spatial scales has not been mentioned

as the median of R exhibited no distinct scale-depending features and remained centered at all observed depths.

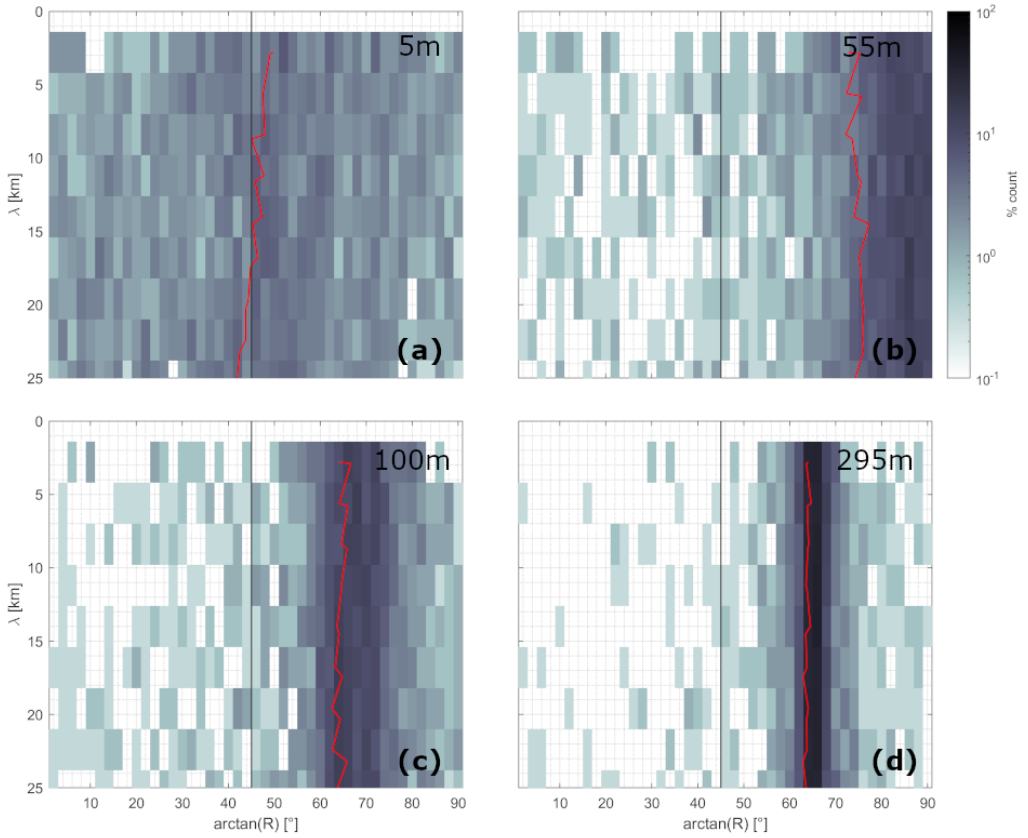

Figure 35. Same as Fig. 32 except for EQT1-1 at **(a)** 5 m, **(b)** 55 m, **(c)** 100 m, and **(d)** 295 m depth. The bin sizes along the y-axis equal the mean sampling interval of EQT1-1.

In the upwelling region offshore of the northwest African coast, the mixed layer again was characterized by a compensated density field at all scales (Fig. 36a). Around 50 m depth, at the MLD that is, the compensated field transitioned into a temperature dominated one with the median being at $\arctan(R) = 56°$ for $\lambda > 10$ km and at slightly higher values for smaller spatial scales (Fig. 36a) corresponding with a maximum in $k_{80\%}(z)$. Progressing in the water column, the distribution of R shifts back to a more compensated state with a centered median around 48° (Fig. 36c), which is maintained down to 350 m depth. The occurrence of salinity-driven variability got more sporadic as progressing along the water column (Fig. 36d).

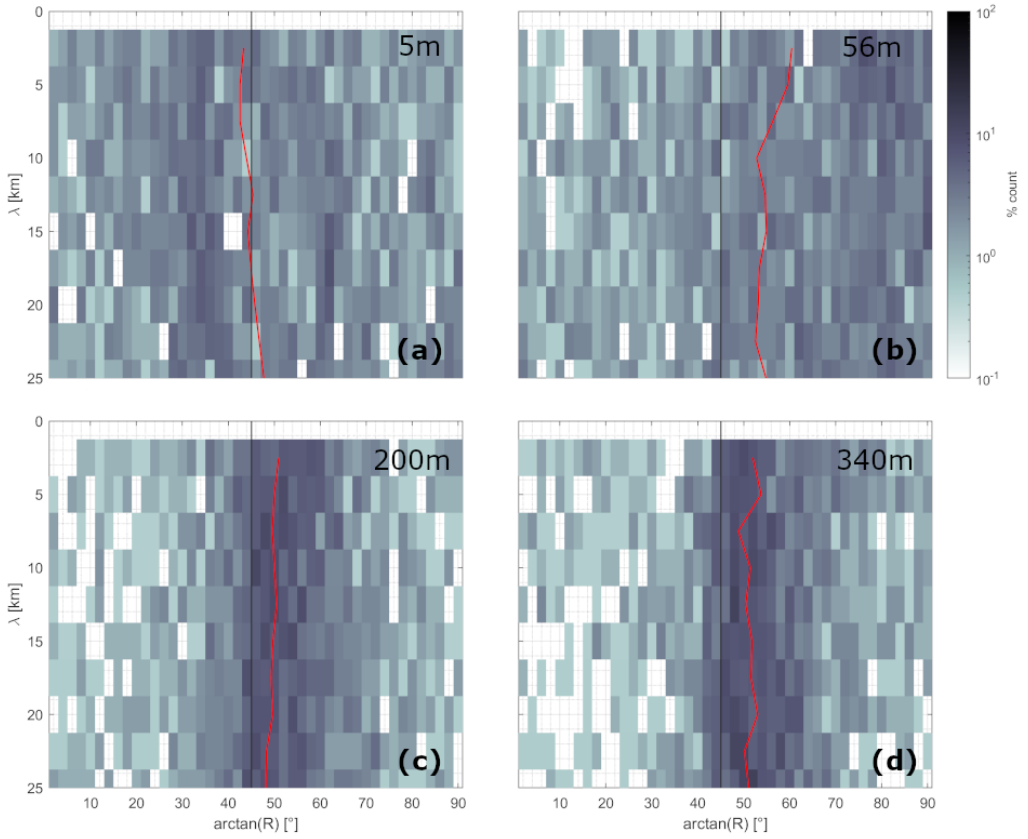

Figure 36. Same as Fig. 32 except for CVF1-1 at **(a)** 5 m, **(b)** 56 m, **(c)** 200 m, and **(d)** 340 m depth. The bin sizes along the y-axis equal the mean sampling interval of CVF1-1.

Lastly, the EGC is the only region which exhibited the transition from a distinct salinity- to a temperature-driven density field along the water column (Fig. 37). The upper water column down to 70 m depth was occupied by a salinity dominated density field (median R around 25° with no distinct scale sensitivity), as expected considering the presence of PSW and distinct freshwater anomalies associated with the retreating ice edge. Passing the cold and fresh core of the PSW, the density field progressively gets more compensated reaching $\arctan(R) = 45°$ for most scales at 130 m depth (Fig. 37b). For the lower water column, which was mostly occupied by AW, the TS contribution shifted toward temperature domination with a distinct scaling behaviour: As the observed length scale is increased the larger R gets coinciding with a minimum in $k_{99\%}(z)$ (cf. Fig. 27). Smaller-scale gradients remained near compensation while a maximum of around $\arctan(R) = 64°$ was found for the largest displayed scale. Thus, the AW layer density field was mainly structured my large-scale variability in temperature. Toward the lower boundary of the section, the median for $2 < \lambda < 10$ km developed a centered position close to 45° followed by a distinct temperature dominance for larger scales (Fig. 37d).

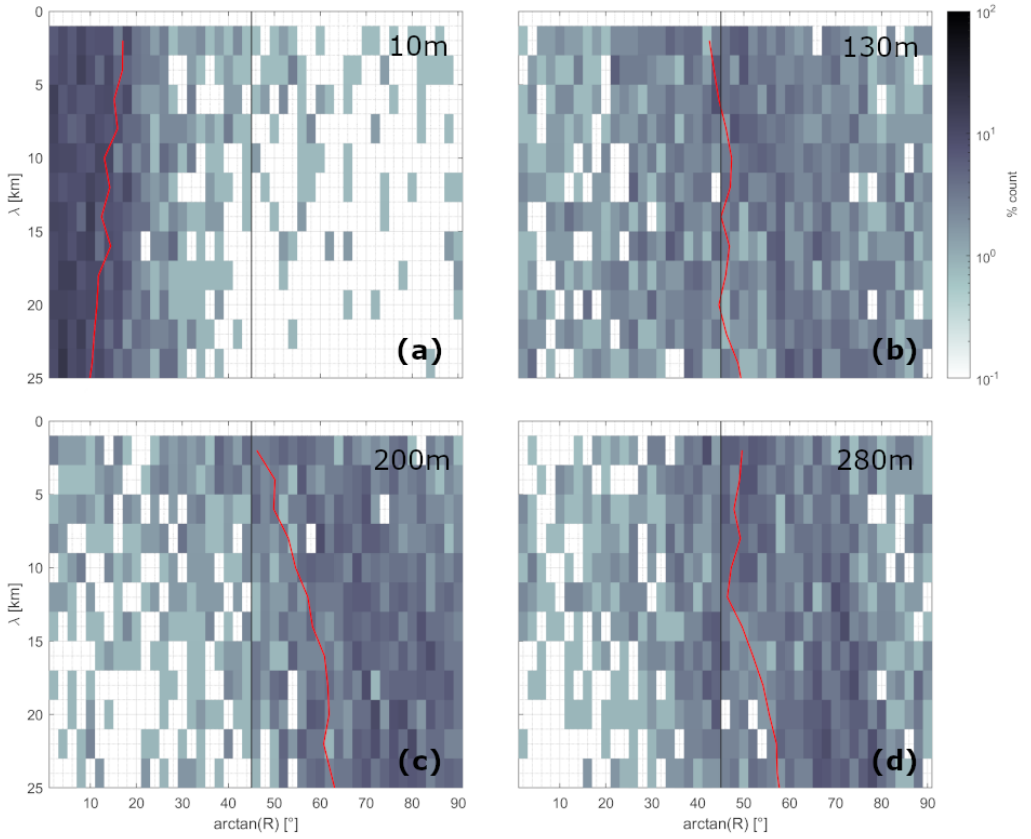

Figure 37. Same as Fig. 32 except for EGC1-1 at **(a)** 10 m, **(b)** 130 m, **(c)** 200 m, and **(d)** 280 m depth. The bin sizes along the y-axis equal the mean sampling interval of EGC1-1.

Taking EGC1-3 into account (Fig. 38), this flip in the TS contribution can indeed not be evaluated, yet it enabled a more detailed assessment of the scale-depending spread of the TS contribution within the PSW. Subsampling along EGC1-1 exhibited a rather uniform spread of R at all scales, while EGC1-3 revealed a distinct scale-sensitivity as shown by the median that varied around 10° and increases for $\lambda < 10$ km presumably contributing to low values in $k(z)$ (cf. Fig. 27). The salinity-driven density field appears to get less scale dependent at 24 m depth and at the lowermost measurements (Fig. 37b,d). Intermediately, between 25 and 39 m depth (Fig. 38c), the median line is characterized by an increasing tilt toward lower density ratios in agreement with the steepening of k as estimated for all percentage envelopes.

With the knowledge that the initial sampling spacing can impact the scale sensitivity of the R-ratio, it might be possible that the weak scaling behaviour as observed for the mid-latitude study areas is attributed to the relatively low horizontal resolution of the original signatures.

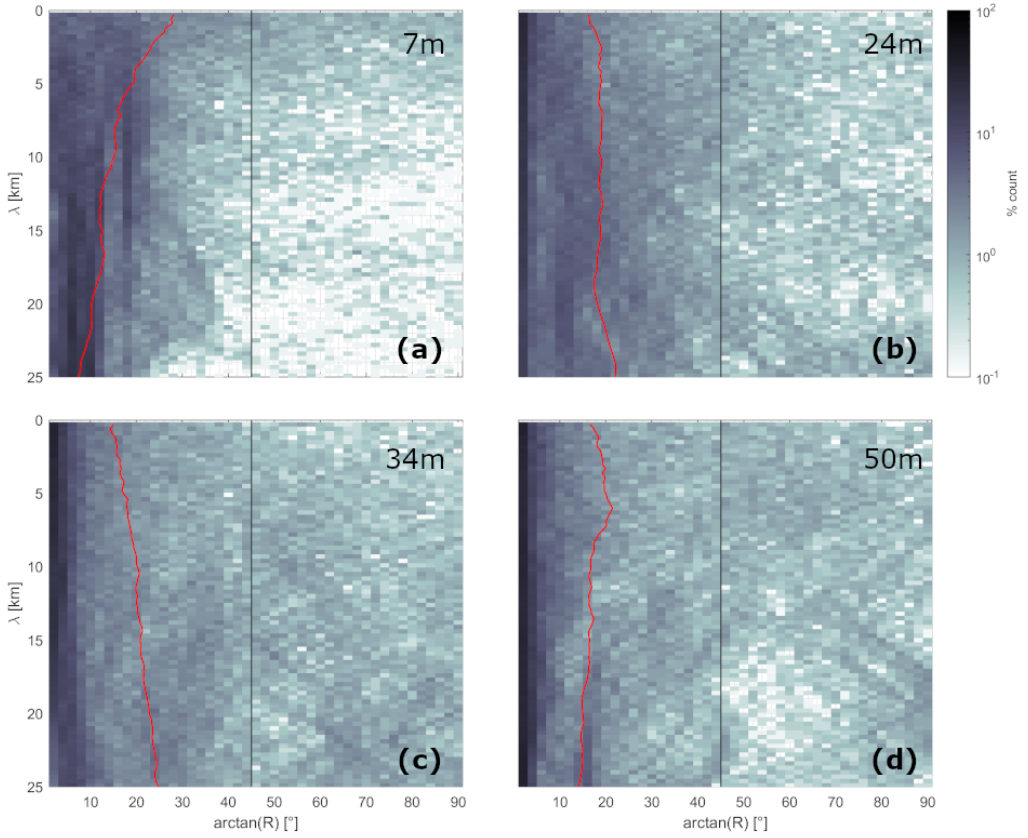

Figure 38. Same as Fig. 32 except for EGC1-3 at **(a)** 7 m, **(b)** 24 m, **(c)** 34 m, and **(d)** 50 m depth. The bin sizes along the y-axis equal the mean sampling interval of EGC1-3.

Chapter 4

Discussion

This thesis involves a multi-scale investigation of horizontal density gradients down to spatial scales beyond the submesoscale. High-resolution datasets have revealed distinct regional and global contrasts in the variability of the subsurface density field. The existing literature on the scale-sensitivity of lateral gradients is limited, yet we will discuss the following implications based upon our observations: Reduction and intensification of density gradients, data aliasing, scaling properties of density fronts, and patterns of thermohaline variability.

4.1 Density gradient reduction and intensification

4.1.1 Meteoric forcing

Previous assessments of horizontal density gradients over different spatial scales revealed significantly larger gradients in the tropical Atlantic (Coadou-Chaventon et al., pers. comm. 2024) than in the Antarctic MIZ (Swart et al., 2020). This clear segregation of the Southern Ocean from other oceanic areas is emphasized by the results presented in this study. The shift from warmer subtropical waters to colder Antarctic water occurs throughout a series of distinct transition zones - literally large lateral gradients, yet they are widely spaced presumably not masking the multi-scale spread of density gradients as observed across the EGC. What separates the Southern Ocean from the other areas is a stronger surface forcing, related to atmospheric transient storms with wind speeds exceeding $20\,\mathrm{m\,s^{-1}}$ (Yuan et al., 2009), which can erode the mixed layer stratification. Indeed, Swart et al. (2020) observed a distinct wind-front relationship using glider data, with higher wind stress ($>0.4\,\mathrm{N\,m^{-2}}$) resulting in a suppression of lateral density gradients to an average of $0.01\,\mathrm{kg\,m^{-3}\,km^{-1}}$. They proposed that this relationship might be driven by thermohaline shear dispersion. Moreover, Du Plessis et al. (2019) found that horizontal submesoscale fronts within the mixed layer are characterized by a distinct temperature-driven seasonality. In austral winter, only 3% of lateral buoyancy gradients exceed $10^{-7}\,\mathrm{s^{-2}}$, in summer, on the other hand, 13% do. They also addressed that wind forcing, depending on its orientation relative to a front, can weaken or

even enhance vertical stratification - this could, however, not be tested in the presented work due to the consideration of absolute density gradients only. The substantial gradient weakening in winter combined with the forcing associated with the westerly wind belt might explain the overall weak density gradients across the ACC.

4.1.2 Freshwater anomalies

Observations from ice-tethered profiler measurements in the Arctic Ocean's Canada Basin show the presence of horizontal density gradients under sea-ice down to scales of $\mathcal{O}(1\,\mathrm{km})$ (Timmermans et al., 2012). The authors attributed the presence of sea-ice and ice-ocean shear to alternations of dynamical processes in terms of frontogenesis and instabilities. Our evaluation of three regions in vicinity to the northern MIZ firmly points to sea-ice contributing to strong (near-)surface density gradients. In ice-free mid-latitude regions, horizontal density gradients are commonly, yet not universally, erased by effective vertical mixing. The sea-ice derived meltwater stratification as observed in the presented work and in recent Arctic studies (Hofmann et al., 2024; von Appen et al., 2021), however, prevents such gradient reduction by mixing which likely explains the persistence of surface density fronts down to the finescale. A highly stratified surface layer allows unique frontal structures like a stepwise subduction as introduced by Hofmann et al. (2024) that feature multiple layers of high gradient-richness . In the Chukchi Sea, Timmermans and Winsor (2013) report of the occurrence of surface density gradients inferring from a weak vertical mixing, but in ice free conditions, suggesting that other air-sea interactions exist that drive a high gradient richness at the surface. An explicit mechanism for the observed lateral density variability was not proposed. In general, it can be assumed that any freshwater anomaly, be it driven by sea-ice melting, river runoff or net precipitation, might be characterized by strong lateral density gradients.

4.1.3 MLD

Swart et al. (2020) proposed that shallow mixed layer environments such as the Polar regions are more likely requiring high-resolution sampling due to their distinct scale-dependant spread of lateral density gradients. Considering our observations from the salinity dominated regimes, that is the northern polar areas with no identifiable ML and the ACC with the deepest ML, this idea appears to be valid. Yet, the global analysis shows that regions within the tropical circles also feature a wide span of density gradients with a pronounced scale dependence suggesting that the MLD might only be one of many relevant factors highlighting the requirement of high-resolution data to capture the full variability of the density field. Based upon

our results, a combination of a distinct decay rate and a high strength of gradients attributes to the susceptibility to a lateral gradient underestimation. Layers with meltwater driven salinity anomalies fitted this profile. Using a similar parametrization, Coadou-Chaventon et al. (pers. comm. 2024) demonstrated that a salinity anomaly such as a Amazon freshwater plume is not only characterized by a high magnitude of density gradients, but also by a gradient drop-off as early as around $\lambda \approx 3\,\mathrm{km}$. The parametrization used in this thesis demonstrated that this gradient decline can be assumed as a generally valid characteristic for $(\nabla\rho, \lambda)$-distributions, yet it is not suited to identify characteristic length scales of sharp drop-offs.

Concerning the role of the mixed layer for the obtained results, our observations indicate distinct scale-dependant characteristics of the density field between the ML and the stratified subsurface. In the subtropical gyre of the North Pacific Rudnick and Ferrari (1999) find that variability in the density field of the ML is restricted to 10 km, while Hosegood et al. (2006) find that density variability exists down to scales of 2 km in the same region. For the equatorial Atlantic, the CVFZ, and the ACC we indeed find a pronounced tendency for the occurrence of compensated density gradients within the MLs, presumambly due to vertical mixing processes and selective removal of density gradients by submesoscale dynamics. Yet, we also found lateral gradients being present down to the finescale, yet they could have been extremely short-living and might have eroded right after being crossed by the towed system. The evaluation of this aspect could not be performed with the data used. There is, however, no universal length scale threshold for an uncompensated density field, hence our observations of smaller scale ML fronts do not stand in contrast to the rather niche literature. In the north-eastern subtropical Atlantic Kolodziejczyk et al. (2015) find surface compensation at all scales during boreal winter (Feb-Mar) and a shift toward salinity-driven density variability in the mesoscale in summer (Aug-Sep). They considered summer heating and reduced vertical mixing of the upper ocean as the main contributors for breakdown of density compensation down to the submesoscale. Our findings from closely located data obtained in the CVFZ do not indicate large-scale shifts of the *T*-*S* contribution, which might be attributed to the data being acquired in the spring season.

To add a level of complexity, the observed MLs show slightly varying magnitudes of density gradients, albeit all are very weak, in accordance that greater MLDs, which can be used as a measure for high mixing strength, lead to a greater tendency for lateral compensation (Rudnick & Martin, 2002). They find that global deep MLDs exceeding 75 m distinguish clearly from moderate MLDs (25-75 m) in terms of the richness of their density field and that compensation is not typical for very shallow MLDs.

4.2 Data aliasing

The computation of density gradients from along-track observations are accompanied by a spatial and temporal component. Actual snapshots in time assuring that variability in the density field is spatially driven can only be obtained by numerical models. Simulations based upon primitive numerical equations usually do not resolve scales of $\mathcal{O}(1-100\,\mathrm{m})$ and simulations that indeed can even have $\mathcal{O}(1\,\mathrm{m})$, such as direct numerical or large eddy simulations, cannot resolve more than four orders of magnitude (i.e. they do not resolve scales larger than $\sim$10 km). The choice of method for the data acquisition can determine the influence of temporal variability on the recorded hydrography.

Traditional CTD sections, especially when covering deep parts of the water column, lack an adequate spatiotemporal resolution to assess the development of submesoscale activities (e.g. Duong, 2021). Our results show that highly stratified layers feature strong density gradients and common phenomena propagating along such density boundaries are internal gravity waves. Their phase velocity can span values between tens of cm/s and several m/s: In Fram Strait and over the Yermak Plateau phase velocities of around 0.3 and 0.8 m/s, respectively, were found (Kozlov & Mikhaylichenko, 2023) and Sun et al. (2021) even observed large internal waves with propagation velocities of 3.27 m/s in the Andaman Sea, albeit in deep water. Their wavelength and period typically vary between hundreds of meters to tens of kilometers, and between minutes and hours, respectively (Njoku, 2014). A lowering of the temporal resolution and acquisition speed can lead to the occurrence of aliasing, which can distort the density signature. With acquisition speeds between 3.5 and 4.2 m/s, we suggest that the towed undulated data presented here avoided internal wave aliasing for the most part. If the upper limit of the internal wave spectrum had been determined, one could have used the Nyquist frequency of the data sampling for a direct comparison (cf. Timmermans et al., 2012). In general, temporal resolution of 1/24 s for the constant depth tows, resolving fine-scale variability, and of $\mathcal{O}(1-10\,\mathrm{min})$ for the undulating tows, resolving submesoscale variability, were high enough to consider that temporally induced variability was low. Wind-propelled sailbuoys as utilized by Swart et al. (2020) and Coadou-Chaventon et al. (pers. comm. 2024) exhibited a comparable temporal sampling resolution, but slightly lower mean propagation speeds between 1 m/s and 3 m/s. Parallel sailbuoy tracks in the study of the latter provided direct insights into the temporal variability. They found that the dominant feature remained consistent for $\mathcal{O}(2-10\,\mathrm{h})$ and suggested that temporal induced signature variability is little. However, smaller-scale less dominant processes might develop and propagate on even shorter timescales. These processes should especially be considered within the ML that lacks the stratification for internal waves to propagate. As gradients cannot be assigned to a single structuring process, it remains

unresolved to which extent data aliasing might transfer to the estimated gradient field.

4.3 Scaling properties of lateral density variability

4.3.1 Sub-ranges

A common way to statistically quantify energetically different dynamical regimes is the estimation of KE spectra. They typically follow a power law, whereby the exponent (or spectral slope) is associated with ocean dynamics of different length scales. For example, a slope of -3 is predicted by theoretical quasi-geostrophic turbulence (Charney, 1971). At the mesoscale, the spectra are expected to flatten down to -2 in the presence of submesoscale energy (Callies & Ferrari, 2013) and further down to the Kolmogorov-slope of -5/3 given by surface quasi-geostrophic theory. Theoretical frameworks for the transition towards the Kolomogorov-slope rely on a forward energy cascade (from large to small scales), due to the non-linear interactions between internal gravity waves (Lindborg, 2006). As horizontal density gradients represent stored potential energy (Mahadevan et al., 2012), providing the restoring force for baroclinic motions, a motivating hypothesis was that physical processes acting on different scales can be attributed to alternating characteristics of the gradient distribution for different sub-ranges of λ allowing the identification of dominating scales similar to the KE spectra. Data obtained upstream of the EGC at 30 m depth reveals a flattening of density gradients for the submeso- and finescales which might correspond to the length scale at which gradient-driving processes dominate. It could also point toward a baseline at which the density gradients get resolved, and therefore, stop to rise for smaller scales. However, the rest of the datasets show that the decay rate of lateral density gradients is scale-invariant for all observed sampling frequencies. One could speculate that the exhibition of a consistent scaling law might indicate that the different regimes are not well-separated in the region analyzed or that a particular process is present masking all other structuring dynamics. A clear explanation could not be found based upon our observations only.

On the other hand, the complementing quantity $D(z)$ reveals different distinct values for different sub-ranges of scales concurring with the assumption that the fractal dimension depends on the spectral characteristics exhibited by the system being analyzed (Wijesekera, 1996).

4.3.2 Predictability of fine-scale $(\nabla\rho, \lambda)$-distributions

We found tendencies for a scale-based underestimation of density gradients in all study regions. Layers characterized by high density variability such as the base

of shallow MLs, frontal systems, eddies, and subsurface currents were prone for an incomplete depiction on their thermohaline structure. We showed that $k(z)$ and $a(z)$ do not scale proportionally, contributing to varying susceptibilities throughout distinct gradient fields: We found that meltwater layers exhibited high values in both parameters, while the EUC came with high strength in gradients yet a lower decay rate as the length scale is increased.

Based upon similar findings Swart et al. (2020) emphasized the requirement of high-resolution data in order to capture an adequate variance of the density field obviating gradient underestimations, especially at high latitudes. Numerical models demonstrated that finer horizontal resolutions indeed lead to sharper density gradients (Kjellsson & Zanna, 2017) and that unresolved scales can contribute to uncertainties in large-scale density gradients (Brankart, 2013). However, the acquisition of differently resolved data across the EGC demonstrate matching gradient distributions over various lateral spatial scales, suggesting that absolute fine-scale variations in the density field could possibly be predicted by measurements with a coarser sampling interval. This is attributed to the joint distributions strictly following the scaling law. Undulating measurements come with a trade-off between the vertically covered area of the water column and the horizontal spacing between consecutive profiles. Being able to estimate the gradient distribution for scales that are actually not resolved, would revoke the need of constant depth tows and thereby the sacrifice of hydrographic information in the vertical. Note that the predictability regards the absolute gradients without considering the position or direction and not the reconstruction of the original density signature, which would obviously benefit from a dense profile spacing. Moreover, some sort of threshold in the lateral sampling frequency is to be expected to make a dependable prediction as the best-fit parameters come with large uncertainties for a distribution consisting of only a few data pairs. We suggest that a sampling interval $< R_\mathrm{d}$ might be sufficient.

Regarding the sample direction, it should be noted that all gradients shown are along-track gradients. They are not necessarily across-front, and therefore, the actual absolute values of the gradients are most likely underestimated by the presented routine. An array of transects would have allowed an estimation of the front directions and thereby the assessment of the difference from the direction of the along-track gradients. The degree of the gradient underestimation attributed to the sample direction could not be evaluated in this work.

4.3.3 Anisotropic density fields

A similar parametrization technique for joint gradient/length scale distributions was independently developed and applied by Coadou-Chaventon et al. (pers. comm. 2024). Based upon an exponential 99-envelope fit, they regionally compared

the multi-scale spread of density gradients for different locations in the tropical Atlantic. Our results, however, reveal that a distinct feature in the density signature can mask other variabilities leading to multi-modal patterns between gradients and lateral scales. In a rather isotropic density field this might be less of a problem, yet we highly suggest to consider lower percentiles as well in order to capture a more representative picture of the gradient distribution at all scales and to enhance robustness and validity when comparing density field variability over various length scales. Moreover, our results demonstrate that varying percentiles do not necessarily share the same characteristics.

4.4 Temperature and salinity contribution

4.4.1 Patterns of thermohaline variability

Oceanic areas are conceptually categorized in alpha and beta oceans depending on the property governing the vertical stratification (Carmack, 2007). Our findings suggest that the distribution of alpha, beta, and transition zone oceans as described by Stewart and Haine (2016) coincide with regions with corresponding *T-S* variances of the lateral density field. This might be explained by the fact that density gradients form a vector field with a vertical and horizontal component. As isopycnals are tilted, usually not perfectly vertically or horizontally aligned, they result in density gradients for both directions in space. Studying the global pattern of horizontal salinity variability Drushka et al. (2019) found that high latitudes, generally considered beta oceans, are indeed characterized by submesoscale lateral salinity-driven density variability. Deeper topAWI sections also allowed to assess the T-S contributions down to the ocean interior: We found that the ACC holds a compensated density field from the surface down to 300 m in accordance that it remains a transition zone ocean at least down to 100 m depth (Stewart & Haine, 2016).

4.4.2 Turner angle

The computation of Tu by performing a four-quadrant arctangent returns angles between -180° and 180° and allows to make statements on double-diffusive potential (You, 2002): -90° < Tu < -45° indicate the possibility for "stair-case" double-diffusion, for -45° < Tu < 45° the water column is stably stratified in temperature and salinity, and values between 45° < Tu < 90° are associated with "salt-fingering" double-diffusion. Angles beyond $\pm 90°$ are expected for gravitational instability in the water column (Ruddick, 1983).

In contrast, this work utilized the relation between Tu and the density ratio R_ρ, which is defined by an arctagent taking one input only (see eq. 4), and therefore,

it is limited to two quadrants. As a consequence, signs of temperature and salinity variability (for instance, if both are positive or both are negative) can not be distinguished mapping the quadrant for angles with some ambiguity. The use of a two-argument arctangent might give a more accurate representation of the thermohaline structure in a two-dimensional space. However, note that the different regimes of stability are actually applied for vertical temperature and salinity profiles and that the Turner angle for horizontal variability is shifted by 45° for reasons of differentations (Tippins & Tomczak, 2003). It is unclear to what extent the physical interpretations after Ruddick (1983), who introduced the Turner angle as a way to investigate double-diffusive potential, can be applied for lateral density variability. Moreover, we addressed absolute values of lateral density gradients only, for which reason Tu is reduced to a single quadrant and exclusively bounded to positive values regarding ∇T and ∇S. Hence, the ambiguous angle signs that come with an one-argument arctangent is not of concern. For the sole purpose of evaluating the temperature and salinity contribution for along-track density fronts, we suggest the one-argument arctangent is sufficient.

Chapter 5

Summary and Conclusions

The principal aim of this thesis was to assess the sensitivity of lateral density gradients to the spatial scale and to contrast regions as different as Fram Strait, the equatorial and tropical Atlantic, and the Southern Ocean in terms of the multi-scale variability of their near- and subsurface density fields. For this purpose, we utilized topAWI data with horizontal resolutions resolving the submeso- and finescale and developed a statistical pipeline that can create and qualitatively compare a bulk of density gradient/length scale distributions.

We observe a non-linear decline of density gradients with an incrementally increased lateral length scale for more than 3000 density signatures (data series at distinct depth layers) in accordance with Swart et al. (2020) whose analysis of $\nabla_\rho(\lambda)$ simply by subsampling laid the basis for our method. We expanded this underlying concept by a parametrization enabling to study the overall strength of density gradients and their decay rate when the spatial scale is incrementally increased. The former can directly be assigned to region-specific hydrography structures, if they span multiple depths or prevail over other features at the same depth, e.g. freshwater plumes, subsurface currents, and density fronts. On the contrary, the qualitative progression and global differences of the decay rate seems less intuitive, yet it is closely related to the fractal dimension and peaks when the density ratio R holds scale-dependant characteristics as revealed in this work. For constant depth tows, the presented subsampling method can reliably be applied to describe the spread of density gradient from the 99th- down to the 10th-percentile. The consideration of the inner envelopes is necessary as individual features in the density signature can mask other variabilities leading to a multi-modal pattern between gradients and lateral scales. We find that the percentiles in the $(\nabla\rho,\lambda)$-distributions that can be assessed with a sufficient statistical significance get restricted to outer envelopes for datasets containing a low number of sampling points. Moreover, multiple occupations across the EGC with different horizontal sampling intervals show that a lower horizontal resolution contributes to a loss of information in the density signature and in the gradient distribution. Yet, we compute coinciding values for $a(z)$ and $k(z)$ between tows of 1900 m, 300 m, and 2.3 m spaced casts indicating that absolute fine-scale variations in the density field can be estimated from the spread of

gradients over coarser spatial scales.

Study areas in the northern Polar region are under the influence of the MIZ involving sea-ice derived meltwater stratification of the (near-)surface layers. These feature strong salinity-driven density gradients and a scale-invariate, self-similar density field as observed in northern Fram Strait. Within the EGC cold and fresh PSW gets subducted by less stratified water from the Greenland Sea associated with a relocation of the regime abundant in small-scale gradient to subsurface depths. In central Fram Strait, we observe two levels of high lateral density variability corresponding to a submesoscale frontal system involving a step-wise subduction.

The horizontal density field in mid-latitude regions is temperature-driven. In the equatorial Atlantic and the Cape Verde Frontal Zone we find a ML more typical of the open ocean, in which density gradients are particularly weak and low in small-scale fluctuations. The tendency of a density compensated ML increases with the mean position of its base, which has also been proposed in Rudnick and Martin (2002). As the lower boundary of a ML is approached the scale-sensitivity and the overall magnitude of lateral density gradients increases drastically. The EUC that acts as a net eastward transport of salinity features a gradient richness comparable to the ones driven by sea-ice melt. However, its self-similar geometric properties are not distinguishable from the ocean interior, which, in general, is occupied by an increasingly compensated gradient field with depth, eventually holding similarly weak density gradients as the corresponding ML.

The ACC stands out with an especially deep winter-time ML throughout its multi-front structures and holds the overall weakest density gradients and lowest amount of small-scale fluctuations. Variability of its gradient field with depth is weak compared to the other regions.

All in all, the presented subsampling routine was developed, inter alia, to test the hypothesis that different oceanic regimes are distinguishable by the gradient distribution in their density fields and this study indeed brought distinct contrasts to light. The selection of regions provided comparisons beyond a regional context, yet their line-up is rather arbitrary and deficient in terms of a global analysis. Regional differences in the Arctic region are addressed in detail revealing they are small as opposed to differences to the other latitudes. In order to exploit more potential of the presented subsampling routine, one could upscale its application on data covering wider areas of the world's ocean. Submesoscale resolving datasets of multiple depth layers might not be available on a global scale, which is why one could switch to surface thermosalinograph data typically obtained during a cruise, and hence spanning large areas. Any data with a high spatio-temporal resolution that are obtained over a longer lateral along-track distance might be suited for the routine to be applied on adding new context on the global variability of density

gradients. For instance, towed instrument arrays (see Kock et al., 2023) could provide a similar horizontal resolution as the topAWI operated with a constant depth pattern while also providing information along different depth layers.

In general, to achieve clearer comparisons, distinct horizontal regimes (e.g. the MIZ and the open sea) should be analyzed separately. Yet, such additional split of the topAWI sections was not performed in this thesis due to the uneven occupations of different regimes, which would have lead to at least one very short sub-track presumably containing a number of sampling points too low for our multi-scale routine to work properly. The inspection of relative gradient occurrence and the parametrization of lower percentiles helped in identifying the presence of regimes along the same section with different gradient fields. The concrete assignment, of a set of density gradients to one of such regime was, however, not possible.

Further potential of the statistical pipeline can be explored by exploiting the full extent of the topAWI data that are already available: as an attempt to support interpretations and speculation of this thesis, one might execute our multi-scale routine on thermohaline and velocity data. The latter is of particular interest, especially in dynamic regions with a complex flow field (e.g. the equatorial and ACC crossings.) Assessing the scale dependence of horizontal gradients in the ocean is, however, not restricted to physical properties only. Considering fluorescence and oxygen gradients, which can also be estimated from all topAWI operations, would enable an interdisciplinary study and the assessment of potential linkages of density gradients to biogeochemical properties at varying spatial scales. Other data that might help consolidating and validating the results of this thesis are wind speed data as the strength of the wind field has been considered as a potential contributor for the different degrees of compensation in the density fields.

Fram Strait will again be explored with the help of the Triaxus in the upcoming time. If horizontal gradients and their distribution over various depths are still of interest, it is recommended to keep the spacing between consecutive upcasts on a reasonable level (e.g. 300 m to maintain consistency with the EGC sections) that ensures sufficient vertical information and a high number of sampling points per depth ensureing a robust functionality of the subsampling method. The results demonstrated that the conduction of constant depth tows is not necessary.

In recent years, submesoscale dynamics has become a major study focus in oceanic sciences, and thus, horizontal density gradients have increasingly been used as thresholds for fronts and other surface structures. With the knowledge we gained from this study, such pre-defined thresholds come with a degree of arbitrariness - whether they get exceeded by the observations will depend on how fine the dataset is resolved. It is obvious that a submesoscale front must not be identified by a fine- or mesoscale gradient, yet a shift of λ by a few hundred meters

can already have a significant impact on the gradient. In order to make gradient-thresholding more consistent, the mere mention of the lateral scale over which a gradient threshold is defined or used could already help.

The introduction of the new statistical parameters $a(z)$ and $k(z)$ created new opportunities for the study of lateral density variability in the ocean. Complementing computations helped in getting a deeper understanding of them, yet in what combination they occur along the water column of the study regions remains rather unintuitive. For future related studies it might be useful to consult further quantities: The estimate of spectral slopes is a common tool to quantify turbulence characterizations and could be used to investigate the impact of the observed density gradients on the energy distribution. Alternatively, the sub-sampling part of our routine can be recycled for the computation of the correlation length scale, which essentially quantifies how far apart in space two points in the ocean can be while still having correlated density values, potentially allowing the identification of patterns in the density gradient field.

Overall, this thesis involves a simple, yet new, statistical methodology tested on high-resolution observational data. New knowledge is added to the scaling behaviour of lateral density gradients in the upper ocean, which has been barely addressed in previous literature. Our observations laid a solid foundation for future studies regarding this topic and the possibilities for a continuation are broad.

Acknowledgements

Ship time was provided under grant numbers AWI_PS113_00 (PS113), AWI_PS131_07 (PS131), and AWI_PS133/1_02 (PS133.1) of RV Polarstern and GPF 18-1_33 (MSM93) of RV Maria S. Merian.

The Triaxus CTD data that this thesis is based on are available on PANGAEA (see Hofmann et al., 2022; von Appen, Hölemann, et al., 2023; von Appen, Kanzow, et al., 2023; von Appen et al., 2019).

I would like to express my sincere gratitude to my supervisor *Dr. Wilken-Jon von Appen*, for his invaluable guidance, feedback, and support throughout my research, for showing understanding and empathy for personal obstacles I went through, and for the opportunity to take part on a wonderful expedition with RV Polarstern.

A special note of thanks to *Prof. Dr. Thorsten Kanzow*, who welcomed me at the section of physical oceanography of AWI.

Genuine thanks to *Dr. Thomas Badewien* for stepping in for *Prof. Dr. Jörg-Olaf Wolff* at rather short notice accepting to co-examine this thesis, and for his constructive feedback.

Furthermore, I would like to thank the OZE group of Wilken consisting of *Hauke Becker*, *Dr. Rebecca McPherson*, *Simon Reifenberg*, *Carina Engicht*, *Ryan Mole*, and *Zerlina Hofmann* for sharing interesting insights from their work, for the helpful discussions, and for the positive environment in the office as well as on the vessel.

Additionally, I thank *Prof. Dr. Sebastiaan Swart* and *Solange Coadou-Chaventon* for sharing their expertise on scale-depending analysis of hydrographic properties. This work certainly benefited from their input.

Finally, my appreciation goes out to my *mother*, my *little brother*, and my *closest friends* for their wholehearted support and their unwavering believe in my journey and success.

References

Beszczynska-Möller, A., Fahrbach, E., Schauer, U., & Hansen, E. (2012). Variability in atlantic water temperature and transport at the entrance to the arctic ocean, 1997–2010. *ICES Journal of Marine Science*, *69*(5), 852–863. https://doi.org/10.1093/icesjms/fss056

Blanke, B., Arhan, M., Lazar, A., & Prévost, G. (2002). A lagrangian numerical investigation of the origins and fates of the salinity maximum water in the atlantic. *Journal of Geophysical Research: Oceans*, *107*(C10), 27–1. https://doi.org/10.1029/2002JC001318

Boccaletti, G., Ferrari, R., & Fox-Kemper, B. (2007). Mixed layer instabilities and restratification. *Journal of Physical Oceanography*, *37*(9), 2228–2250. https://doi.org/10.1175/JPO3101.1

Botnikov, V. (1963). Geographical position of the antarctic convergence zone in the antarctic ocean. *Soviet Antarctic Exped. Inform. Bull.*, *41*, 324–327.

Boyd, T. J., & D'Asaro, E. A. (1994). Cooling of the west spitsbergen current: Wintertime observations west of svalbard. *Journal of Geophysical Research: Oceans*, *99*(C11), 22597–22618. https://doi.org/doi.org/10.1029/94JC01824

Brankart, J.-M. (2013). Impact of uncertainties in the horizontal density gradient upon low resolution global ocean modelling. *Ocean Modelling*, *66*, 64–76. https://doi.org/10.1016/j.ocemod.2013.02.004

Brenner, S., Rainville, L., Thomson, J., & Lee, C. (2020). The evolution of a shallow front in the arctic marginal ice zone. *Elem Sci Anth*, *8*, 17. https://doi.org/10.1525/elementa.413

Callies, J., & Ferrari, R. (2013). Interpreting energy and tracer spectra of upper-ocean turbulence in the submesoscale range (1–200 km). *Journal of Physical Oceanography*, *43*(11), 2456–2474. https://doi.org/10.1175/JPO-D-13-063.1

Carmack, E. C. (2007). The alpha/beta ocean distinction: A perspective on freshwater fluxes, convection, nutrients and productivity in high-latitude seas. *Deep Sea Research Part II: Topical Studies in Oceanography*, *54*(23-26), 2578–2598. https://doi.org/10.1016/j.dsr2.2007.08.018

Chapman, C. C., Lea, M.-A., Meyer, A., Sallée, J.-B., & Hindell, M. (2020). Defining southern ocean fronts and their influence on biological and physical processes in a changing climate. *Nature Climate Change*, *10*(3), 209–219. https://doi.org/10.1038/s41558-020-0705-4

Charney, J. G. (1971). Geostrophic turbulence. *Journal of the Atmospheric Sciences*, *28*(6), 1087–1095.

Chavez, F. P., & Messié, M. (2009). A comparison of eastern boundary upwelling ecosystems. *Progress in Oceanography*, *83*(1-4), 80–96. https://doi.org/10.1016/j.pocean.2009.07.032

Chelton, D. B., DeSzoeke, R. A., Schlax, M. G., El Naggar, K., & Siwertz, N. (1998). Geographical variability of the first baroclinic rossby radius of deformation. *Journal of Physical Oceanography*, *28*(3), 433–460.

Chelton, D. B., Schlax, M. G., & Samelson, R. M. (2011). Global observations of nonlinear mesoscale eddies. *Progress in oceanography*, *91*(2), 167–216. https://doi.org/10.1016/j.pocean.2011.01.002

Chu, P. C., & Fan, C. (2011). Determination of ocean mixed layer depth from profile data. *Prcdgs15th Symp Int Obs Ass Sys Atmos, Ocn Lnd Sfc, AMS*, 1001–1008.

Crochiere, R. E., & Rabiner, L. R. (1983). *Multirate digital signal processing* (Vol. 18). Prentice-hall Englewood Cliffs, NJ.

Dietrich, G., Kalle, K., Krauss, W., & Siedler, G. (1975). *Allgemeine meereskunde: Eine einführung in die ozeanographie*. Gebr. Borntraeger.

Drushka, K., Asher, W. E., Sprintall, J., Gille, S. T., & Hoang, C. (2019). Global patterns of submesoscale surface salinity variability. *Journal of Physical Oceanography*, *49*(7), 1669–1685. https://doi.org/10.1175/JPO-D-19-0018.1

Du Plessis, M., Swart, S., Ansorge, I. J., Mahadevan, A., & Thompson, A. F. (2019). Southern ocean seasonal restratification delayed by submesoscale wind–front interactions. *Journal of Physical Oceanography*, *49*(4), 1035–1053. https://doi.org/10.1175/JPO-D-18-0136.1

Duong, B. L. (2021). Identification of fronts near the marginal ice zone (bachelor thesis). *University of Bremen, IUP, Department of Physical Oceanography*.

Eden, C., Czeschel, L., & Olbers, D. (2014). Toward energetically consistent ocean models. *Journal of Physical Oceanography*, *44*(12), 3160–3184. https://doi.org/https://doi.org/10.1175/JPO-D-13-0260.1

Ferrari, R., & Wunsch, C. (2009). Ocean circulation kinetic energy: Reservoirs, sources, and sinks. *Annual Review of Fluid Mechanics*, *41*, 253–282. https://doi.org/10.1146/annurev.fluid.40.111406.102139

Ferrari, R., & Young, W. (1997). On the development of thermohaline correlations as a result of nonlinear diffusive parameterizations. *Journal of marine research*, *55*(6), 1069–1101.

GEBCO Compilation Group. (2021). Gebco 2021 grid. https://doi.org/10.5285/c6612cbe-50b3-0cff-e053-6c86abc09f8f

Hattermann, T., Isachsen, P. E., von Appen, W.-J., Albretsen, J., & Sundfjord, A. (2016). Eddy-driven recirculation of atlantic water in fram strait. *Geophysical Research Letters*, *43*(7), 3406–3414. https://doi.org/10.1002/2016GL068323

Håvik, L., Pickart, R., Våge, K., Torres, D., Thurnherr, A., Beszczynska-Möller, A., Walczowski, W., & von Appen, W.-J. (2017). Evolution of the east greenland current from fram strait to denmark strait: Synoptic measurements from summer 2012. *Journal of Geophysical Research: Oceans*, *122*(3), 1974–1994. https://doi.org/10.1002/2016JC012228

Hofmann, Z., von Appen, W.-J., Mathieu, L., Hagemann, J., Engicht, C., Kuhlmey, D., & Becker, H. (2022). Physical Oceanography measured with CTD on Triaxus topAWI (towed ocean profiler of the AWI) during MERIAN cruise MSM93. https://doi.org/10.1594/PANGAEA.940010

Hofmann, Z., von Appen, W.-J., Kanzow, T., Becker, H., Hagemann, J., Hufnagel, L., & Iversen, M. H. (2024). Stepwise subduction observed at a front in the marginal ice zone in fram strait. *Journal of Geophysical Research: Oceans*, *129*(5), e2023JC020641. https://doi.org/10.1029/2023JC020641

Hofmann, Z., von Appen, W.-J., & Wekerle, C. (2021). Seasonal and mesoscale variability of the two atlantic water recirculation pathways in fram strait. *Journal of Geophysical Research: Oceans*, *126*(7), e2020JC017057. https://doi.org/10.1029/2020JC017057

Hosegood, P., Gregg, M. C., & Alford, M. H. (2006). Sub-mesoscale lateral density structure in the oceanic surface mixed layer. *Geophysical Research Letters*, *33*(22). https://doi.org/10.1029/2006GL026797

Hosegood, P., Nightingale, P., Rees, A., Widdicombe, C., Woodward, E., Clark, D., & Torres, R. (2017). Nutrient pumping by submesoscale circulations in the mauritanian upwelling system. *Progress in oceanography*, *159*, 223–236. https://doi.org/10.1016/j.pocean.2017.10.004

Hoskins, B. J., & Bretherton, F. P. (1972). Atmospheric frontogenesis models: Mathematical formulation and solution. *Journal of the atmospheric sciences*, *29*(1), 11–37. https://doi.org/10.1175/15200469(1972)029%3C0011:AFMMFA%3E2.0.CO;2

Jinadasa, S., Lozovatsky, I., Planella-Morató, J., Nash, J. D., MacKinnon, J. A., Lucas, A. J., Wijesekera, H. W., & Fernando, H. J. (2016). Ocean turbulence and mixing around sri lanka and in adjacent waters of the northern bay of bengal. *Oceanography*, *29*(2), 170–179. https://doi.org/10.5670/oceanog.2016.49

Johnson, G. C., Schmidtko, S., & Lyman, J. M. (2012). Relative contributions of temperature and salinity to seasonal mixed layer density changes and horizontal density gradients. *Journal of Geophysical Research: Oceans*, *117*(C4). https://doi.org/10.1029/2011JC007651

Johnson, L., Lee, C. M., D'Asaro, E. A., Thomas, L., & Shcherbina, A. (2020). Restratification at a california current upwelling front. part i: Observations. *Journal of Physical Oceanography*, *50*(5), 1455–1472. https://doi.org/10.1175/JPO-D-19-0203.1

Kjellsson, J., & Zanna, L. (2017). The impact of horizontal resolution on energy transfers in global ocean models. *Fluids*, *2*(3), 45. https://doi.org/10.3390/fluids2030045

Kock, T., Baschek, B., Wobbe, F., Heineke, M., Riethmueller, R., Deschner, S. C., Seidel, G., & Calil, P. H. (2023). An advanced towed ctd chain for physical-biological high resolution in situ upper ocean measurements. *Frontiers in Marine Science*, *10*, 1183061. https://doi.org/10.3389/fmars.2023.1183061

Kolodziejczyk, N., Reverdin, G., Boutin, J., & Hernandez, O. (2015). Observation of the surface horizontal thermohaline variability at mesoscale to submesoscale in the north-eastern subtropical atlantic ocean. *Journal of Geophysical Research: Oceans*, *120*(4), 2588–2600. https://doi.org/10.1002/2014JC010455

Kozlov, I., & Mikhaylichenko, T. (2023). Deriving internal wave phase speed in the arctic ocean from sequential spaceborne sar observations. *The International Archives of the Photogrammetry, Remote Sensing and Spatial Information Sciences*, *48*, 169–174. https://doi.org/10.5194/isprs-archives-XLVIII-M-1-2023-169-2023

Lindborg, E. (2006). The energy cascade in a strongly stratified fluid. *Journal of Fluid Mechanics*, *550*, 207–242. https://doi.org/10.1017/S0022112005008128

Liu, Y., Wang, J., Han, G., Lin, X., Yang, G., & Ji, Q. (2022). Spatio-temporal analysis of east greenland polar front. *Frontiers in Marine Science*, *9*, 943457. https://doi.org/10.3389/fmars.2022.943457

MacArtney Underwater Technology. (2019). *Triaxus - oceanographic rotv system. 2nd edition - 2.1*. Retrieved March 1, 2024, from https://www.macartney.com/media/6445/triaxus.pdf

MacKinnon, J. A., Zhao, Z., Whalen, C. B., Waterhouse, A. F., Trossman, D. S., Sun, O. M., Laurent, L. C. S., Simmons, H. L., Polzin, K., Pinkel, R., et al. (2017). Climate process team on internal wave–driven ocean mixing. *Bulletin of the American Meteorological Society*, *98*(11), 2429–2454. https://doi.org/10.1175/BAMS-D-16-0030.1

Macrander, A., Valdimarsson, H., & Jónsson, S. (2014). Improved transport estimate of the east icelandic current 2002–2012. *Journal of Geophysical Research: Oceans*, *119*(6), 3407–3424. https://doi.org/10.1002/2013JC009517

Mahadevan, A. (2016). The impact of submesoscale physics on primary productivity of plankton. *Annual review of marine science*, *8*, 161–184. https://doi.org/10.1146/annurev-marine-010814-015912

Mahadevan, A., D'asaro, E., Lee, C., & Perry, M. J. (2012). Eddy-driven stratification initiates north atlantic spring phytoplankton blooms. *Science*, *337*(6090), 54–58. https://doi.org/10.1126/science.1218740

Mandelbrot, B. B., & Mandelbrot, B. B. (1982). *The fractal geometry of nature* (Vol. 1). WH freeman New York.

Manucharyan, G. E., & Thompson, A. F. (2017). Submesoscale sea ice-ocean interactions in marginal ice zones. *Journal of Geophysical Research: Oceans*, *122*(12), 9455–9475. https://doi.org/10.1002/2017JC012895

Mathieu, L. (2019). Using a towed undulating platform to measure ocean velocities and to estimate turbulent dissipation rate (master thesis). *EPFL*. https://epic.awi.de/id/eprint/49871/1/Mathieu_MSc_2019.pdf

McHardy, I., & Czerny, B. (1987). Fractal x-ray time variability and spectral invariance of the seyfert galaxy ngc5506. *Nature*, *325*(6106), 696–698. https://doi.org/10.1038/325696a0

McWilliams, J. C. (2016). Submesoscale currents in the ocean. *Proceedings of the Royal Society A: Mathematical, Physical and Engineering Sciences*, *472*(2189), 20160117. https://doi.org/10.1098/rspa.2016.0117

McWilliams, J. C., Colas, F., & Molemaker, M. (2009). Cold filamentary intensification and oceanic surface convergence lines. *Geophysical research letters*, *36*(18). https://doi.org/10.1029/2009GL039402

Njoku, E. G. (2014). *Encyclopedia of remote sensing*. Springer New York.

Orsi, A. H., Whitworth III, T., & Nowlin Jr, W. D. (1995). On the meridional extent and fronts of the antarctic circumpolar current. *Deep Sea Research Part I: Oceanographic Research Papers*, *42*(5), 641–673. https://doi.org/10.1016/0967-0637(95)00021-W

Park, Y.-H., Park, T., Kim, T.-W., Lee, S.-H., Hong, C.-S., Lee, J.-H., Rio, M.-H., Pujol, M.-I., Ballarotta, M., Durand, I., et al. (2019). Observations of the antarctic circumpolar current over the udintsev fracture zone, the narrowest choke point in the southern ocean. *Journal of Geophysical Research: Oceans*, *124*(7), 4511–4528. https://doi.org/10.1029/2019JC015024

Pérez-Hernández, M. D., Pickart, R. S., Pavlov, V., Ingvaldsen, R., & Sundfjord, A. (2016). The atlantic water boundary current north of svalbard. *American Geophysical Union, Ocean Sciences Meeting*, *2016*, HE51A–07.

Ruddick, B. (1983). A practical indicator of the stability of the water column to double-diffusive activity. *Deep Sea Research Part A. Oceanographic Research Papers*, *30*(10), 1105–1107. https://doi.org/10.1016/0198-0149(83)90063-8

Rudels, B., Björk, G., Nilsson, J., Winsor, P., Lake, I., & Nohr, C. (2005). The interaction between waters from the arctic ocean and the nordic seas north of fram strait and along the east greenland current: Results from the arctic ocean-02 oden expedition. *Journal of Marine Systems*, *55*(1-2), 1–30. https://doi.org/10.1016/j.jmarsys.2004.06.008

Rudels, B., Fahrbach, E., Meincke, J., Budéus, G., & Eriksson, P. (2002). The east greenland current and its contribution to the denmark strait overflow. *ICES Journal of Marine Science*, *59*(6), 1133–1154. https://doi.org/10.1006/jmsc.2002.1284

Rudnick, D. L., & Ferrari, R. (1999). Compensation of horizontal temperature and salinity gradients in the ocean mixed layer. *Science*, *283*(5401), 526–529. https://doi.org/10.1126/science.283.5401.526

Rudnick, D. L., & Martin, J. P. (2002). On the horizontal density ratio in the upper ocean. *Dynamics of atmospheres and oceans*, *36*(1-3), 3–21. https://doi.org/10.1016/0079-6611(81)90011-2

Sarkar, S., & Scotti, A. (2017). From topographic internal gravity waves to turbulence. *Annual Review of Fluid Mechanics*, *49*, 195–220. https://doi.org/10.1146/annurev-fluid-010816-060013

Smith, K. S., & Ferrari, R. (2009). The production and dissipation of compensated thermohaline variance by mesoscale stirring. *Journal of Physical Oceanography*, *39*(10), 2477–2501. https://doi.org/10.1175/2009JPO4103.1

Smith, W. H., & Wessel, P. (1990). Gridding with continuous curvature splines in tension. *Geophysics*, *55*(3), 293–305. https://doi.org/10.1190/1.1442837

Spiro Jaeger, G., & Mahadevan, A. (2018). Submesoscale-selective compensation of fronts in a salinity-stratified ocean. *Science advances*, *4*(2), e1701504. https://doi.org/10.1126/sciadv.1701504

Stewart, K. D., & Haine, T. W. (2016). Thermobaricity in the transition zones between alpha and beta oceans. *Journal of Physical Oceanography*, *46*(6), 1805–1821. https://doi.org/10.1175/JPO-D-16-0017.1

Sun, L., Zhang, J., & Meng, J. (2021). Study on the propagation velocity of internal solitary waves in the andaman sea using terra/aqua-modis remote sensing images. *Journal of Oceanology and Limnology*, *39*(6), 2195–2208. https://doi.org/10.1007/s00343-020-0280-6

Swallow, J. C. (1971). A discussion on ocean currents and their dynamics-the aries current measurements in the western north atlantic. *Philosophical Transactions of the Royal Society of London. Series A, Mathematical and Physical Sciences*, *270*(1206), 451–460. https://doi.org/10.1098/rsta.1971.0084

Swart, S., du Plessis, M. D., Thompson, A. F., Biddle, L. C., Giddy, I., Linders, T., Mohrmann, M., & Nicholson, S.-A. (2020). Submesoscale fronts in the antarctic marginal ice zone and their response to wind forcing. *Geophysical Research Letters*, *47*(6), e2019GL086649. https://doi.org/10.1029/2019GL086649

Talley, L. D., Pickard, G. L., Emery, W. J., & Swift, J. H. (2011). Atlantic ocean. In *Descriptive physical oceanography* (Sixth, pp. 245–301). Academic Press. https://doi.org/10.1016/B978-0-7506-4552-2.10009-5

Teigen, S. H., Nilsen, F., & Gjevik, B. (2010). Barotropic instability in the west spitsbergen current. *Journal of Geophysical Research: Oceans*, *115*(C7). https://doi.org/10.1029/2009JC005996

Thomas, L. N., Tandon, A., & Mahadevan, A. (2008). Submesoscale processes and dynamics. *Ocean modeling in an Eddying Regime*, *177*, 17–38. https://doi.org/10.1029/177GM04

Timmermans, M.-L., Cole, S., & Toole, J. (2012). Horizontal density structure and restratification of the arctic ocean surface layer. *Journal of Physical Oceanography*, *42*(4), 659–668. https://doi.org/10.1175/JPO-D-11-0125.1

Timmermans, M.-L., & Winsor, P. (2013). Scales of horizontal density structure in the chukchi sea surface layer. *Continental Shelf Research*, *52*, 39–45. https://doi.org/10.1016/j.csr.2012.10.015

Tippins, D., & Tomczak, M. (2003). Meridional turner angles and density compensation in the upper ocean. *Ocean Dynamics*, *53*, 332–342. https://doi.org/10.1007/s10236-003-0056-5

Tomczak, M., & Godfrey, J. S. (2003). *Regional oceanography: An introduction*. Daya books.

Tomczak Jr, M. (1981). An analysis of mixing in the frontal zone of south and north atlantic central water off north-west africa. *Progress in Oceanography*, *10*(3), 173–192.

Treguier, A. M., de Boyer Montégut, C., Bozec, A., Chassignet, E. P., Fox-Kemper, B., McC. Hogg, A., Iovino, D., Kiss, A. E., Le Sommer, J., Li, Y., et al. (2023). The mixed-layer depth in the ocean model intercomparison project (omip): Impact of resolving mesoscale eddies. *Geoscientific Model Development*, *16*(13), 3849–3872. https://doi.org/10.5194/gmd-16-3849-2023

Våge, K., Pickart, R. S., Spall, M. A., Moore, G., Valdimarsson, H., Torres, D. J., Erofeeva, S. Y., & Nilsen, J. E. Ø. (2013). Revised circulation scheme north of the denmark strait. *Deep Sea Research Part I: Oceanographic Research Papers*, *79*, 20–39. https://doi.org/10.1016/j.dsr.2013.05.007

von Appen, W.-J., Hölemann, J. A., Mole, R., Oetjens, A., Hölemann, A., Becker, H., Bracher, A., Zeising, M., & Klaas, C. (2023). Raw data from Triaxus topAWI (towed ocean profiler of the AWI) during RV POLARSTERN cruise PS133/1. https://doi.org/10.1594/PANGAEA.962675

von Appen, W.-J., Kanzow, T., Hoppmann, M., McPherson, R., Hofmann, Z., Mathieu, L., Reifenberg, S. F., Becker, H., Monsees, M., Graupner, R., Allerholt, J., & Bracher, A. (2023). Raw data from Triaxus topAWI (towed ocean profiler of the AWI) during RV POLARSTERN cruise PS131. https://doi.org/10.1594/PANGAEA.962659

von Appen, W.-J., Strass, V. H., Becker, H., Bracher, A., & Spahic, S. (2019). Raw data from Triaxus topAWI tows during POLARSTERN cruise PS113. https://doi.org/10.1594/PANGAEA.904420

von Appen, W.-J., Strass, V. H., Bracher, A., Xi, H., Hörstmann, C., Iversen, M. H., & Waite, A. M. (2020). High-resolution physical–biogeochemical structure of a filament and an eddy of upwelled water off northwest africa. *Ocean Science*, *16*(1), 253–270. https://doi.org/10.5194/os-16-253-2020

von Appen, W.-J., Waite, A. M., Bergmann, M., Bienhold, C., Boebel, O., Bracher, A., Cisewski, B., Hagemann, J., Hoppema, M., Iversen, M. H., et al. (2021). Sea-ice derived meltwater stratification slows the biological carbon pump: Results from continuous observations. *Nature Communications*, *12*(1), 7309. https://doi.org/10.1038/s41467-021-26943-z

von Appen, W.-J., Wekerle, C., Hehemann, L., Schourup-Kristensen, V., Konrad, C., & Iversen, M. H. (2018). Observations of a submesoscale cyclonic filament in the marginal ice zone. *Geophysical Research Letters*, *45*(12), 6141–6149. https://doi.org/10.1029/2018GL077897

Wijesekera, H. W. (1996). Fractal dimension as an indicator for turbulent mixing in the thermocline. *Journal of Geophysical Research: Oceans*, *101*(C7), 16703–16709. https://doi.org/10.1029/96JC01349

You, Y. (2002). A global ocean climatological atlas of the turner angle: Implications for double-diffusion and water-mass structure. *Deep Sea Research Part I: Oceanographic Research Papers*, *49*(11), 2075–2093. https://doi.org/10.1016/S0967-0637(02)00099-7

Yuan, X., Patoux, J., & Li, C. (2009). Satellite-based midlatitude cyclone statistics over the southern ocean: 2. tracks and surface fluxes. *Journal of Geophysical Research: Atmospheres*, *114*(D4). https://doi.org/10.1029/2008JD010873